natural sciences .be
Geological Survey of Belgium
LIÈGE université

ESTIMATING SURFACE DISPLACEMENTS USING SAR DATA AND HYDRO-GEOMECHANICAL MODELS AND IGRS PERFORMANCE ASSESSMENT

Doctoral Thesis by

Atefe Choopani

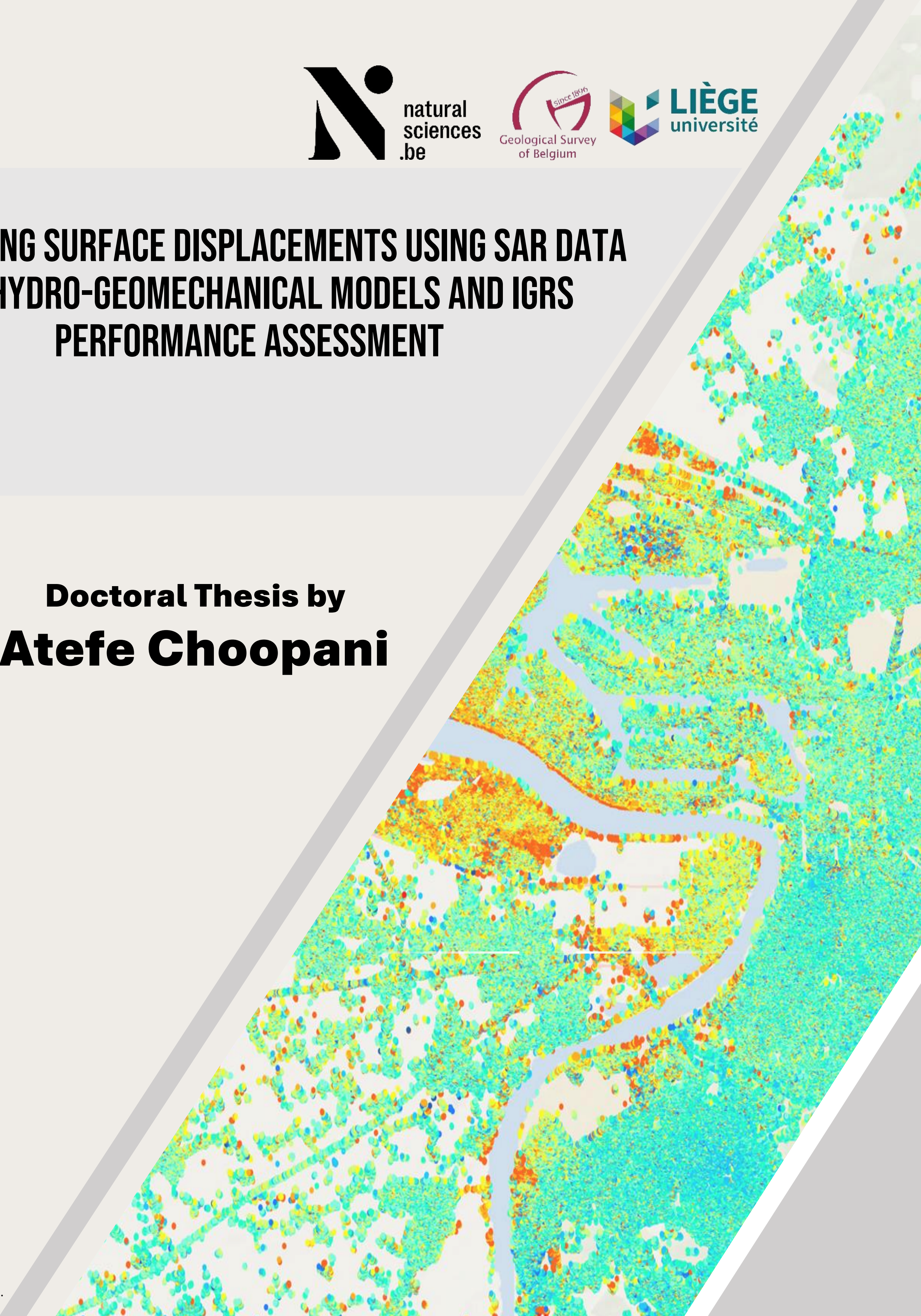

Cover page data provided by SkyGeo.

Atefe Choopani

Bachelor in Geomatics Engineering

Tafresh University, Iran, 2015

Master in Remote Sensing

Shiraz University, Iran, 2017

atefe.choopani@yahoo.com

atefe.choopani@doct.uliege.be

atefe.choopani@naturalsciences.be

atefe-choopani

0000-0002-2184-4187

Submitted on October 31, 2024, in partial fulfillment of the requirements for the degree of Doctor of Philosophy (Ph.D.) in Engineering Science and Technology awarded by the University of Liège

University of Liège (ULiege)
Faculty of Applied Sciences
Urban and Environmental Engineering (UEE)
Geology and Applied Geology
Hydrogeology and Environmental Geology

Royal Belgian Institute of Natural Sciences (RBINS)
Geological Survey of Belgium (GSB)
Geohazards Research Group

Estimating Surface Displacements Using SAR Data and Hydro-Geomechanical Models and IGRS Performance Assessment

Doctoral Thesis Presented by

Atefe Choopani

Jury Members

Alain Dassargues	Hydrogeology and Environmental Geology, Faculty of Applied Sciences, Liège University
Xavier Devleeschouwer	Royal Belgian Institute of Natural Sciences, Geological Survey of Belgium
Philippe Orban	Hydrogeology and Environmental Geology, Liège University
Pierre-Yves Declercq	Royal Belgian Institute of Natural Sciences, Geological Survey of Belgium
Ramon F. Hanssen	Faculty of Civil Engineering and Geosciences, Delft University of Technology
Michel Van Camp	General Director, Royal Belgian Institute of Natural Sciences
Bertrand François	Geotechnical Engineering, Faculty of Applied Sciences, University of Liège

September 2024

This research was generously funded by BELSPO through the BRAIN (Belgian Research Action through Interdisciplinary Networks) program.

The project, entitled "Monitoring LAnd SUbsidence caused by Groundwater Exploitation through gEOodetic Measurements" (LASUGEO), was conducted under the BRAIN BELSPO program from 2019 to 2023.

Dedication

To the women of Iran
and their ongoing fight
for life and freedom.

Acknowledgments

First of all, I would like to express my deepest gratitude to my supervisor from the University of Liege, Prof. Alain Dassargues. He is a very strict professor, and I must honestly say that I did not receive positive feedback from him many times. However, I valued the few that I did receive, as satisfying him scientifically was not an easy task. His high standards pushed me to refine my work and increase my scientific rigor. Most importantly, he taught me the importance of being meticulous with every sentence in the scientific world. At the end of this journey, I came to appreciate how nice he was to me, and I am deeply grateful for his mentorship. Merci beaucoup, Alain, pour tout votre soutien et vos conseils.

I am also very grateful to my other supervisor at the Geological Survey of Belgium, Dr. Xavier Devleeschouwer. His support was invaluable throughout this journey. Whenever I encountered difficulties in understanding geology, which was not my background, he explained everything with great humility and patience. His encouragement and unwavering support helped me overcome many challenges. Merci, Xavier, pour vos conseils inestimables et votre soutien infini.

I would also like to extend my heartfelt thanks to Dr. Philippe Orban. Although he was not officially my supervisor, he played a crucial role in my journey. He helped me immensely, particularly with the practical aspects of my work in modeling. His willingness to assist me at every step made a significant difference, and for that, I am sincerely thankful. Merci, Philippe, pour votre soutien constant et votre aide précieuse.

I extend my heartfelt thanks to Professor Ramon Hanssen and Dr. Freek van Leijen from Delft University, Prof. Maryam Dehghani from Shiraz University, and Prof. Bertrand François from the University of Liege. Despite not being their student, their occasional remarks and insights were invaluable to my work. Their expertise and willingness to offer guidance have been greatly appreciated.

I would like to express my gratitude to Dr. Pierre-Yves Declercq from the Geological Survey of Belgium for his help throughout this project. I am also sincerely thankful to Mrs. Chandra Algoe, Leen De Vos, Mr. Johan Lermytte, Mr Tom van Haren for providing essential data and their valuable consultation, which was crucial for the success of this research.

A special and heartfelt thank you goes to my friend, Mr. Chrishan Foneska. His support, both as a friend and a colleague, went above and beyond what I could have hoped for. His guidance, encouragement, and tireless efforts significantly contributed to the completion of this work. I would also like to extend my thanks to Mr. Amin Tavakkoli Estahbanati, Milad Yarmohammad Touski, and Mohammad Kaveh for their valuable consultation and support throughout this journey.

I am deeply thankful to my mother, brother, and sisters. Though distance separates us, your love and support have always been with me, giving me the strength to keep fighting. Thank you for being my source of resilience.

Lastly, I am so grateful to my beloved husband, my constant and faithful companion, who has been my greatest source of strength throughout this journey. Your belief in me, even when I struggled to believe in myself, has made all the difference. You have shouldered my worries and celebrated my achievements as if they were your own, never wavering in your dedication to our shared dreams. Your love and steadfast presence have made this journey not only bearable but meaningful. I cannot thank you enough for being my greatest champion.

Table of Contents

Abstract 1
1. Introduction 3
1.1. Background 4
1.2. Objectives & Motivations 7
1.3. Method & Materials 9
1.4. Thesis Outline 11
2. Background Theory 12
2.1. Principles of PS-InSAR 13
2.2. Hydrogeological Modeling 22
2.3. Geomechanical Modeling 24
3. Subsidence in Antwerp Harbour: PS-InSAR and Coupled Hydrogeological-Geomechanical Modeling 27
3.1. Abstract 28
3.2. Introduction 29
3.2.1. InSAR Technology 29
3.2.2. Subsidence Due to Groundwater Pumping or Drainage 30
3.2.3. Land Subsidence in Antwerp 31
3.3. Land Subsidence Modeling 35
3.4. Challenges in Measurements & Data 39
3.4.1 Data Overview 39
3.4.1.1. Land Subsidence Measurements 39
3.4.1.2. Hydrogeological Data 44
3.4.1.3. Geomechanical Data 46
3.4.2. Impact of Data Scarcity on Modeling 48
3.5. Simulated Delayed Deformation 50
3.6. Results 52
3.6.1. Water Head Evolution in Different Sublayers 52
3.6.2. Pore Pressure Distribution Across Model Layers 54
3.6.3. Computed Deformation Across Model Layers 54
3.6.4. Comparison Between 1D Geomechanical Model Results with PS-InSAR Estimations 56
3.6.5. Sensitivity Analysis of 1D Geomechanical Model 59
3.7. Conclusions 62
4. Land Surface Deformation in Saint-Vaast 65
4.1. Abstract 66
4.2. Introduction 67
4.3. Region of Interest 70
4.3.1. Geographical and Geological Setting 70
4.3.2. Saint-Vaast Incidents of 2009 and 2018 73
4.4. Methods & Materials 76
4.4.1. PS-InSAR Technique, Processing, and SAR Datasets 76
4.4.2. Water Level Monitoring 78
4.5. Results 79
4.5.1. PS-InSAR Displacements 79
4.5.2. PS-InSAR Timeseries Analysis 83
4.5.3. Analysis of Piezometric Wells 86
4.6. Discussion & Conclusions 90
5. Performance Assessment of the IGRS Corner Reflectors 92
5.1. Introduction 93
5.2. Theoretical Background 95
5.3. IGRS Installation in Doel 99
5.4. Results 102
5.5. Discussions 109
6. Conclusions and Perspectives 111
6.1. Conclusions 112
6.2. Perspectives 115
References 117
Appendix A. Scientific Contribution and Publications 134

Abstract

Interferometric Synthetic Aperture Radar (InSAR) has been a crucial technique for monitoring land subsidence and uplift due to its ability to provide high-resolution, continuous spatial and temporal data. This thesis aims to enhance the understanding of ground deformation mechanisms in regions with complex geological settings by integrating InSAR estimations with hydrogeological and geomechanical models. Two case studies are investigated: Antwerp Harbour, a major industrial area experiencing significant land subsidence, and the Saint-Vaast region, a former coal mining area facing land subsidence and uplift challenges.

In Antwerp Harbour, subsidence is driven by natural and anthropogenic factors. The natural consolidation of Holocene sediments, the additional consolidation due to the backfill overload along harbour docks, the saturated-unsaturated consolidation of backfill materials, and the consolidation of compressible layers induced by groundwater pumping in Cenozoic aquifers are identified as the possible key drivers. Persistent Scatterer InSAR (PS-InSAR) was employed to monitor displacements, providing high-resolution surface deformation data. Coupled hydrogeological and geomechanical modeling was conducted in a local scale model out of the border of backfill to isolate only the effects of groundwater extraction on land subsidence. This approach enabled the exclusion of other factors and focused specifically on the impact of groundwater pumping. By integrating these methods, the study quantified the contribution of groundwater extraction relative to other factors, enhancing the understanding of complex interactions between surface deformations and subsurface processes.

The Saint-Vaast region presents unique geohazards due to presence of an old drainage adit in the historical coal mining region. During the post-mining period, this drainage adit was filled with water, changing subsurface pressure regimes and causing both land subsidence and uplift. This study used three decades of PS-InSAR data to detect and map temporal and spatial dynamics of ground displacements. All relevant spatial data, including an old drainage adit from the coal mining exploitation period, geological layers, and hydrogeological conditions, were mapped to understand the structural context of observed deformations. Thirteen years of piezometric well data provided insights into subsurface hydrodynamics. Breakpoints in the PS-InSAR time series, significant shifts in deformation rates, were identified showing the temporal evolution of ground deformation and its correlation with hydrogeological events. Correlation analysis linked ground deformation with mudflow events in 2009 and 2018, demonstrating a strong relationship between changes in groundwater levels and surface deformation patterns.

This thesis provides a comprehensive methodology for studying surface deformation phenomena by integrating the PS-InSAR technique with hydrogeological and geomechanical analyses and models. The insights gained contribute to a better understanding of the complex interactions between surface and subsurface processes, supporting the development of effective strategies for mitigating deformation-related geohazards. These geohazards are associated respectively with industrial areas under extensive developments and with densely populated urbanized areas. The main idea of the thesis is also to conduct a comparison between SAR data obtained by different satellites vs the estimated ground displacement measurements deduced from the SAR LOS timeseries and other techniques like hydrogeological and geomechanical models.

Additionally, this research assesses the performance of Integrated Geodetic Reference Stations (IGRS) installed in Antwerp, close to the Doel nuclear plant. The performance assessment focused on analyzing the IGRS data for stability and reliability, demonstrating generally high consistency and accuracy in range and azimuth measurements using SAR data. The results, including time series and Signal-to-Clutter Ratio (SCR) analysis, validated the quality of radar measurements. However, for a definitive assessment of their ability to measure and monitor surface displacements accurately, further validation with GPS antenna installed on the station would be necessary. Future studies should aim to seek this purpose. This would involve decomposing the line-of-sight (LOS) deformation into vertical and horizontal components and comparing these with GPS measurements to confirm their accuracy in monitoring surface displacements.

1

Introduction

1.1. Background

InSAR, or Interferometric Synthetic Aperture Radar, is a remote sensing technique that has become increasingly important in monitoring and understanding natural hazards such as land subsidence and uplift (Aswathi, et al. 2022; Bokhari et al. 2023). InSAR's capacity to provide high-resolution, continuous spatial and temporal data makes it an essential tool for detecting and mitigating the impacts of geological and hydrogeological processes (Krieger et al. 2009; Cigna et al. 2011). Land subsidence, the gradual settling or sudden sinking of the Earth's surface, is a potentially destructive hazard caused by various natural and anthropogenic activities, posing a serious threat to infrastructure, water resources, and human safety (Siriwardane-de Zoysa et al. 2021; Zhang et al. 2024). Land subsidence can result from a range of factors, including natural processes like sediment compaction, tectonic activity, and anthropogenic activities such as groundwater extraction, mining, and the construction of heavy infrastructure (Abidin et al. 2012; Maaß and Schüttrumpf 2018; Ikuemonisan and Ozebo 2020). In coastal and urban areas, subsidence increases flood risks and can result in significant economic losses (Huang and Jin 2018; Voyiadjis et al. 2024).

To fully use the capabilities of InSAR, advanced techniques such as Persistent Scatterer InSAR (PS-InSAR) (Ferretti et al. 1999) and Multi-Temporal InSAR (MT-InSAR) (Hooper 2008) have been developed (Aswathi et al. 2022). PS-InSAR enhances conventional InSAR by focusing on stable, point-like reflectors known as persistent scatterers, which consistently reflect radar signals over time. This technique significantly improves the accuracy of ground deformation measurements by filtering out noise and atmospheric disturbances, allowing for millimeter-level precision in detecting surface movements (Crosetto et al. 2016).

PS-InSAR’s ability to cover large areas with high spatial resolution allows for the mapping of ground deformation patterns over wide regions (Qu et al. 2015). PS-InSAR is particularly advantageous in urban environments, where numerous man-made structures serve as reliable persistent scatterers. This capability is especially beneficial in industrial areas such as Antwerp Harbour, where traditional ground-based measurements are often sparse or entirely absent.

Despite the advancements offered by InSAR and hydrogeology, relying solely on either technique for studying land subsidence and uplift can result in significant limitations and incomplete interpretation. While InSAR provides precise measurements of surface deformation, it does not provide the ability to directly identify subsurface processes or determine the causes of the observed movements. On the other hand, hydrogeological studies offer crucial insights into subsurface fluid dynamics and geological conditions but often lack the spatial and temporal resolution to capture detailed surface deformation patterns. Without the integration of both, studies may either overlook critical subsurface interactions or fail to accurately link surface observations to their underlying causes. This can lead to incomplete hazard assessments and less effective mitigation strategies. By combining InSAR with hydrogeological and geomechanical data, a more comprehensive understanding of deformation mechanisms is achieved.

Despite the clear benefits of integrating InSAR with hydrogeological and geomechanical analyses, several challenges persist. One major challenge is the difference in spatial and temporal scales at which these data sets are acquired. InSAR typically provides high-resolution, wide-area coverage over time, while hydrogeological data can be more localized and sporadic. Aligning these disparate data sets to ensure coherent and meaningful interpretations remains challenging. Additionally, the inherent uncertainties in both InSAR measurements and hydrogeological models need to be carefully interpreted and managed. Another significant challenge is the interdisciplinary expertise required; effective integration demands not only technical proficiency in remote sensing and geomechanics but also a deep understanding of hydrogeological processes. Overcoming these challenges is essential for developing more accurate models and reliable interpretations of land subsidence and uplift, ultimately leading to better-informed decision-making and risk management.

Despite the challenges, integrating InSAR with hydrogeological data and modeling provides a comprehensive methodology for studying surface deformation phenomena. This multidisciplinary approach is essential for explaining the complexities of subsurface dynamics and their surface phenomenon. Hydrogeological data, encompassing groundwater flow and distribution patterns, offer essential insights into subsurface fluid dynamics, while geomechanical models explain the stress-strain relationships within the subsurface. The combination of these approaches captures both surface and subsurface processes.

The motivation for this study is to increase our understanding of ground deformation mechanisms, especially in regions with complex geological settings. This research aims to address the challenges of accurately characterizing and understanding subsurface deformation in those areas that are characterized by significant subsurface heterogeneity, which complicates the interpretation of surface deformation signals.

One exemplary application of InSAR is in monitoring subsidence in Antwerp harbour, one of Europe's largest and busiest ports. Antwerp harbour has been experiencing significant subsidence due to both natural and anthropogenic factors. Naturally, the gradual consolidation of Holocene sediments causes slow compression and ground sinking over time. However, human activities have accelerated this process. The heavy infrastructure associated with port facilities, such as docks, warehouses, and transportation networks, adds substantial weight to the land, causing further compression. Additionally, continuous dredging of the Scheldt River and port expansion activities have disrupted the natural sediment balance, increasing subsidence. The presence of heavy industries, such as petrochemicals and shipping, contributes further by increasing the load on the ground. Historical urban development has also played a role in the long-term subsidence issues. These combined factors, particularly noticeable from the late 20th century onwards, highlight the necessity for continuous monitoring and management to mitigate flood risks and maintain the economic viability of Antwerp's port.

In contrast, the Saint-Vaast region, a former coal mining area, faces unique challenges related to the reactivation of old mining voids and changes in subsurface hydrology. This area has a long history of coal mining that dates back to the late 19th century, resulting in an extensive network of underground tunnels and voids. Over time, the cessation of mining activities led to the abandonment of these voids, which began to fill with water due to the natural groundwater recharge process. This re-flooding changed the subsurface pressure regimes significantly, causing both subsidence and uplift in different periods. The reactivation of these old voids, as they filled with water, introduced a complex set of hydrogeological dynamics, where the increased pore pressure in the aquifer above the mined-out spaces led to the deformation of the overlying strata. The presence of loose sediments of thin layers of clay and sand further complicated the situation, as these materials responded differently to the changes in pressure and saturation. This combination of factors resulted in ground movements in different periods. The region has experienced at least two mudflow outbursts from an old gallery so far. These events, in 2009 and 2018, have led to land subsidence. Monitoring and mitigating these risks require a detailed understanding of the interplay between historical mining activities, current groundwater dynamics, and the geological characteristics of the area.

1.2. Objectives & Motivations

In this study, we aim to address key questions about the mechanisms of ground deformation in regions with complex geological settings, using two distinct but related case studies: Antwerp Harbour and the Saint-Vaast region.

The Antwerp Harbour case study explores ground deformation by integrating InSAR data with hydrogeological and geomechanical modeling. In contrast, the Saint-Vaast region involves comparing InSAR deformation time series with piezometric time series.

The first essential question this thesis seeks to answer focuses on the subsidence driver in the Antwerp local model: **What are the effects of groundwater extraction in the subsidence estimated in the local model area, and how can the results from the local model help us generalize the role of groundwater extraction in driving deformation across the entire Antwerp region?**

In previous studies, it was concluded that the deformation observed by InSAR was significant primarily in areas where backfill is present, particularly in the harbour (Declercq et al. 2021). Based on this observation, it was assumed that the subsidence in Antwerp was driven solely by the compaction of the backfill material. However, this conclusion overlooked other important potential subsurface processes that may contribute to the observed ground deformation. Limiting the interpretation of subsidence to only backfill compaction oversimplifies the complexity of the region's geological and hydrogeological dynamics, especially considering that some subsidence is estimated in areas where no backfill is present. Therefore, a more comprehensive analysis is required to fully understand the subsidence mechanisms at play. To address this, we have specified four possible drivers of subsidence in the entire Antwerp region: the natural consolidation of the Holocene estuarine sediments, the additional consolidation in the saturated Holocene estuarine sediments due to the backfill overload (8-meter-thick embankments) along the harbour docks, the saturated-unsaturated consolidation of the backfill materials, and the consolidation of the most compressible layers, due to pore pressure decrease induced by groundwater pumping in the different Cenozoic aquifers.

To isolate the effects of deformation due to possible groundwater extraction, we conducted coupled hydrogeological and geomechanical modeling outside the borders of the embankment. This approach allowed us to exclude the effects of the other three drivers and focus specifically on the impact of groundwater pumping on the subsidence observed by PS-InSAR. The contribution of groundwater extraction relative to the other factors is quantified. This increases our understanding of the complex interactions between surface deformations and subsurface processes. We aim to isolate deformation caused by groundwater extraction and identify which shallow or deep layers are responsible for this deformation. Specifically, we seek to determine whether the deformation originates from an aquifer or an aquitard. At the end, the mechanisms of deformation in the local model can be generalized to the entire Antwerp region. While it is true that we are not conducting modeling for the entire Antwerp area, the hydrogeological conditions in the local model are similar to those beneath the Antwerp harbour, with the key difference being the presence of backfill material in the harbour, which is absent in the local model. If groundwater extraction plays a role in subsidence within the local model, it is reasonable to suggest that it could also be contributing to subsidence in the Antwerp harbour. However, the extent to which groundwater extraction contributes to subsidence in the harbour remains uncertain, as we do not know how much of the deformation in the Antwerp harbour is specifically due to this factor. Further investigation would be required to quantify its share in the overall subsidence observed in the harbour area.

The second essential question this thesis seeks to answer focuses on the Saint-Vaast region: **What are the hydrogeological processes driving subsidence and uplift in the post-mining area of Saint-Vaast, and how are these related to the clogging of water in the old mining galleries?** Using three decades of PS-InSAR estimations we detected and mapped temporal and spatial dynamics of ground deformation in Saint-Vaast, capturing distinct periods of both subsidence and uplift.

We also mapped all relevant spatial data, including an old drainage gallery from the mining time, the geological layers, and hydrogeological conditions of the region, and locations of mudflow outbursts.

To gain insights into subsurface hydrodynamics, we used 13 years of data from piezometric wells in the region. These wells monitored groundwater levels and provided critical information on subsurface water dynamics. We defined breakpoints in the PS-InSAR time series, which are significant shifts in deformation rates indicative of underlying geomechanical processes. Identifying these breakpoints was crucial for understanding the temporal evolution of ground deformation and its correlation with hydrogeological events.

Finally, we conducted a correlation analysis to link the observed ground deformation with the two significant mudflow events in 2009 and 2018. This demonstrated a strong relationship between changes in groundwater levels, as recorded by the piezometric wells, and the surface deformation patterns estimated through PS-InSAR.

In addition to the core questions of the study, an extra research objective is introduced in this thesis related to the implementation and evaluation of Interferometric Geodetic Reference Stations (IGRS) in Doel. The question posed is: **How does the corner reflector of the Doel Integrated Geodetic Reference Station (IGRS) perform in terms of precise positioning using SAR data?** This investigates the effectiveness of IGRS in improving the precision of InSAR measurements by analyzing its contributions in this specific case study, focusing on signal-to-clutter ratio and radar cross-section optimizations.

1.3. Method & Materials

Figure 1.1 shows the comprehensive workflow used in our study in Antwerp. It starts with the acquisition and processing of radar data for PS-InSAR analysis, which provides high-resolution surface deformation data. This is followed by hydrogeological modeling using MODFLOW to simulate groundwater flow, incorporating sub-layering to capture delayed pore pressure propagation. Next, geomechanical modeling calculates vertical deformation by integrating storage parameters and stress-strain relationships. Finally, the modeled deformations are compared with PS-InSAR results. This integrated approach allows us to isolate and quantify the contribution of groundwater extraction to subsidence relative to other factors.

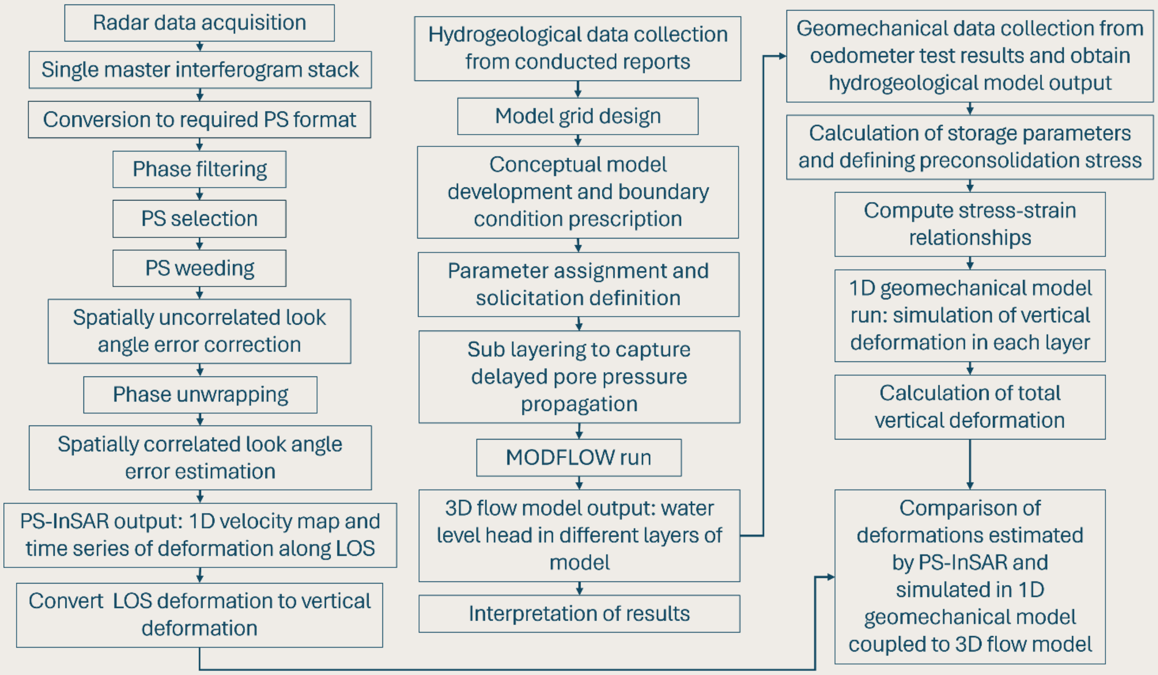

Figure 1.1. Workflow of the study integrating PS-InSAR analysis with hydrogeological model coupled to geomechanical model in Antwerp.

Figure 1.2 illustrates the workflow of the methodology applied in the Saint-Vaast case study. The PS-InSAR processing workflow follows the same steps as in the Antwerp case, as shown in Figure 1.1. After the deformation patterns were obtained from PS-InSAR, a correlation analysis was performed between the time series of the piezometric well data and the LOS time series extracted from the PS-InSAR results. This analysis aimed to investigate the evolution of the uplift and subsidence related to clogging of the old water adit present in the region.

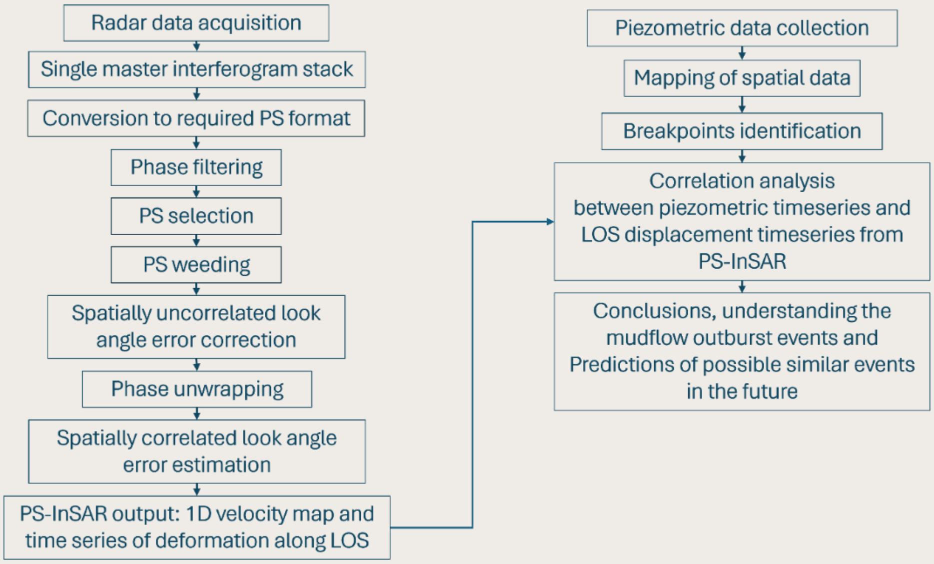

Figure 1.2. Workflow of the study integrating PS-InSAR analysis with piezometric data in Saint-Vaast.

In this study, we used InSAR data from multiple satellite missions to monitor displacements in Antwerp Harbour and the Saint-Vaast region. A detailed table summarizing the InSAR images used, including relevant parameters is provided (Table 1.1). In addition, two columns specifying the Local Incidence Angle (°) in the middle of each region and the corresponding Scaling Factor (Vertical), which converts Line of Sight (LoS) measurements to vertical displacements, have been included in the table.

Table 1.1 InSAR data characteristics for Antwerp Harbour and Saint-Vaast region

Region	Satellite	Wavelength (cm)	Track /Path	Geometry	Local Incidence Angle (°) in the middle of each region	Scaling Factor (on to vertical direction)	Pixel Size Slant range (m) × Azimuth (m)	Revisit Time
Antwerp	TerraSAR-X	X-Band	48	Descending	21.53	1.075	1.2 ×3.3	11 days
			116	Ascending	24.04	1.095		
	ERS-1/2	C-Band	423	Descending	29.62	1.150	10.2 ×6	35 days
	Envisat	C-Band	423	Descending	23.80	1.093	7.8 ×3.5	35 days
	Sentinel-1A	C-Band	88	Ascending	24.23	1.097	2.3 ×14.1	12 days
Saint-Vaast	ERS-1/2	C-Band	423	Descending	25.53	1.108	10.2 ×6	35 days
	Envisat	C-Band	423	Descending	28.89	1.142	7.8 ×3.5	35 days
	Sentinel-1A	C-Band	161	Ascending	39.97	1.305	2.3 ×14.1	12 days

1.4. Thesis Outline

The structure of this thesis is organized to address the research questions and objectives outlined. **Chapter 2** provides a summary of the foundational background theory necessary to understand the methodologies employed in this study. This covers the principles of PS-InSAR and the integrated approach of hydrogeological models coupled with geomechanical models. This theoretical framework sets the stage for the detailed case studies that follow.

Chapter 3 presents the first case study, focusing on the Antwerp Harbour region. This chapter delves into the specific question of identifying and monitoring the key drivers of subsidence in Antwerp. This chapter is under the form of a submitted paper to the *Hydrogeology Journal*.

Chapter 4 shifts to the Saint-Vaast region, addressing the second essential question. This chapter explains the hydrogeological and geomechanical processes driving subsidence and uplift in this post-mining area. This chapter is under the form of a submitted paper to *Natural Hazards Journal*.

Chapter 5 focuses on the implementation and evaluation of Interferometric Geodetic Reference Stations (IGRS) as a novel approach and a key step for enhancing the accuracy of ground deformation measurements. This chapter examines how IGRS can improve the precision of InSAR results by optimizing signal-to-clutter ratio (SCR) and radar cross-section (RCS).

Chapter 6 concludes the thesis by summarizing the key findings from both case studies, highlighting the challenges encountered, and discussing the broader implications of these findings. This chapter offers perspectives on future research directions and practical applications for managing deformation-related risks in similar regions.

References compile all the references cited throughout the thesis.

Appendices present scientific contributions and publications resulting from conference presentations, in the frame of this thesis, provided as an appendix.

2

Background Theory

2.1. Principles of PS-InSAR

This chapter provides a fundamental review of the underlying principles of PS-InSAR, hydrogeological modeling, and geomechanical modeling essential for this study. While many of these processes are performed using specialized software, understanding the theoretical basis is crucial for comprehending the exact procedures and methodologies employed. Specifically, the geomechanical modeling in this research is conducted using Python code developed as part of this study.

Interferometric Synthetic Aperture Radar (InSAR) relies on the principles of radar interferometry, where the phase of the radar signal is used to infer changes in the distance between the satellite and the ground surface (Rosen et al. 2000; Dzurisin and Lu 2007; Hrysiewicz et al. 2023). The phase information is sensitive to changes in the order of the radar wavelength, typically a few centimeters This sensitivity allows InSAR to detect very small surface deformations over large areas with high spatial resolution (Klees and Massonnet 1999). By interference of the two images, very small slant-range changes of the same surface can be inferred (Mastro et al. 2020). The slant-range is the direct line-of-sight distance between the radar on the satellite and the target on the ground.

Traditional radar systems, known as Real Aperture Radar (RAR), have resolutions limited by the physical size of the antenna (Blackledge 2005). A larger antenna can provide better resolution, but this is often impractical for airborne or spaceborne systems. Synthetic Aperture Radar (SAR) overcomes this limitation by synthesizing a large antenna electronically (Yang 2022) enabling higher-resolution images (Khoshnevis and Ghorshi 2020). Figure 2.1 illustrates the basic operation of a SAR system highlighting the transmission and reception of microwave signals, and the formation of the synthetic aperture. The figure shows how the radar antenna, moving along the satellite's orbit, synthesizes a large aperture by collecting reflected signals over a series of positions.

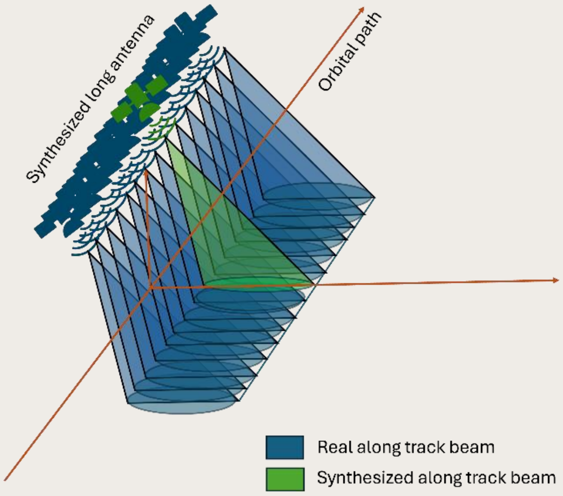

Figure 2.1 Schematic representation of Synthetic Aperture Radar (SAR) operation systems

SAR sensors transmit microwave pulses toward the Earth's surface and record the backscattered signals (Tomiyasu 1978; Moreira et al. 2013). By analyzing the phase differences between the reference and secondary images acquired at different times, InSAR can detect sub-centimeter deformation with millimeter-precision (Eneva et al. 2011). These phase differences can result from various factors, including tectonic movements, subsidence, or volcanic activity (Bürgmann et al. 2000; Bokhari et al. 2023). The significant advantage of InSAR is its ability to provide accurate deformation measurements over large areas with high spatial resolution.

InSAR data can be collected from ascending or descending satellite passes (Figure 2. 2). An ascending pass occurs when the satellite moves from south to north, whereas a descending pass occurs when it moves from north to south (Bouraoui 2013). These different geometries provide complementary perspectives, which can be crucial for comprehensive deformation analysis.

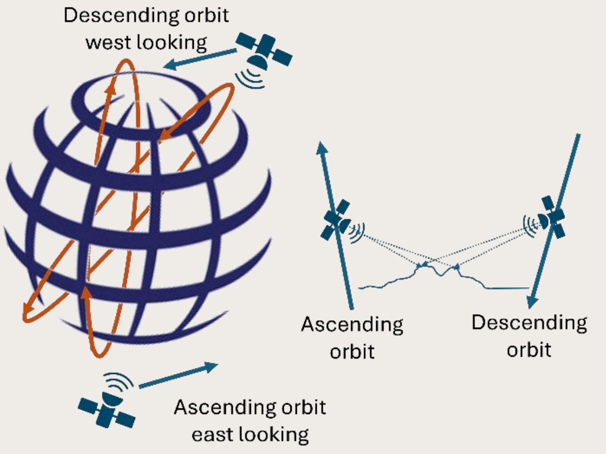

Figure 2.2 Schematic representation of ascending and descending geometry in SAR imaging

InSAR techniques measure only one-dimensional (1D) displacement in the satellite's Line of Sight (LOS) direction, which combines three-dimensional (3D) displacement components (east d_E, north d_N, and up d_U) and indicates the displacement of the ground surface towards or away from the satellite (Hanssen 2001; Azadnejad et al. 2024). As illustrated in Figure 2. 3, a SAR satellite system can only detect the component of ground displacement that lies along the LOS. Consequently, the measured displacement represents only a portion of the true displacement magnitude. Thus, decomposing the deformation measured by InSAR into vertical and horizontal components is essential for a complete understanding of surface movements.

This LOS displacement can be written as Equation (1):

$$d_{LOS} = (-\sin\theta\cos\alpha \quad \sin\theta\sin\alpha \quad \cos\theta)\begin{pmatrix} d_E \\ d_N \\ d_U \end{pmatrix} \tag{1}$$

where θ is the local incidence angle, and α is the azimuth of the zero-Doppler plane (ZDP) at the position of the target (Chang et al. 2018; Brouwer and Hanssen 2023). Estimating all three displacement components typically requires at least three independent Line of Sight (LOS) observations that are spatially and temporally coincident (Azadnejad et al. 2024).

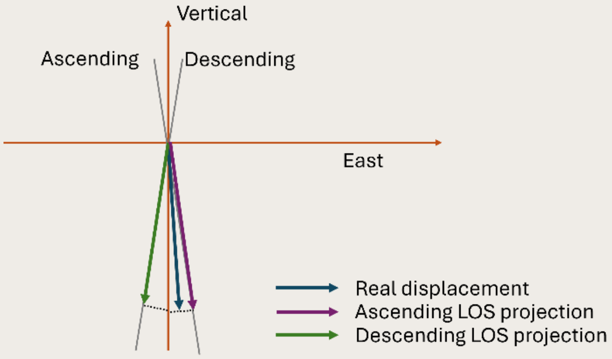

Figure 2.3 The displacements as detected by the line of sight directions.

The general equations for LOS displacement in ascending and descending passes can be written as:

$$d_{LOS-A} = -d_E\sin\theta_A\cos\alpha + d_N\sin\theta_A\sin\alpha + d_U\cos\theta_A \tag{2}$$

$$d_{LOS-D} = d_E\sin\theta_D\cos\alpha + d_N\sin\theta_D\sin\alpha + d_U\cos\theta_D \tag{3}$$

where d_{LOS-A} and d_{LOS-D} are the LOS displacements measured during the ascending and descending passes, and θ_A and θ_D are the incidence angles for the ascending and descending passes, respectively. In summary, the negative sign in the ascending pass equation reflects the coordinate system and viewing geometry of the satellite, where eastward movement is considered negative relative to the ascending satellite's perspective (Figure 2.4).

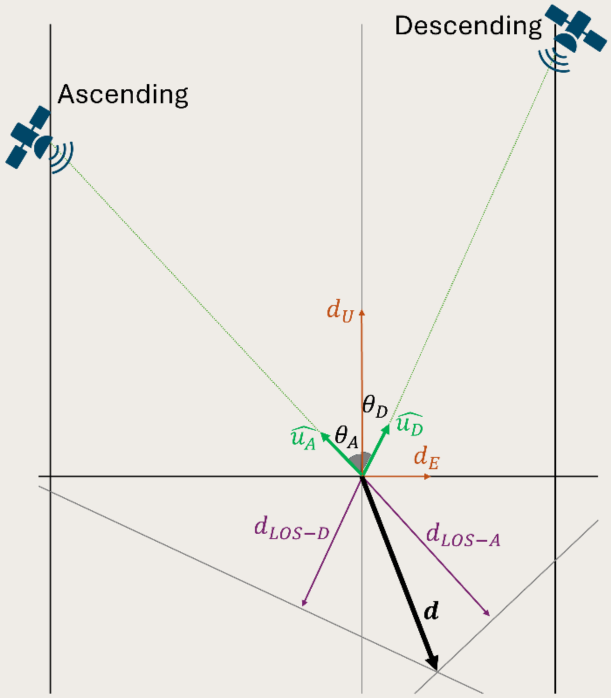

Figure 2.4 Coordinate system and viewing geometry of the satellite during ascending and descending passes. The unit vectors $\widehat{u_A}$ and $\widehat{u_D}$ represent the LOS directions for the ascending and descending passes, respectively.

However, it is important to emphasize the importance of carefully considering the assumptions made about displacement components in InSAR analysis, highlighted in Brouwer and Hanssen (2023). In some previous approaches, it has been assumed that displacements in the north-south direction (d_N) can be considered negligible. As Brouwer and Hanssen (2023) point out, one of the most frequently occurring geometric InSAR errors is the decomposition error. Specifically, the error arises when it is assumed that by combining ascending descending (the maximum number of spatio-temporally coinciding and independent) LOS observations, it is possible to accurately separate east-west horizontal displacement from vertical displacement. This assumption inevitably leads to biased estimates because the estimators for $d_E, d_N, and\ d_U$ are correlated and simply ignoring d_N from the inverse problem will lead to biased estimates for the other two.

In many practical situations, where only two LoS sets are available—typically from ascending and descending satellite passes—an important concept to consider is the null line. The null line arises because, with only two LOS observations, the problem becomes underdetermined, meaning there are an infinite number of possible solutions for the displacement components. However, by understanding the viewing geometry of the two acquisitions (even before observations are made), we can define the null line. The null line represents the direction in which the two LOS observations have zero sensitivity, meaning no displacement can be observed along this direction. It is formed by the intersection of two null planes—one associated with the ascending LOS and the other with the descending LOS. Visually, these planes intersect to create the null line, which is fully described by its azimuth angle ϕ and elevation angle ζ (Figure 2.5). The significance of the null line in InSAR interpretation is that displacement in the direction of the null line cannot be detected by the satellite geometry. Therefore, knowing the orientation of the null line is crucial before conducting an InSAR survey, as it defines the direction in which the system cannot observe any ground motion. This orientation can be calculated by taking the cross-product of the two normal vectors (the LoS unit vectors) of the ascending and descending acquisitions (Brouwer and Hanssen 2023):

$$n = \widehat{u_A} \times \widehat{u_D} \tag{4}$$

Although the nature of the problem cannot be formally solved, standardizing InSAR product generation and interpretation is proposed in the literature (Brouwer and Hanssen 2023). According to that study, there are two primary recommendations for handling this issue: the physical option and the geometric option.

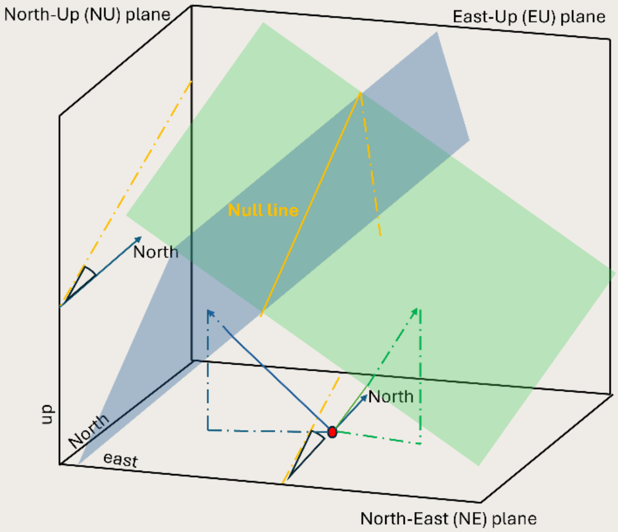

Figure 2.5 Illustration of the null line formed by the intersection of two null planes from ascending and descending LOS observations. Adapted from (Brouwer and Hanssen 2023).

The first option involves changing the orientation of the Cartesian reference frame based on prior physical knowledge. For example, if the system under observation, such as a landslide or glacier, is influenced by gravity, the displacement vector can be assumed to lie within a 2D vertical plane. In this case, the frame is rotated so that one direction (such as the longitudinal direction of a linear infrastructure) can be potentially assumed to be displacement-free. However, this approach comes with the risk of introducing biased estimates if the reference frame is misaligned.

The second option, which is more geometrically rigorous, involves using a Null-Line aligned (NLA) Cartesian coordinate system. This approach takes advantage of the orientation of the null space and forces the orthogonal projection of the displacement vector onto a plane that is orthogonal to the null line. By doing this, the in-plane components (such as east and vertical) can be uniquely and unbiasedly estimated, while avoiding bias from the ignored displacement direction.

When only one LoS observation is available, it is possible to project the displacement on to any desired direction. For instance, projecting the observed displacement onto the vertical direction can provide an estimate of vertical ground movement. This projection is performed as an oblique projection onto the vertical axis and is represented by the following formula:

$$d_{PoV} = \frac{1}{\cos\theta} d_{LOS} \qquad (5)$$

Here d_{PoV} represents the projection of the LOS displacement on to the vertical direction, and θ is the incidence angle of the radar signal. It is important to note that this projected value d_{PoV} does not equal the actual vertical displacement d_U. The reason is that the projection adjusts the LOS observation based on the satellite's viewing geometry and does not capture the true vertical displacement unless the satellite is observing directly from above, which is never the case.

In cases, when two LOS observations are available, such as from ascending and descending satellite passes, it is possible to project the observations onto a specific plane. One common approach is to project the LOS displacement vector onto the plane spanned by the east and vertical (EU) axes. The projection can be written as:

$$d_{PoEU} = \begin{bmatrix} 1 & 0 & 0 \\ 0 & 0 & 0 \\ 0 & 0 & 1 \end{bmatrix} U_{LOS} d_{LOS} \qquad (6)$$

where d_{PoEU} is the projection of d_{LOS} on to the EU plane. This projection provides estimates for the eastward d_E and vertical d_U displacement components. However, it is crucial to understand that these are not the true displacement components.

The final approach to address the underdetermined problem is to present the LOS observations unchanged as the ultimate product (Brouwer and Hanssen 2023).

The signal received by the SAR antenna contains an amplitude, which depends on the intensity of the reflection on Earth and is influenced by the surface's roughness, and a phase, which carries the distance information between the satellite and the ground target (Hanssen and Klees 1998). By comparing the phase differences between multiple SAR images taken at different times, it is possible to detect very small changes in the Earth's surface. Differential Interferometric Synthetic Aperture Radar (D-InSAR) is a technique that enhances InSAR by isolating the deformation signal through the removal of the topographic phase component from the interferogram (Zebker et al. 1994).

The basic principle of D-InSAR involves the generation of interferograms, which are images formed by the difference in phase information between two SAR images taken at different times. By differentiating these interferograms, we can detect changes in phase information that correspond to surface deformations. This technique considers two SAR complex images, I_1 and I_2, taken at different times, t_1 and t_2: The pixel value of i from refrence and secondary radar image is given by:

$$I_{1_i} = A_{1_i} \exp\left(j\varphi_{1_i}\right) \tag{7}$$

$$I_{2_i} = A_{2_i} \exp\left(j\varphi_{2_i}\right) \tag{8}$$

where A_{1_i} and A_{2_i} are the amplitudes of the pixel i in the two images, and φ_{1_i} and φ_{2_i} are the phases of the pixel i in the two images. The complex interferogram is calculated as:

$$I_{1_i} {I_{2_i}}^* = A_{1_i} A_{2_i} \exp\left(j(\varphi_{1_i} - \varphi_{2_i})\right) \tag{9}$$

where ${I_{2_i}}^*$ is the complex conjugate of I_{2_i}. The resulting interferogram contains both amplitude and phase information. The phase difference $\Delta\phi_{Interferogram}$ is wrapped within the range of $-\pi$ to $+\pi$. The observed phase values φ_{1_i} and φ_{2_i} in the images are given by:

$$\varphi_{1_i} = -\frac{2\pi 2R_1}{\lambda} + \varphi_{Scat,1_i} \tag{10}$$

$$\varphi_{2_i} = -\frac{2\pi 2R_2}{\lambda} + \varphi_{Scat,2_i} \tag{11}$$

where R_1 and R_2 are geometric distances between the radar sensor and the target on the ground during the first and second image acquisitions, and $\varphi_{Scat,1_i}$ and $\varphi_{Scat,2_i}$ refer to the contributions of the scattering phases in both images. If the In case the scattering characteristics are equal during both acquisitions, the interfrometric phase for pixel i can be given by (Hanssen 2001):

$$\Delta\phi_{Interferogram,i} = \varphi_{1_i} - \varphi_{2_i} = -\frac{4\pi\Delta R}{\lambda} \tag{12}$$

For accurate interferogram generation, several preprocessing steps are essential. These include calibration, radiometric correction, and co-registration of SAR images. Calibration involves correcting sensor-specific biases to ensure the accuracy of the radar signal. Radiometric correction adjusts for variations in signal strength caused by differences in the surface reflectivity and sensor characteristics. Co-registration aligns multiple SAR images to a common grid, ensuring that each pixel corresponds to the same ground location across all images (Zhai and Whang 2007). This step is crucial for minimizing errors in phase difference calculations and improving the overall quality of the interferometric products.

After the essential preprocessing steps, phase difference $\Delta\phi_{Interferogarm}$ can be further calculated and decomposed as:

$$\Delta\phi_{Interferogram} = \Delta\phi_{topo} + \Delta\phi_{disp} + \Delta\phi_{atm} + \Delta\phi_{orb} + \Delta\phi_{flat} + \Delta\phi_{noise} \tag{13}$$

Here, $\Delta\phi_{topo}$ is the phase component due to topography, $\Delta\phi_{disp}$ is the phase component due to displacement, $\Delta\phi_{atm}$ is the phase component due to atmospheric delays, $\Delta\phi_{orb}$ is the phase component due to orbital errors, $\Delta\phi_{flat}$ is the flat Earth component (also known as the reference plane phase) and $\Delta\phi_{noise}$ is the phase noise. By using a DEM, the topographic phase $\Delta\phi_{topo}$ can be simulated and subtracted from the total phase difference $\Delta\phi_{Interferogram}$ (Xue et al. 2020):

$$\Delta\phi_{topo} = \frac{4\pi}{\lambda} \cdot \left(\frac{h}{\rho \sin\theta}\right) \tag{14}$$

where h is the height difference between the SAR satellite and the ground surface, λ is the wavelength of the radar signal, ρ is the perpendicular baseline, and θ is the angle between the baseline and the radar line of sight. Additionally $\Delta\phi_{flat}$ caused by the phase difference at different positions on the reference plane and is proportional to the parallel baseline $B_{||}$ (Xue et al. 2020):

$$\Delta\phi_{flat} = 2\pi \cdot \frac{B_{||}}{\lambda} \tag{15}$$

After subtracting the topographic phase and flat Earth components, the remaining phase difference includes contributions from displacement, atmospheric delays, orbital errors, and noise. To further refine the deformation signal, multiple interferograms can be used to reduce the atmospheric effects and noise. Many techniques are introduced in the literature, such as Permanent (also persistent) Scatterers InSAR (PS-InSAR) (Ferretti et al. 2000; Ferretti and Rocca 2001), Small Baseline Subset (SBAS) (Berardino et al. 2002).

Persistent Scatterer Interferometry (PS-InSAR) is an advanced InSAR technique that improves the accuracy and reliability of deformation measurements by focusing on stable radar targets, known as Persistent Scatterers (PS) (Hooper and Zebker, 2007). These are typically man-made structures or natural features that reflect radar signals consistently over time (Perissin and Wang 2010). PS-InSAR can measure millimeter-level displacements, making it highly effective for long-term monitoring of ground deformation in the region with an even lower rate of deformation (Suresh et al. 2019). To address the various errors that can affect InSAR measurements, the Single Master PS-InSAR technique, as implemented in the Stanford Method for Persistent Scatterers (StaMPS) software, effectively mitigates these error components through a combination of data stacking and error modeling. The Single Master approach involves selecting one SAR image as the reference (master) and generating all interferograms using this master image against other images (slaves). Figure 2.6 illustrates an example of a star graph of perpendicular baseline versus temporal baseline between pairs of images, illustrating the selection of a single master image (brown dot) and its relative position to multiple slave images (blue dots) for interferogram formation.

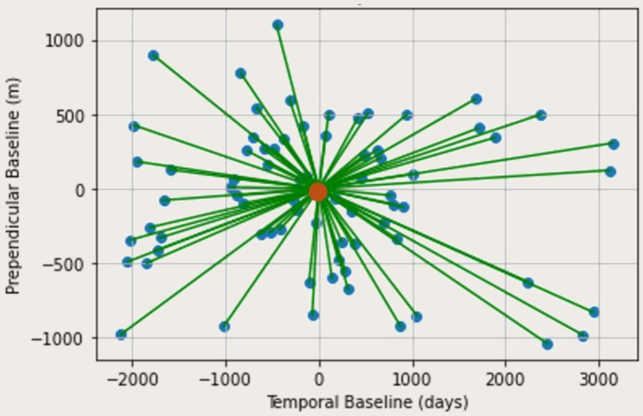

Figure 2.6 Graph of perpendicular baseline versus temporal baseline, illustrating the selection of a single master image (brown dot) and its relative position to multiple slave images (blue dots) for interferogram formation.

The workflow in StaMPS is designed to select PSs and compute their displacement history by following the principles of the PS-InSAR technique. This involves several key steps: data collection and preprocessing, interferogram formation, PS identification, phase model decomposition, phase unwrapping, estimating deformation and removing other components, time series analysis. Each of these steps relies on specific formulations and mathematical models (El Rai and Simonetto 2009; Sousa et al. 2010; Bayer et al. 2017).

Initially, the workflow selects PSs by considering a constant velocity model for target motion. Pixels are selected based on this model, and their phase history is analyzed. Only pixels with a history consistent with the functional model are included as final PS candidates. When using the PS-InSAR technique, the initial selection of PSs is based on a specific model or assumption about how the ground is deforming. Typically, this model assumes a constant velocity of deformation over time. If the actual ground deformation does not follow this assumed model (e.g., if it is non-linear, variable, or follows a different pattern), then the technique might not correctly identify all the relevant PS. As a result, the method might not be able to accurately measure or detect the true deformation, limiting its effectiveness and applicability in such cases. This can limit the application of the technique if the actual deformation model deviates from the initial hypothesis (Mancini et al. 2021).

In the StaMPS method, the initial selection of PS candidates is performed based on amplitude analysis (Ferretti et al. 2001; Chen et al. 2022). The statistical relationship between amplitude and phase stabilities is exploited, using a high value of the amplitude dispersion index (DA) as a threshold (Ferretti et al. 2001; Sousa et al. 2011). DA is defined as:

$$DA = \frac{\sigma_A}{\mu_A} \qquad (16)$$

where σ_A is the standard deviation, and μ_A is the mean of a series of amplitude values. StaMPS uses the statistical relationship between amplitude stability and phase stability to reduce the initial number of pixels for phase analysis. In some studies, a threshold value of approximately 0.4 is used (Yang et al. 2022), however, it is important to note that this threshold is not universally applicable and depends on various factors, including the environmental conditions. In StaMPS, the threshold for candidate Persistent Scatterers (PS) is often set higher than in other software, such as the Delft PSI processing package (DePSI), where a more conservative value around 0.25 is often used. This is because, in StaMPS, the final selection of PS is based on phase analysis, allowing for a higher initial threshold. (Ferretti et al. 2001). Studies by Hooper et al. (2007) have shown that using a threshold lower than 0.4 results in the selection of the largest number of stable PS while also reducing the computational effort for phase analysis.

After selecting a subset of pixels as initial candidates, the phase stability for each pixel is estimated using phase analysis, based on the assumption that deformation is spatially correlated (Zhang et al. 2015; Ansar et al. 2022). Consequently, signals associated with isolated movement of individual bright scatterers may be missed and considered as noise. The phase observations are “wrapped,” meaning only the fractional phase is measured, not the integer number of cycles from the satellite to the Earth's surface (Crosetto et al. 2016; El Kamali et al. 2020). Phase unwrapping resolves the ambiguity in phase measurements, which are initially wrapped within the interval $[-\pi, +\pi]$. This process is essential to reconstruct the true phase signal and involves minimizing phase differences between neighboring pixels while ensuring consistency. Various algorithms exist for phase unwrapping, such as the Minimum Cost Flow (MCF) algorithm, which seeks to minimize phase discontinuities in a wrapped phase map (Eineder et al. 1998).

However, the StaMPS software employs a

different approach for phase unwrapping, employed specifically for PS-InSAR applications. StaMPS uses a technique called 3D phase unwrapping. This method is designed to work effectively in the context of PS-InSAR by employing the phase gradients in x, y, and time t directions (Hooper and Zebker 2007). This technique is implemented within a software package called Statistical-Cost Network-Flow Algorithm for Phase Unwrapping (SNAPHU), which utilizes a statistical-cost, network-flow model to determine the most probable solution for phase unwrapping (Chen and Zebker 2000; 2001; 2002). Some widely used InSAR software packages including StaMPS are benefiting from this algorithm (Hooper et al. 2012).

SNAPHU is an advanced algorithm designed to handle phase unwrapping problems efficiently, particularly in the context of interferometric SAR applications (Yu et al. 2019). The primary challenge in phase unwrapping is to correctly estimate the absolute phase values from the wrapped phase data, which are inherently modulo-2π ambiguous. SNAPHU approaches this by modeling the phase unwrapping task as an optimization problem where the goal is to minimize a cost function that reflects the likelihood of phase discontinuities. Phase observations of neighboring PS candidates are processed through a band-pass filter, which includes an adaptive phase filter and a low-pass filter applied in the frequency domain. This method selects the candidates with the lowest residual noise (Liu 2013). Each pixel is initially weighted by setting the amplitude in all interferograms to an estimate of the signal-to-noise ratio (SNR) for the pixel, which in the first iteration is estimated from DA. The SNR is refined using residuals in subsequent iterations. Once the algorithm converges on estimates for the phase stability of each pixel, those most likely to be PS pixels are selected, with a threshold determined by the acceptable fraction of false positives. Additionally, pixels that appear stable only in a subset of the interferograms or those influenced by scatterers in adjacent PS pixels may be excluded (Sousa et al. 2011). A phase stability indicator, γ_x which is based on temporal coherence estimator, is used to assess whether a pixel qualifies as a PS:

$$\gamma_x = \frac{1}{N}\left|\sum_{i=1}^{N} exp\{j(\phi_{int,x,i} - \bar{\phi}_{int,x,i} - \hat{\phi}_{int,x,i})\}\right| \tag{17}$$

where N is the number of interferograms, and $\hat{\phi}_{int,x,i}$ is the estimate of the wrapped phase $\phi_{int,x,i}$ of the x-th pixel in the i-th flattened and topographically corrected interferogram. The root-mean-square change in coherence, γ_x, is calculated after each iteration. When this value ceases to decrease, the solution has converged, and the algorithm stops iterating. Pixels are then selected based on their probability of being PS pixels, considering their amplitude dispersion and γ_x (Hooper et al. 2007)

Once the PSs are selected, their phase is corrected for spatially uncorrelated look angle (SULA) errors using a DEM. If the phase difference between neighboring PSs, after SULA correction, is less than π, the phase values can be unwrapped. The primary observation in PSI is the double difference between master and slave images for nearby PSs (Hanssen 2004). This double difference, incorporating both temporal and spatial differences, requires a reference in both time (master image) and space (reference PS or area). After phase unwrapping, high-pass filtering in time and low-pass filtering in space can be applied to mitigate spatially correlated errors such as atmospheric and orbital effects. The remaining signal represents deformation and spatially uncorrelated errors, which can be modeled as noise (Sousa et al. 2010; 2011).

After the generation of the interferogram stack, PS selection, phase unwrapping, and isolating of the deformation phase in each interferogram, the construction of time series in PS-InSAR is conducted. This involves transforming phase information from multiple interferograms into a coherent series of displacement measurements over time. A mathematical model, often assuming linear or seasonal deformation, is fitted to the unwrapped phase data to relate the observed phase differences to ground displacement over time. This model helps to interpolate the displacement at each PS for times when no SAR image is available. The unwrapped phases from the interferograms are used to solve an inverse problem, where the goal is to estimate the incremental displacements that occurred between each pair of acquisition dates. This involves setting up and solving a system of linear equations that describe the relationship between phase differences and ground displacement:

$$\Delta\phi = 4\pi \cdot \frac{\Delta d}{\lambda} \tag{18}$$

where $\Delta\phi$ is the phase difference, Δd is the displacement, and λ is the radar wavelength. By integrating the incremental displacements over time, a cumulative displacement time series is constructed for each PS point. This provides a detailed temporal profile of ground deformation:

$$d(t_n) = d(t_1) + \sum_{i=1}^{n-1} \Delta\mathrm{d}(t_i, t_{i+1}) \tag{19}$$

where $d(t_n)$ is the cumulative displacement at time t_n, and $\Delta\mathrm{d}(t_i, t_{i+1})$ is the incremental displacement between times t_i and t_{i+1}.

By analyzing the time series data, long-term trends in ground deformation can be identified. By mapping the displacement time series for all PS points, spatial patterns of deformation can be analyzed. Techniques such as spatial autocorrelation (e.g., Moran's I) and clustering (e.g., K-means) can help identify areas with similar deformation behaviors, indicating underlying geological or anthropogenic processes.

Errors from atmospheric delays and orbital inaccuracies are mitigated using models and filtering techniques. High-pass filtering in the temporal domain removes long-wavelength atmospheric noise, while low-pass filtering in the spatial domain reduces high-frequency phase noise.

Decomposing the time series into trend, seasonal, and residual components can provide insights into the nature of the deformation. Methods such as Seasonal-Trend decomposition using Loess (STL) can separate these components, helping to distinguish between consistent trends and periodic variations

2.2. Hydrogeological Modeling

Hydrogeological modeling is a crucial component in understanding subsurface water flow and managing groundwater resources effectively. The use of 3D hydrogeological models allows for a detailed representation of the complex interactions within groundwater systems. One of the most widely used software tools for this purpose is MODFLOW, developed by the U.S. Geological Survey (McDonald and Harbaugh 1988). This software, when integrated with Groundwater Modeling System (GMS), provides a powerful platform for simulating groundwater flow and contaminant transport in three dimensions.

In our study on subsidence, MODFLOW plays an essential role in accurately modeling the groundwater flow, which is a critical factor influencing ground deformation. While MODFLOW itself is not used for geomechanical modeling, the detailed groundwater pressures deduced from groundwater flow simulations that it provides are crucial inputs for our geomechanical analyses.

By incorporating the variations in groundwater levels and pressures simulated by MODFLOW, we can more accurately analyze subsidence phenomena. This integration enables us to achieve a more precise understanding of the swelling and consolidation processes.

MODFLOW operates on the principles of groundwater flow equations derived from Darcy's law and the continuity equation. Darcy's law states that the flow rate through a porous medium is proportional to the hydraulic gradient and the hydraulic conductivity of the medium. Mathematically, this can be expressed as:

$$q = -K\nabla h \tag{20}$$

where q is the specific discharge (m/s), K is the hydraulic conductivity (m/s) and ∇h is the hydraulic gradient (dimensionless). The continuity equation for incompressible flow, where the density ρ is constant, which ensures mass conservation, is given by:

$$\nabla \cdot \mathrm{q} + \frac{\partial n}{\partial t} = 0 \tag{21}$$

where n is the storage coefficient (dimensionless), and t is time. Combining Darcy's law with the continuity equation for steady-state flow in three dimensions, we obtain:

$$\frac{\partial}{\partial x}\left(K_{xx}\frac{\partial h}{\partial x}\right) + \frac{\partial}{\partial y}\left(K_{yy}\frac{\partial h}{\partial y}\right) + \frac{\partial}{\partial z}\left(K_{zz}\frac{\partial h}{\partial z}\right) + W = 0 \tag{22}$$

where K_{xx}, K_{yy}, and K_{zz} are the hydraulic conductivities in the x, y, and z directions, respectively, and W is the water flow rate per unit area of the geological medium that is injected $(W > 0)$or withdrawn $(W < 0)$. All this equation's terms are in (m^3/m^2 m s) or (m/s) showing the volume of flowing water per unit cross-sectional area of the porous medium, per second.

For transient conditions, where storage changes must be accounted for, combining Darcy's law with the continuity equation in three dimensions we obtain:

$$\frac{\partial}{\partial x}\left(K_{xx}\frac{\partial h}{\partial x}\right)+\frac{\partial}{\partial y}\left(K_{yy}\frac{\partial h}{\partial y}\right)+\left(K_{zz}\frac{\partial h}{\partial z}\right)+W=S_S\frac{\partial h}{\partial t} \tag{23}$$

This equation is the development of Equation (22) under transient conditions. In Equation (23) all terms are in (s^{-1}) expressing the volume of flowing water per volume of porous medium per unit of time. In this equation S_S is the specific storage coefficient which is the volume of groundwater gained or released per unit *volume* of saturated porous medium and per unit change in piezometric head h.

In MODFLOW, these 3D partial differential equations are simplified and solved using a quasi-3D approach. The model uses a 2D partial differential equation that is solved using finite-difference methods (Igboekwe MU and Amos-Uhegbu 2011) layer per layer. For the 2D horizontal plane, considering the Dupuit assumption, the steady-state groundwater flow Equation (22) becomes:

$$\frac{\partial}{\partial x}\left(T_{xx}\frac{\partial h}{\partial x}\right)+\frac{\partial}{\partial y}\left(T_{yy}\frac{\partial h}{\partial y}\right)+W=0 \tag{24}$$

For transient conditions, the Equation (23) becomes:

$$\frac{\partial}{\partial x}\left(T_{xx}\frac{\partial h}{\partial x}\right)+\frac{\partial}{\partial y}\left(T_{yy}\frac{\partial h}{\partial y}\right)+W=S\frac{\partial h}{\partial t} \tag{25}$$

where T_{xx} and T_{yy} are the transmissivities in the x and y directions, respectively and S is the volume of groundwater gained or released per unit *area* of saturated porous medium and per unit change in piezometric head h. For more details on these concepts, readers are referred to (Dassargues 2018).

In MODFLOW, the model domain is discretized into a grid of cells, each representing a portion of the aquifer. The hydraulic properties such as hydraulic conductivity, specific yield, and specific storage coefficient are assigned to each cell based on field data or geological interpretations. Boundary conditions and initial conditions are specified to simulate real-world scenarios (Harbaugh et al. 2000).

GMS enhances MODFLOW by providing a graphical user interface that simplifies the construction, visualization, and calibration of complex 3D groundwater models (Aquaveo 2023). GMS supports various pre-processing and post-processing tools, enabling users to create detailed geological models, assign properties, and visualize simulation results effectively.

To enhance simulation accuracy in modeling subsidence, compressible layers must be finely discretized into sublayers, maintaining consistent hydrogeological and geomechanical parameters. This fine discretization improves the representation of water pressure distribution within each layer, which is particularly critical for thick, low-permeability layers.

In 3D hydrogeological modeling, the conceptual model is critical as it defines the hydrostratigraphy and hydrodynamic characteristics of the aquifer system. The conceptual model includes information on aquifer boundaries, recharge and discharge areas, and the interaction between surface water and groundwater (Tóth 1970; Anderson et al., 2015). This information is used to set up the numerical model in MODFLOW, where the model domain is divided into layers representing different hydrogeological units.

MODFLOW's capability to simulate various hydrogeological processes makes it suitable for a wide range of applications, including groundwater resource management, contamination assessment, and aquifer remediation. The software can simulate steady-state and transient flow conditions (Zheng and Wang 1999).

2.3. Geomechanical Modeling

Pumping or draining groundwater can cause land subsidence through settlement. This phenomenon is explained by the Terzaghi principle for saturated porous media (Terzaghi 1925):

$$\sigma = \sigma' + p \tag{26}$$

Here σ' is the effective stress, p is the water pressure, and σ is the total stress, all expressed in Pa [$ML^{-1}T^{-2}$]. Effective stress, the 'grain to grain' stress within the solid matrix of the medium, drives consolidation. When water pressure decreases in a saturated geological medium, effective stress increases, inducing consolidation (Dassargues 2018).

In confined conditions, the total stress may often be considered unchanged as the pressure decreases through the confined layers and is very slow to propagate, and the saturation of the upper layers can be maintained by recharging from the surface. In unconfined conditions, a portion of the effective stress decrease is balanced by a possible decrease of the total stress by lowering the total saturated column (Dassargues 1995; Dassargues 2018). This is important to note that land subsidence does not necessarily require a partial desaturation of the geological formation. Any decrease in pore pressure, leading to an increase in effective stress, is sufficient to trigger the consolidation process. Consolidation is a delayed process due to the slow change in groundwater storage, influenced by the compressibility of the saturated porous medium under transient flow conditions. This geomechanical behavior in compressible layers made of clay, peat, and loam can be described by elastic, elastoplastic, or visco-elastoplastic rheological laws. Over time, the viscous component of this process is considered 'secondary consolidation' and is often neglected. The volume compressibility of a saturated porous medium is expressed as:

$$-\frac{1}{V}\frac{\partial V}{\partial t} = \alpha \frac{\partial \sigma'}{\partial t} \tag{27}$$

Here α is the volume compressibility of the porous medium [Pa^{-1}]. A decrease in total volume V [L^3] is expected with an increase in effective stress. Volume compressibility depends on the value of σ' and thus the pre-consolidation effective stress σ'_{max}.

Land subsidence induced by human activities, such as groundwater extraction, is experienced in regions with compressible sediments. These layers, including recent fluviatile, coastal, estuarine, deltaic, and lacustrine sediments (Poland and Davis 1969), may be under-consolidated, meaning they are at a lower effective stress than expected at their depth in a saturated column in equilibrium.

Geomechanical data critical to understanding this process include the specific storage coefficient S_S, which relates to the volumetric compressibility of the saturated medium. Oedometer tests, which are one-dimensional vertical consolidation lab tests in drained conditions, provide compressibility assessments. These values depend on the effective stress state and whether it is above or below the pre-consolidation effective stress σ'_{max}.

A ‘compression constant’ C and a ‘swelling constant’ A can be defined as describing the effective stress-strain relationship. These last are defined in a linearized $\ln \sigma'$, relative deformation) diagram, which shows the presumed elasto-plastic geomechanical behaviour. The 'swelling constant' A illustrates the reversible elastic behaviour (below the pre-consolidation effective stress), whereas the 'compression constant' C describes the non-reversible plastic behaviour (above the pre-consolidation effective stress) (Figure 2.7).

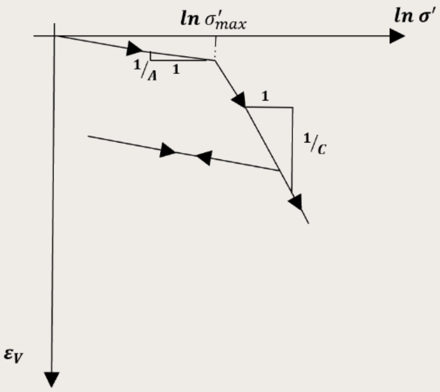

Figure 2.7 Diagram of relative deformation (ε_V) in function of the natural logarithm of effective stress $(\ln \sigma')$ (modified from Dassargues (2018))

Similarly, in a linearized, $(\log \sigma'$, void ratio $e)$ diagram, a compression index C_C and a swelling index are depicted C_S (Figure 2.8). Oedometer tests allow us to determine those characteristics as cited in various studies (Lambe 1951; Jorgensen 1980; Yoon et al. 2011; Dassargues 2018). Considering the intrinsic connection between the specific storage coefficient and compressibility values, groundwater literature often distinguishes the elastic and inelastic (plastic) geomechanical behaviours via elastic and inelastic specific storage coefficients (S_{ske} and S_{skv}) (Zhuang et al. 2017; Li et al. 2022).

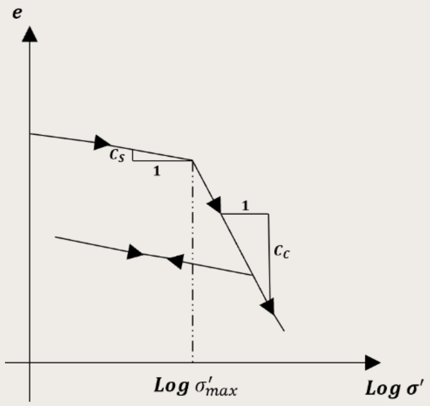

Figure 2.8 Diagram of void ratio (e) in function of the logarithm of effective stress $(log\ \sigma')$ (modified from Dassargues (2018))

Using the oedometer test results, the elastic (S_{ske}) and inelastic skeletal specific storage (S_{skv}) coefficients introduced in the 1D-geomechanical model used in this study can be calculated (Hoffmann 2003). First, compressibility α is calculated using the results of oedometer tests in terms of geomechanical parameters (A, C) (Dassargues 2018):

$$\begin{cases} \alpha = \frac{1}{A.\sigma'} & \sigma' < \sigma'_{max} \\ \alpha = \frac{1}{C.\sigma'} & \sigma' \geq \sigma'_{max} \end{cases} \tag{28}$$

Alternatively, if the provided geomechanical parameters are (C_C, C_S):

$$\begin{cases} \alpha = 0.434 \times \frac{C_S}{\sigma'} & \sigma' < \sigma'_{max} \\ \alpha = 0.434 \times \frac{C_C}{\sigma'} & \sigma' \geq \sigma'_{max} \end{cases} \tag{29}$$

Once the compressibility values α were obtained, the specific storage coefficients can be directly written in relation to volume compressibility (Pa^{-1}) [M^{-1}LT^{2}] (Dassargues 2018):

$$S_S = \rho g \alpha \tag{30}$$

where ρ is the density of water and g is the acceleration due to gravity. Finally, to obtain the elastic and inelastic skeletal specific storage coefficients for the geomechanical model used in this study, the specific storage values were multiplied by the thickness of each layer b (Hoffmann et al. 2003):

$$\begin{cases} S_{ske} = S_{S\,(elastic)} \times b & \sigma' < \sigma'_{max} \\ S_{skv} = S_{S\,(inelastic)} \times b & \sigma' \geq \sigma'_{max} \end{cases} \qquad (31)$$

where S_{ske} and S_{skv} are the inelastic and elastic skeletal specific storage coefficients of each sublayer. In the 1D geomechanical model used in this study, these parameters are crucial for the vertical deformation simulation in each layer.

From the pore pressure and effective stress calculated at each time step, a 1D vertical geomechanical model simulates deformations through these equations:

$$\begin{cases} \Delta \mathrm{b} = S_{ske} \times \Delta h & h < h_{min} \\ \Delta \mathrm{b} = S_{skv} \times \Delta h & h \geq h_{min} \end{cases} \qquad (32)$$

where h is the hydraulic head at a given timestep, and h_{min} is the preconsolidation head corresponding to the maximum preconsolidation stress.

To enhance simulation accuracy in modeling subsidence, particularly in this study, compressible layers must be finely discretized into sublayers, maintaining consistent hydrogeological and geomechanical parameters. This fine discretization improves the representation of water pressure distribution within each layer, which is particularly critical for thick, low-permeability layers. Using these principles, subsidence simulations in this study can more accurately capture the time-dependent deformations in hydrogeological materials, reflecting both elastic and inelastic characteristics. This approach provides a comprehensive theoretical background for understanding and predicting land subsidence behavior effectively, specifically for the purposes of this study.

3

Subsidence in Antwerp Harbour: PS-InSAR and Coupled Hydrogeological-Geomechanical Modeling

This chapter is based on the paper titled, "Challenges in comparing land subsidence measurements by PS-InSAR with simulations from coupled hydro-geomechanical modeling: a case study in Antwerp harbour," by A. Choopani, P. Orban, P. Y. Declercq, X. Devleeschouwer, and A. Dassargues, which is currently under review at the Hydrogeology Journal.

3.1. Abstract

Land subsidence is a serious problem, especially in rapidly urbanizing areas. Monitoring the subsidence velocities and their evolution in time is valuable but not sufficient to determine the ongoing processes, causes, and contributing components. Interferometric Synthetic Aperture Radar (InSAR) technology has advanced over the last 30 years, enabling better spatial resolution for detecting surface deformation. However, to explain the geomechanical or hydrogeological causes of subsidence, additional tools and approaches are necessary. Studies that integrate a variety of geodetic observations, Global Navigation Satellite System campaigns, and the deployment of extensometers in various sublayers along with space-based InSAR measurements, provide valuable insight into the ongoing consolidation processes. Groundwater flow models coupled to geomechanical models provide physically consistent results of consolidation induced by water pressure decrease in pumped or drained aquifer-aquitard systems mainly made of loose and recent sediments. However, the conceptual choices for such consolidation computation may vary widely, potentially leading to biased results for comparison with measured values. Recent investigations have integrated various geodetic approaches to detect, quantify, and map the effective components of subsidence. A few of them address the actual limitations and challenges connected to the comparison between measurements and results from coupled models. In this paper, the most important practical and conceptual challenges are described starting from InSAR measurements until a valid comparison with the simulated values of consolidation. One practical case study of local land subsidence in Belgium is used as an illustration in a geological context of recent loose sediments.

3.2. Introduction

3.2.1. InSAR Technology

Interferometric Synthetic Aperture Radar (InSAR) measurements have provided new insights into land movement detection. Land subsidence or uplift due to pore pressure changes induced by pumping or drainage can make up most of these movements. To obtain reliable estimations of ground level motion, InSAR measurements require appropriate processing. InSAR effectively allows estimating land surface deformations over time. The displacement time series and land surface velocity map in the satellite Line Of Sight (LOS) are the two primary outputs. While these measurements provide an integrated estimation of consolidation occurring below the surface, they do not provide information about the specific layers affected by the consolidation processes. Nevertheless, their contribution to understanding ground movement remains invaluable. They have revealed cases that were previously undetected by other surveying techniques (Gambolati and Teatini 2015). InSAR generates an interferogram using a pair of complex SAR images acquired at two distinct times and from slightly differing orbital positions. By analyzing the phase difference between these two acquisitions, the displacement of the ground surface can be determined along the satellite LOS (Massonnet and Feigl 1998; Chen et al. 2020). The Global Positioning System (GPS) campaigns, subsoil elevation surveys using cable or pipe borehole extensometers, and leveling are traditional land subsidence assessment techniques that can provide data with millimeter-scale precision. However, these methods have several limitations. While some can provide continuous data, they often do not offer continuous spatial coverage. They can be costly and time-consuming, especially when monitoring large areas. While they are invaluable for specific applications (e.g., borehole extensometers allow for the detection of the consolidation in each individual layer), they might not always be the most practical choice for broad-scale and continuous monitoring (Zhou et al. 2019; Li et al. 2022). Multi-Temporal InSAR (MT-InSAR) technology, due to its extensive geographical coverage and higher precision, can detect displacements with millimeter-level precision in the vertical coordinate (z) (Ghorbani et al. 2022). Under optimal conditions, this offers a fine spatial resolution down to the meter scale in horizontal coordinates (x, y) and millimeter-level precision in the vertical coordinate (z) (Peng et al. 2022). This higher precision in the vertical dimension makes MT-InSAR particularly valuable for monitoring small ground movements over time, compensating for the typical centimeter-level precision in conventional InSAR by using multiple temporal acquisitions to enhance measurement accuracy. This is one of the most cost-effective methods for assessing ground surface displacement over large areas. Due to the link between water pressure in the geological layers and consolidation processes, InSAR has recently been employed as a basic dataset for the estimation of aquifer storage characteristics through inverse groundwater modeling (Chaussard et al. 2014; Miller and Shirzaei 2015; Miller et al. 2017; Motagh et al. 2017; Jiang et al. 2018; Gualandi and Liu 2021). Multi-temporal InSAR methods, including Persistent Scatterer Interferometric Synthetic Aperture Radar (PS-InSAR) (Ferretti et al. 2000; 2001) and the Small Baseline Subset (SBAS) technique (Berardino et al. 2002), are among the predominant categories of InSAR techniques. They are primarily employed to mitigate the effects of atmospheric distortions and topographic inaccuracies creating artifacts (Chen et al. 2021). Compared to PS-InSAR, the SBAS approach is more suitable for detecting displacement in areas with less stable or coherent reflectors, such as rural environments. However, the accuracy is primarily influenced by the characteristics of the Earth's surface, which can be compromised in vegetated regions with high temporal decorrelation (Xu et al. 2021). In highly vegetated regions or areas with significant surface changes, the temporal decorrelation can lead to challenges in phase unwrapping. Conversely, PS-InSAR identifies pixels exhibiting consistent and permanent scattering behavior over time. This enables the mapping of displacement patterns and quantifies surface motion over extended periods, thereby addressing the limitations of the conventional InSAR approach (Ferretti et al. 2000; 2001; 2007; Fiorentini et al. 2020). While the PS-InSAR technique is frequently regarded as optimal for estimating land surface movement in urban regions, the comparison of these estimations with results simulated by process-based geomechanical models coupled to hydrogeological models brings distinct challenges, as detailed in this paper.

3.2. 2. Subsidence Due to Groundwater Pumping or Drainage

Pumping or draining groundwater can lead to settlement, which in turn may result in land subsidence. This phenomenon has been recognized for many years and can be explained by using the concept of the Terzaghi principle, formulated in 1925 (Terzaghi, 1925) for saturated porous media:

$$\sigma = \sigma' + p \tag{33}$$

where σ' is the effective stress, p is the water pressure, and σ is the total stress, all expressed in Pa [$ML^{-1}T^{-2}$]. Effective stress is defined as the 'grain to grain' stress or the stress occurring within the solid matrix of the saturated medium.

Any increase in this effective stress is thus considered as the driver of consolidation. A decrease in water pressure in a saturated geological medium induces an increase in effective stress in both confined and unconfined conditions (Dassargues 2018). In confined conditions, the total stress may be considered unchanged as the pressure decrease through the confining layers is very slow to propagate, and the saturation of the upper layers can be maintained by the recharge from the surface. In unconfined conditions, a portion of the effective stress decrease is balanced by a possible decrease of the total stress by lowering the total saturated column (Dassargues 1995; Dassargues 2018).

This is important to note that land subsidence does not necessarily require a partial desaturation of the geological formation. Any decrease in pore pressure, leading to an increase in effective stress, is sufficient to trigger the consolidation process.

Consolidation can be a delayed compaction process due to the slow change of groundwater storage caused by the compressibility of the saturated porous medium under the transient flow and drained conditions. This geomechanical behavior occurring in the most compressible layers as clayey, peaty, and loamy loose sediments, can most often be described by elastic, elastoplastic, or visco-elastoplastic rheological laws. The viscous component, delayed in time, can also be invoked in the long term and considered as a 'secondary consolidation'.

The volume compressibility of a saturated porous medium is expressed by:

$$-\frac{1}{V}\frac{\partial V}{\partial t} = \alpha\frac{\partial \sigma'}{\partial t} \tag{34}$$

where α is the volume compressibility of the porous medium [Pa^{-1}], the negative sign is justified as a decrease of total volume V [L^3] is expected for an increase in effective stress. An important observation is that volume compressibility is not constant but depends on the value of σ' and thus also on the pre-consolidation effective stress σ'_{max} (i.e., the highest effective stress value previously applied to the considered porous medium).

Land subsidence induced by anthropogenic changes in groundwater conditions can be local or regional. The subsiding regions most often correspond to areas where compressible loose sediments are present. Compressible layers are made of recent fluviatile, coastal, estuarine, deltaic, and lacustrine sediments (Poland and Davis 1969). Under certain sedimentological circumstances, they can even be under-consolidated (i.e., at a lower effective stress than the expected one at the considered depth in a saturated column in equilibrium).

3.2. 3. Land Subsidence in Antwerp

This part of the study focuses on the land subsidence estimated, around Antwerp city, the second largest city in Belgium. Surface displacements in this area have been detected and mapped since the 1990s. This monitoring was achieved by employing the PS-InSAR space-based technique on ERS1/2, ENVISAT ASAR, and Sentinel-1A radar data (Declercq et al. 2021; Choopani et al. 2023). As a result, land subsidence measurements are available for this site during the periods between 1992–2001, 2003–2010, and 2016–2023. For this study, high-resolution TerraSAR-X data from 2019-2022 were also used. PS-InSAR provides insights into both the spatial extent and magnitude of surface deformation. Displacement magnitudes are presented as LOS velocity over specific observation periods and displacement time series. A global hydrogeological map (Figure 3.1) across Belgium and the neighbouring countries is provided.

Located on both riversides of the Scheldt, within Antwerp city limits, the harbour has seen progressive development. The elevation in the Scheldt polders varies from 0.5 to 5 m relative to Belgium reference altitude (Declercq et al. 2021). The region lies on low-lying polders in the upper reaches of the Sea Scheldt estuary (Figure 3.2).

Despite no significant groundwater extraction recorded in the area, subsidence spanning the entire Antwerp region has been observed since 1992 using PS-InSAR. The subsidence rates in the Antwerp city center differ from those in the harbour installations. In the habour area, land subsidence can be driven by different processes than groundwater pumping, such as the natural and over-consolidation of Holocene estuarine sediments due to backfill overload (8 m thick embankments) along the harbour docks, and the saturated-unsaturated consolidation of backfill materials (Figure 3.2).

To ensures a focused analysis of the subsidence due to changes in water pressure in the aquifers and aquitards while excluding the effects of compaction of the embankment, it was decided to choose a study area deliberately positioned outside the embankment limits.

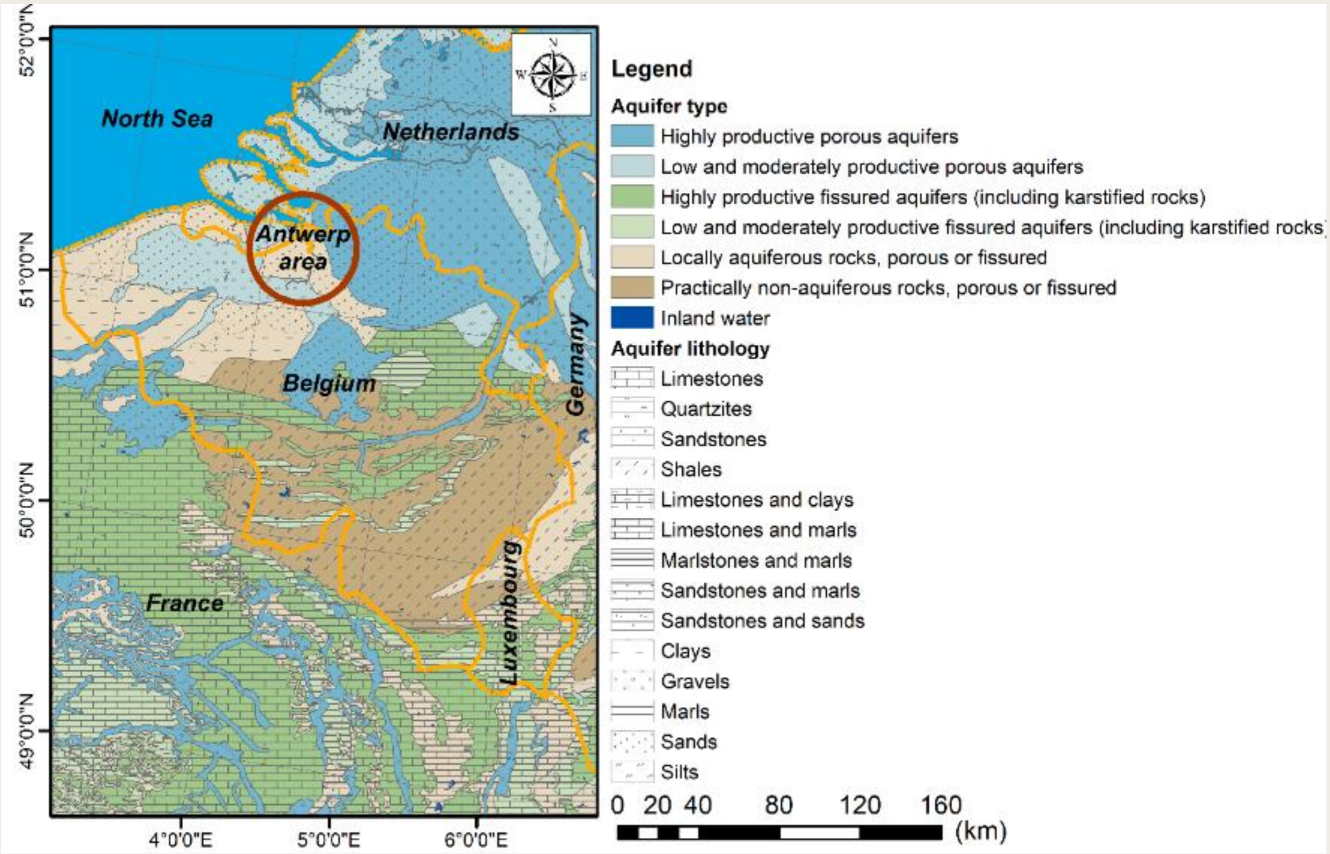

Figure 3.1 Global hydrogeological map. Data from the International Hydrogeological Map of Europe at a scale of 1:1,500,000 (IHME1500) (BGR and UNESCO, 2013)

To understand potential consolidation processes in the most compressible strata (Paleocene and Eocene) arising from pore pressure decreases in various Cenozoic aquifers (Figure 3.3), a 3D groundwater flow model coupled to a 1D-geomechanical model has been developed. This 3D groundwater flow model covers an area of 1.1 Km^2 and includes nine layers of loose sediments (Figure 3.3) The study area comprises nine main hydrogeological units up to a depth of 225 meters. These include four aquifers, four aquitards, and the uppermost layer, composed of mixed sand and clay. The uppermost layer (Layer 1) is the Quaternary Layer, including Polder deposits, characterized by mixed sand and clay. Below this (Layer 2) is the Pleistocene and Pliocene Aquifer System, which actually forms part of the broader Miocene aquifer and consists primarily of sandy deposits. Layer 3 is Boom Aquitard, composed of clay, which acts as a confining unit. Layer 4 is the Ruisbroek-Berg Aquifer, also known as the Upper Oligocene Aquifer, featuring sandy materials.

Layer 5 is the Tongeren Aquitard, another significant confining layer rich in clay. Layer 6 is the Lower Oligocene Aquifer, composed of sandy sediments. Layer 7 is the Bartoon Aquitard System, characterized by its clay composition. Layer 8 is the Ledo-Paniselian-Brusselian Aquifer System, consisting of mixed sand and clay. Finally, Layer 9 is the Paniselian Aquitard System, the deepest unit, mainly composed of clay.

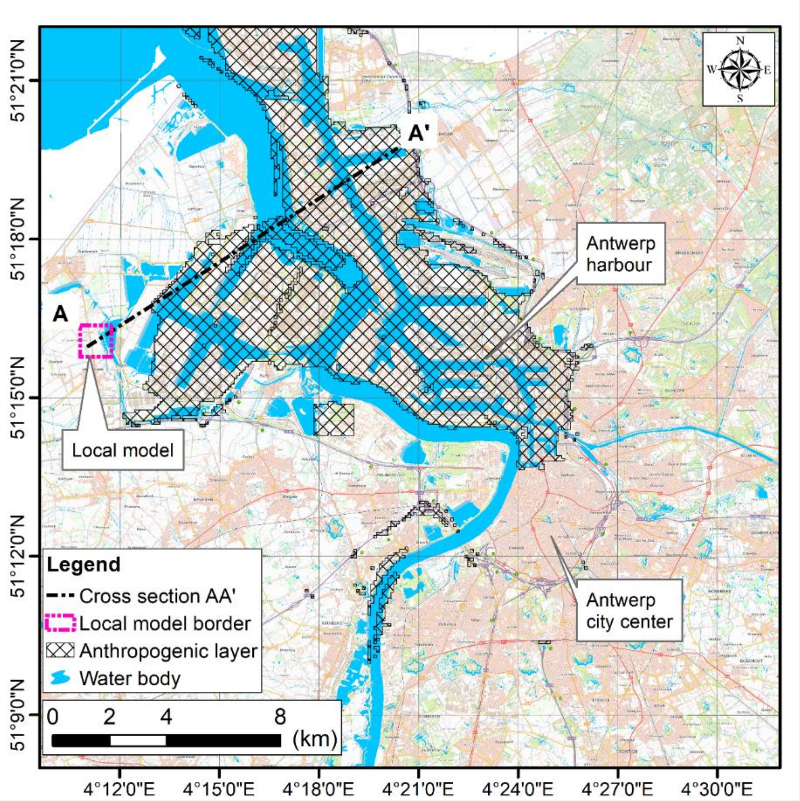

Figure 3.2 Location map of Antwerp region in Belgium. The location of the cross-section AA' (Figure 3.3) is highlighted (with a dashed black line) on the map. (The border of the Anthropogenic layer is from the Geological 3D model (v3.1))

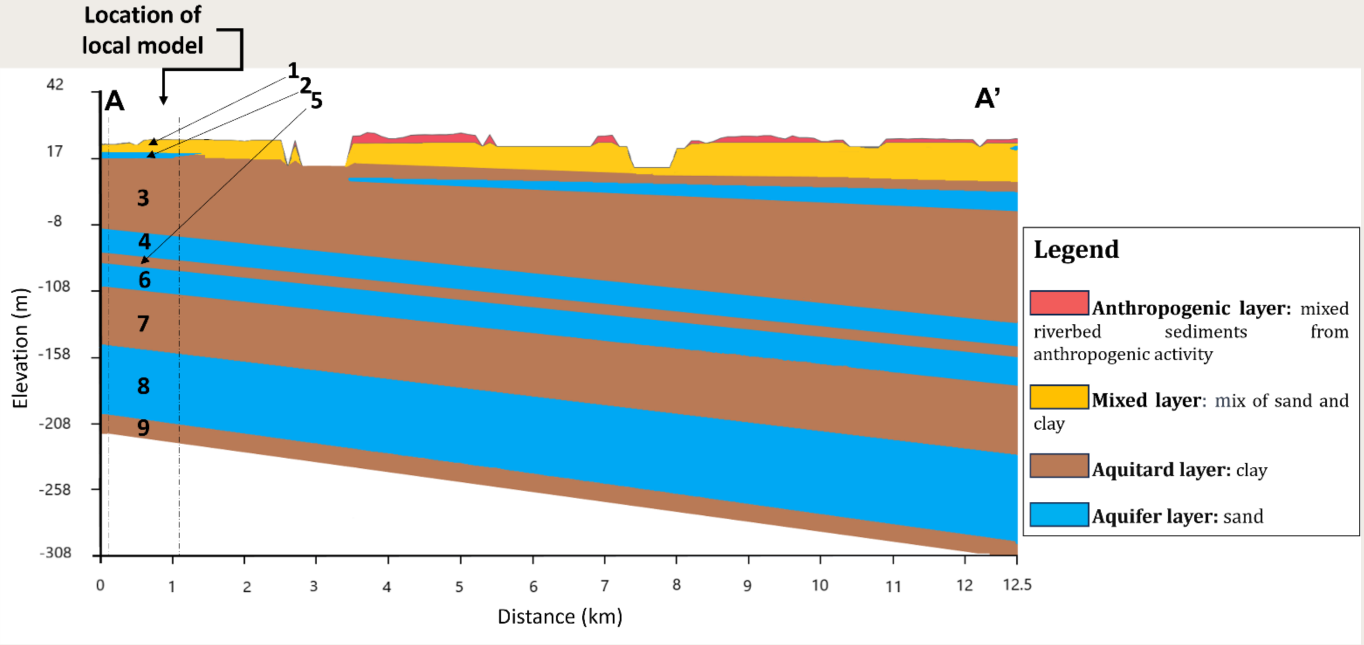

Figure 3.3 Simplified hydrogeological cross-section AA' (as drawn in Figure 3.2) showing in depth the interlayering between compressible clayey aquitards and sandy aquifers. Elevation values are given in m and above the Belgian reference level. The numbers shown on each layer represent the corresponding layer number in the model. This cross-section is based on an interpretation of data from the Geological 3D model (v3.1) and the Hydrogeological 3D model (v2.1) available on (DOV 2024).

In the subsequent section, we review the various methods and models employed for calculating land subsidence. The third section highlights challenges arising from the limited availability of hydrogeological and geomechanical data, using the case of Antwerp as an illustration. The issues related to the temporal gap between the periods of availability of stress factors data and the time series of subsidence estimated by PS-InSAR are also discussed. The fourth section delves into the needed simplifying assumptions that can impact the comparison between displacements detected by PS-InSAR with those simulated by the 1D-geomechanical model coupled to the groundwater flow model.

3.3. Land Subsidence Modeling

The phenomenon of land subsidence has been observed for centuries. Initially, occurrences were primarily attributed to natural causes such as tectonic activities, karstification, and the natural compaction of sedimentary basins (Heiken et al. 2013). By the late 19th and early 20th centuries, human activities, such as mining, gas or oil exploitation, and groundwater pumpings, introduced a new set of challenges (Reddish and Whittaker 2012). Coal extraction from underground mines, for instance, created voids that led to ground collapses (Forster 2000). In the 20th century, with growing urban centers and agricultural expansion, groundwater extraction became one of the primary causes of land subsidence. Extensive extraction from aquifers often resulted in a reduction of pore pressure, leading to the compaction of granular layers and subsidence at the surface (Poland and Davis 1969).

Some of the most notable cases of subsidence from groundwater extraction include the San Joaquin Valley in California and Mexico City (Galloway et al. 1999; Galloway and Riley 1999; Strozzi and Wegmuller 1999). Other significant global instances of subsidence have been recorded in locations (among many others) such as Bangkok (Phien-wej et al. 2006); Venice (Gambolati et al. 1974; Tosi et al. 2009; Zanchettin et al. 2021); Tokyo (Sato et al. 2006); Shanghai (Dassargues et al. 1993; Dong et al. 2014); Jakarta (Abidin et al., 2011); and Tehran (Tavakkoli Estahbanati and Dehghani, 2018).

These geohazards not only may impact infrastructures but also reduce the aquifer storage capacity, leading to a vicious cycle of further extraction and subsidence (Famiglietti, 2014).

The oil and gas industry are also confronted with significant subsidence issues due to hydrocarbon extraction. This is induced by reservoir and overburden layers compaction and subsequent surface subsidence (Geertsma, 1973; Ferretti 2014; Thienen-Visser et al. 2015). Predictive models are needed to possibly anticipate these changes, especially in coastal flat regions where land subsidence exacerbates flood risks (Wdowinski et al. 2016).

Initial efforts to model subsidence were largely empirical, particularly for groundwater-induced subsidence (Holzer and Bluntzer 1984). These models often drew correlations between water extraction volumes and observed land subsidence. Subsequently, models began to incorporate theoretical and mechanistic elements, integrating soil mechanics and hydrogelogy principles to simulate aquifer system compaction,and their results were compared with observed land subsidence. These models have been implemented, for example, in Pixley, California (Helm 1976); different areas in the United States (Gabrysch and

Bonnet 1975; Holzer and Galloway 2005); and in Iran (Motagh et al. 2007). Statistical and semi-empirical methods including regression analysis (Allen 1973; Duncan and Chang 1970; Poulos et al. 2001) and ’black box’ models (Phoon and Tang) were also developed. While regression analysis requires large datasets to establish these relationships between land subsidence and withdrawal volume, the ’black box’ method can work with limited data concerning the hydraulic and geomechanical properties of the layers. However, they offer lower reliability, especially if they are used for prediction with stresses that are out of the calibration range (Wang et al. 2019).

While empirical models provided initial insights into subsidence, they were constrained by encompassed assumptions of spatial-temporal uniformity, linear behaviour, a lack of mechanistic understanding, and a narrow focus on single variables, although a few did touch upon nonlinear behaviour with clear limitations (Burbey 2002; Domenico and Schwartz 1997; Galloway and Burbey 2011; Wang et al. 2019).

Building on a process-based approach, Terzaghi introduced his one-dimensional consolidation theory in 1925, bringing into focus the time-dependent settlement of saturated soils under load (Terzaghi 1925; Jaeger et al. 2009). This conceptual model linking the effective stress to the water pore pressure in saturated, compressible soils allows to couple groundwater flow calculation to geomechanical behaviour laws. The groundwater flow equation, considering Darcy law and the conservation of groundwater mass, can be coupled to 1D geomechanical laws to predict time-dependent compaction of clays (Terzaghi 1943; Hubbert 1957). While limitations are lying in simplicity and 1D dimensionality, this provided the first robust mathematical framework for understanding subsurface behaviour. Subsequent models focused on consolidation and subsidence phenomena, drawing from this work (Poland and Davis 1969). Following Terzaghi's work, Biot introduced a more encompassing poro-elastic theory in 1941, which considered the interaction between the soil skeleton deformation and the pore fluid movement in multiple dimensions (Biot 1941). The formulated differential equations combined considerations from both equilibrium and fluid dynamics. These first generations of mathematical equations offered a deeper understanding of the intricate deformation processes, fluid migration, and the distribution of stress within underground formations (Detournay and Cheng 1993). Over time, the importance of modeling the irreversible, or plastic, behavior became evident. This led to the incorporation of elasto-plastic formulations including compressibility coefficients that depend on the stress state and stress history (Wood 1990). In that framework, the Cam-Clay model emerged as a significant elastoplastic model for clays, providing insights into both consolidation and yield mechanisms (Schofield and Wroth 1968). More intricate models such as the Modified Cam-Clay for over-consolidated clays and the Hardening Soil Model for modeling stress-dependent stiffness and plastic behavior in soils were developed (Roscoe and Burland 1968; Schanz 1998; Schanz et al. 1999). All those models keep the essence of Cam-Clay family models where the elastic and plastic deformation upon consolidation process is separated by the vertical preconsolidation stress of the materials that correspond to the yielding limit upon 1D compression Viscoelastic models also emerged, blending theory and empirical observations to merge both elastic and viscous behaviours (Findley et al. 2013). Creep models capturing the time-dependent deformations experienced by saturated soils under constant effective stress loading (Yasuhara et al. 1988; Mitchell and Soga 2005), can simulate substantial subsidence (Seed 1965), emphasizing the importance of these models in geotechnical engineering.

In one-dimensional flow and consolidation modeling, lateral strains and drainage are typically disregarded, implying that the movement of fluid and associated deformations are assumed to occur predominantly in the vertical direction (Davis and Raymond 1965; Schiffman and Stein 1970; Yun 2002; Radhika et al. 2020). Semi-3D models, simulate horizontal groundwater flow in aquifers and vertical flow in aquitards, employing Terzaghi's 1D consolidation theory for soil deformation (Hu et al. 2004; Xu et al. 2008; Shen and Xu 2011). In the three-dimensional (3D) flow coupled with one-dimensional (1D) consolidation model, groundwater movement is computed in 3D, while compaction is calculated exclusively in the vertical direction (Gambolati and Freeze 1973; Shen et al. 2006; Shi et al. 2006; Xu et al. 2008). Finally, while Biot's 3D consolidation theory provides an all-encompassing representation of seepage, stress changes, and soil deformation, its extensive resource and data requirements limit its widespread application (Gambolati and Freeze 1973; Sukirman and Lewis 1994).

Given the complexity of the land subsidence processes, the shortcomings of analytical solutions became increasingly evident (Lewis and Schrefler 1987). Numerical methods, based on the Finite Difference Methods (FDM) and the Finite Element Methods (FEM) (Zienkiewicz and Taylor 1989) were used. Other techniques like the Boundary Element Method (BEM) (Mirsalari et al. 2017), meshfree or meshless methods (Khoshghalb and Khalili 2010), Lattice Boltzmann Method (LBM) (Kim et al. 2019), and Discontinuous Galerkin methods (Chen et al. 2013) can also address the complex geomechanical issues (Galloway and Burbey 2011).

Land subsidence prediction is chiefly based on two coupled models that simultaneously examine groundwater flow and consolidation (Gambolati and Freeze 1973), requiring the development of advanced simulation software (Reddish and Whittaker 2012; Guzy and Malinowska 2020). COMPAC used an FDM method for pioneering the modeling of 1D consolidation in compacting aquifer systems (Helm 1986) considering vertical stresses in aquitards. This software was the first to allow simulation of recoverable and non-recoverable consolidations (Helm 1976). The IBS1 tool, combined with MODFLOW for 3D regional groundwater flow, simulated subsidence in 'interbeds' layers (Prudic 1989), which are the compressible layers between high permeable aquifers. Despite the unrealistic assumption of an instant aquifer head propagation in the compressible and low permeability layers, hydrogeologists have used IBS1 extensively (Mahmoudpour et al. 2016). For thick aquitard layers, this IBS1 assumption becomes highly unrealistic. The SUB Package proposed with MODFLOW enabled to simulate time-dependent decrease in pressure propagation and compaction in thick, low-permeability units (Hoffmann et al. 2003). Earlier codes used also an approach with a single equivalent layer rather than distinct ones, preventing from offering individual subsidence results for each layer (Jafari et al. 2016; Choopani et al. 2019). The SUB-WT package for MODFLOW offers the possibility of a total stress variation (Leake and Galloway 2007; Leake and Galloway 2010). However, in most of these groundwater-dependent geomechanical models, constant elastic and inelastic compressibility coefficients are assumed constant, which does not fit with the reality (Dassargues 1996) as the compressibility is dependent on the reached effective stress influenced by the induced groundwater drawdown (Guzy and Malinowska 2020). Beyond these mentioned codes, specific advanced modeling solutions were also developed by different research teams for a detailed and reliable simulation of land subsidence (Brinkgreve and Vermeer 1999; Calderhead et al. 2011; Hu et al. 2013; Pham et al. 2019; 2020). For example, among the first ones, Dassargues et al. (1993) developed a 3D FEM model for simulating transient groundwater pressure conditions in the area of Shanghai. This model was coupled to 30 vertical 1D flow-compaction geomechanical FEM models where pore pressure conditions on the boundaries of the aquifer layers were actualized at each time step from the 3D model. Specifically, this approach allowed to have a very fine discretization of the clay layers. This also allowed to take the hydraulic conductivity and specific storage variations (in function of the stress-state) into account (Dassargues 1995).

More recently, the implementation of Artificial Intelligence (AI) and Machine Learning (ML) in geomechanical modeling is evolving, bringing improved simulation efficiency and predictive capabilities (Baghbani et al. 2022; Zhang et al. 2023). In subsidence prediction and mapping, various AI methodologies have been adopted, including Artificial Neural Networks (ANN) (Zhao and Chen 2011; Yang and Xia 2013; Rafiee et al. 2022), Adaptive Neuro-Fuzzy Inference Systems (ANFIS) (Jang 1993; Park et al. 2012; Faryabi 2023), and Support Vector Machines (SVM) (Lee et al. 2018; Mehrnoor et al. 2023; Rajabi et al. 2023). Additionally, various other methodologies, such as adaptive neuro-fuzzy inference system–genetic algorithm (ANFIS–GA) (Wen et al. 2022), Random Forest (RF) (Ebrahimy et al. 2020), and Bayesian Logistic Regression (BLR) (Tien Bui et al. 2018), have found applications in mapping susceptibility to land subsidence (Eghrari et al. 2023). However, despite their potential, AI and ML are not without limitations. Since these models are largely data-driven, but not physically- or process-based, they rely on the quality and quantity of available data (Bejani and Ghatee 2021). Without sufficient or reliable data, AI and ML models may produce skewed or over-fitted results (Ray 2019). Hence, the traditional understanding and interpretability provided by classic groundwater flow coupled to geomechanical models remain essential.

The understanding of land subsidence has deepened immensely, from basic observations to advanced computational and predictive models. Initially attributed to only natural processes, significant human-induced contributors, especially groundwater extraction, have been identified, explained, and simulated in recent times (Liu et al. 2024; Wang et al. 2024). The advancements, favored by computational innovations, have been very useful in forecasting, understanding, and managing subsidence, especially in regions vulnerable to multiple subsidence drivers. Yet, challenges persist, especially in defining detailed geological layers properties and their behavior under varied pore pressure and thus effective stress conditions.

3.4. Challenges in Measurements & Data

3.4.1. Data Overview

3.4.1.1. Land Subsidence Measurements

Land surface deformation can be measured and mapped using different geodetic techniques (Galloway et l. 1999; Galloway and Burbey 2011). Among the traditional methods of displacement assessment, differential leveling can be accurate and cost-effective for local scale surveys. However, establishing high-quality observations from first-order precision in leveling is time-consuming, labor-intensive, and overpriced on a regional scale (Qin et al. 2018). Extensometers are used to measure displacements in deeper strata, allowing to determine the compaction of individual consolidating layers. They offer crucial data on the deformation rate and magnitude (Gabrysch and Coplin 1990; Galloway and Burbey 2011).

Differential Light Detection And Ranging (Dif-LiDAR) is another method for displacement monitoring at the local-scale. LiDAR data is costly due to its high-resolution hardware requirements, demanding direct physical access to the target area, complex data processing for converting point clouds into meaningful 3D models, and dealing with large data volumes (Challis et al. 2008; Liu 2008). LiDAR estimates typically have standard deviations in the order of 5 cm or less (Streutker and Glenn 2006), making them less suitable for regions with millimeter deformations (Zheng et al. 2022). The Global Navigation Satellite System (GNSS) offers high temporal resolution observations and determines an absolute position by harnessing signals from at least four Earth-orbiting satellites. This allows for millimeter-level precision in a three-dimensional plane (Langley et al. 2017; Hu et al. 2019; Del Soldato et al. 2021). However, at a regional scale, GNSS surveys are limited by their point-based measurements and thus limited large-scale coverage. The use of GNSS campaigns also comes with significant workloads, elevated costs, and the difficulty of maintaining observation sites over extended durations (Hongdong et al. 2011).

These drawbacks are addressed by PS-InSAR techniques, which also mitigate the limitations of the conventional InSAR method (Ferretti 2000; 2001; 2007; Fiorentini et al. 202). Yet, even with PS-InSAR, the deformation pattern might not be accurately delineated if the spatial density of the Persistent Scatterers (PS) is lacking (Dehghani et al. 2013). Moreover, highly localized displacement assessments are constrained by the spatial resolution of C-band SAR data sets, which can reduce the ability to detect and map smaller-scale deformations (Khan et al. 2022). On the contrary, high-resolution SAR imagery from X-band satellites can provide tremendous data points covering an area with sufficient data control on the ground to precisely map land subsidence phenomena, but the drawback is the cost and the availability of the X-band SAR images on a specific target area. Concerning the example located in Belgium as mentioned previously, the The Belgian GNSS network includes 33 permanent GNSS reference stations corresponding to the Flemish RTK-network (FLEPOS) along with the WALCORS (Walloon Region) and GPSBru (Brussels Region) (Deruyter et al. 2022). Of these 33 stations, overall displacement between 2001–2015 was assessed using two LiDAR campaigns over Flanders (Werbrouck et al. 2011; Meylemans 2017). However, achieving a sub-centimeter confidence interval remains challenging for the detection of the Antwerp subsidence with the order of a few millimeters a year. BEZA is situated in Antwerp harbour, while ANTW and ATWR are located in the suburban area close to the Antwerp city center (Figure 3.4a) (Digitaal Vlaanderen 2023).

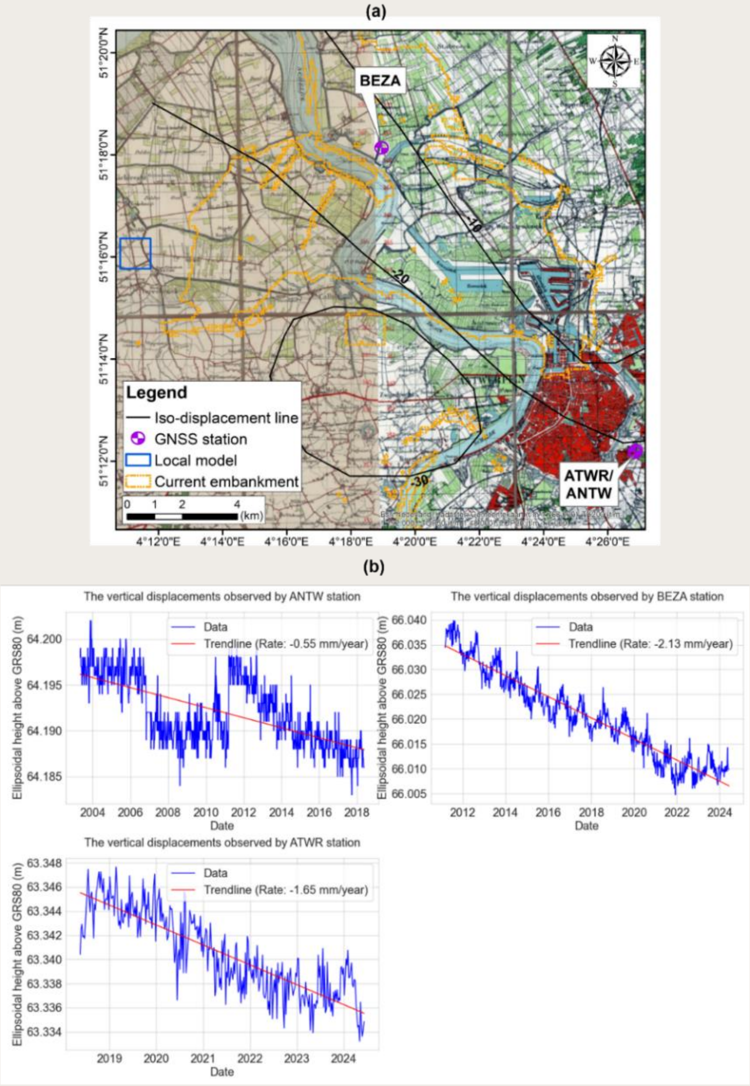

Figure 3.4 a Isolines of the cumulative deformations (in mm) from leveling surveys conducted by Pissart and Lambot (1989) during the period 1946–1980, overlaid on a historical map of the Antwerp region from 1946 (Esri Netherlands 2015), GNSS stations, referenced inside the Flemish FLEPOS network (Digitaal Vlaanderen 2023), are highlighted; **b** time series showing measured vertical deformation at these GNSS points.

These stations were deployed in 2003 (ANTW), 2010 (BEZA), and 2018 (ATWR, replacing the previous ANTW station). These stations have monitored surface elevation and have shown an average velocity of -0.55, -2.13-, and -1.65±0.49 mm/year over the periods of 2003–2018, 2010–present, and 2018–present respectively (Figure 3.4b). Historically, a classical national leveling was conducted twice in Belgium: first from 1946–1948, and again from 1976–1980 (Pissart and Lambot 1989). The most pronounced displacement measured between 1946–1980 is illustrated by the isoline of -20 mm, which passes through the Antwerp harbour (Figure 3.4a).

The most recent deformation measurements in Antwerp were obtained using the Stanford Method for PSs (StaMPS) time series analysis software (Hooper et al. 2007; Hooper 2008). StaMPS integrates the principles of PS-InSAR into its methodology. The spatial variability and temporal evolution of displacement in the region were determined using data from the ERS (1992–2001) (Figure 3.5a), Envisat (2003–2010) (Figure 3.5b), and Sentinel-1A (2016–2020) satellites (Declercq et al. 2021). For this research, the Sentinel-1A data was extended to cover up to 2023 (Figure 3.5c). Additionally, TerraSAR-X data from 2019–2022, processed using the SARPROZ software (Perissin et al. 2011), were also used to complement the analysis. For this study, only the time series of deformation from TerraSAR-X data during 2019-2022 was used to compare with the results of deformation from the geomechanical model. Annual average velocity map along LOS from TerraSAR-X data are not depicted in Figure 3.5 and will be detailed in a separate study.

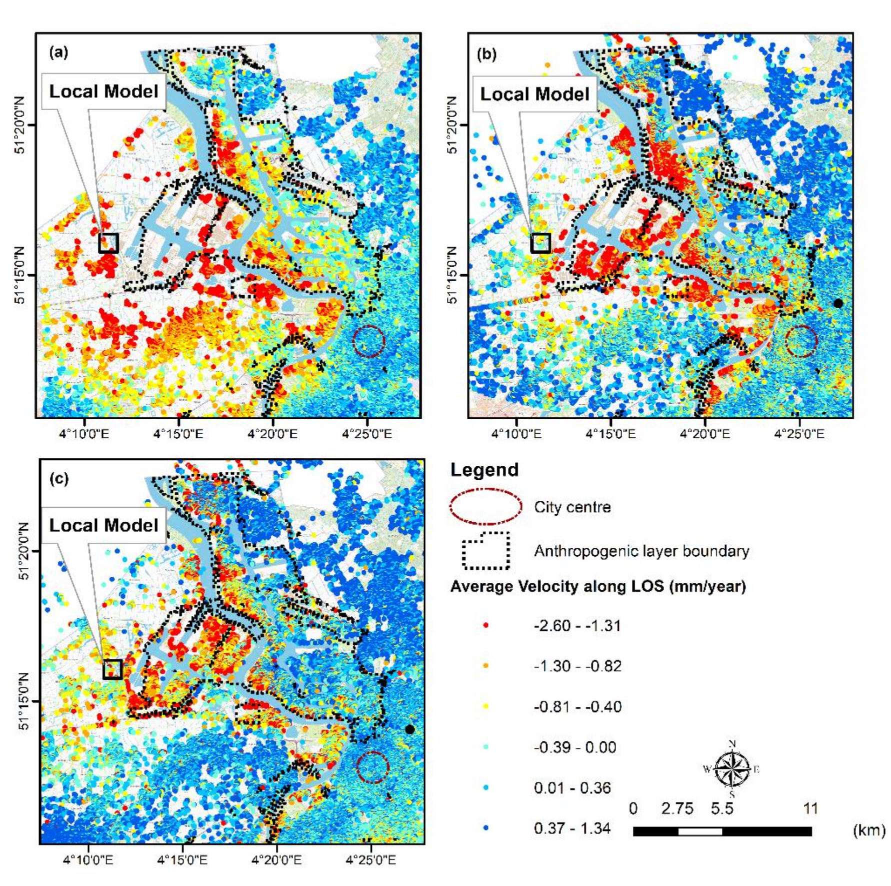

Figure 3.5 Annual average velocity map along LOS observed by: **a** ERS (1992–2001); **b** ENVISAT (2003–2010) data from (Declercq et al. 2021); and **c** Sentinel (2016-2023) radar data. The location of the reference point in the Envisat and Sentinel processing is shown with the black circle in b and c.

For each satellite operational duration, an InSAR time-series data stack for Antwerp was processed to offer a reliable displacement time series spanning 1992–2023. In the central region of the Antwerp harbour, measurements integrated over specific periods provided estimations of land subsidence. For the intervals 1992–2001, 2003–2010, and 2016–2023, the highest estimated average subsidence located approximately in the middle of the harbour was -4.4 mm, -4.1 mm, and -7.4 mm +/- 0.49 mm, respectively along LOS. The highest rate is reported to focus on the areas experiencing the most significant deformation over each mission. In Figure 3.6, the time series of these points are illustrated. The key parameters presented in the figure include the R-squared (R^2) value indicating the goodness of fit for the linear regression model, the standard error, the standard deviation and the p-value of the time series. The p-value is provided to demonstrate the statistical significance of the trend, with lower values indicating a stronger confidence in the observed subsidence pattern. Together, these parameters help to evaluate the reliability and robustness of the subsidence estimates for each period.

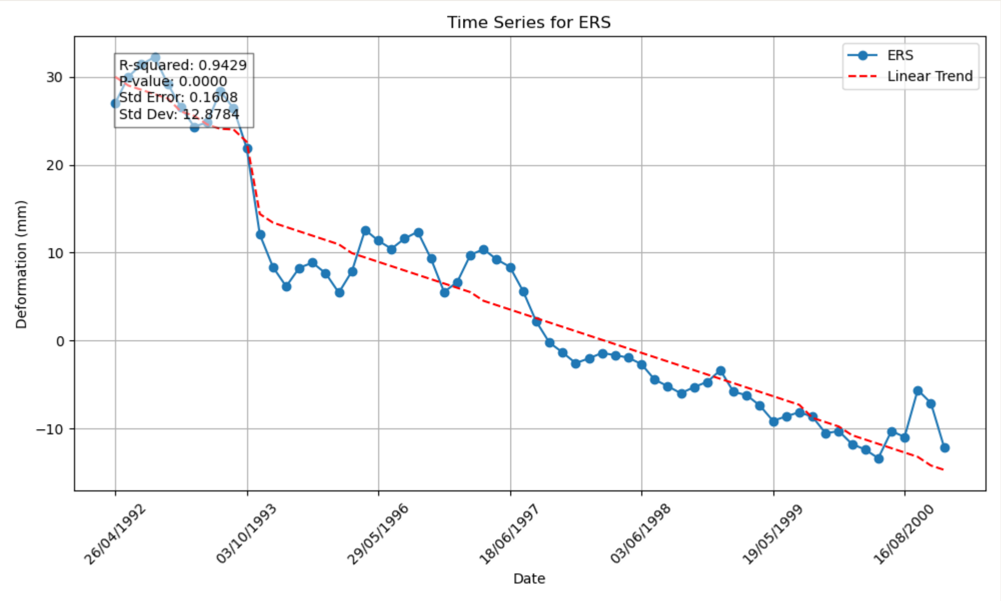

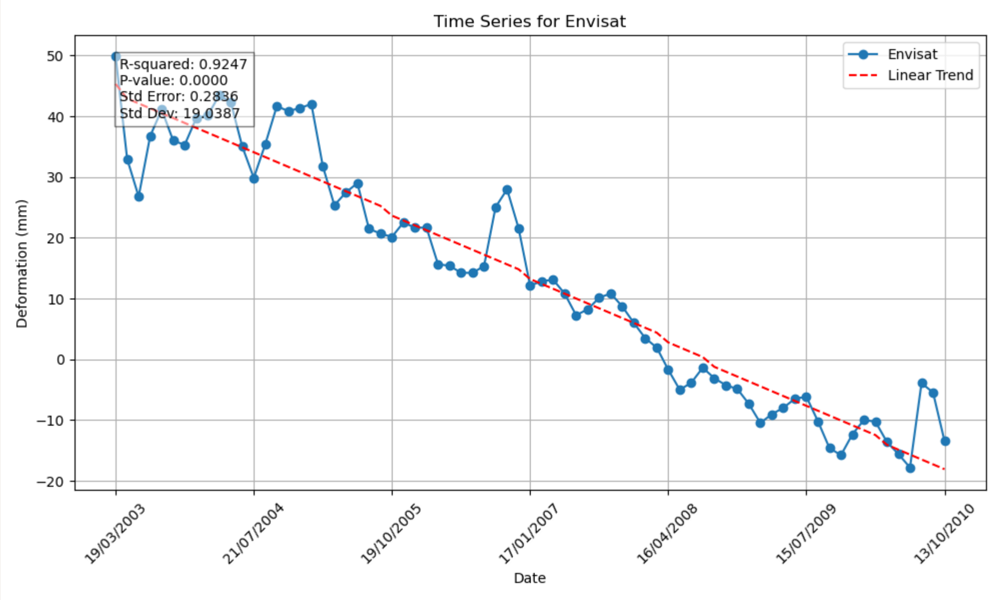

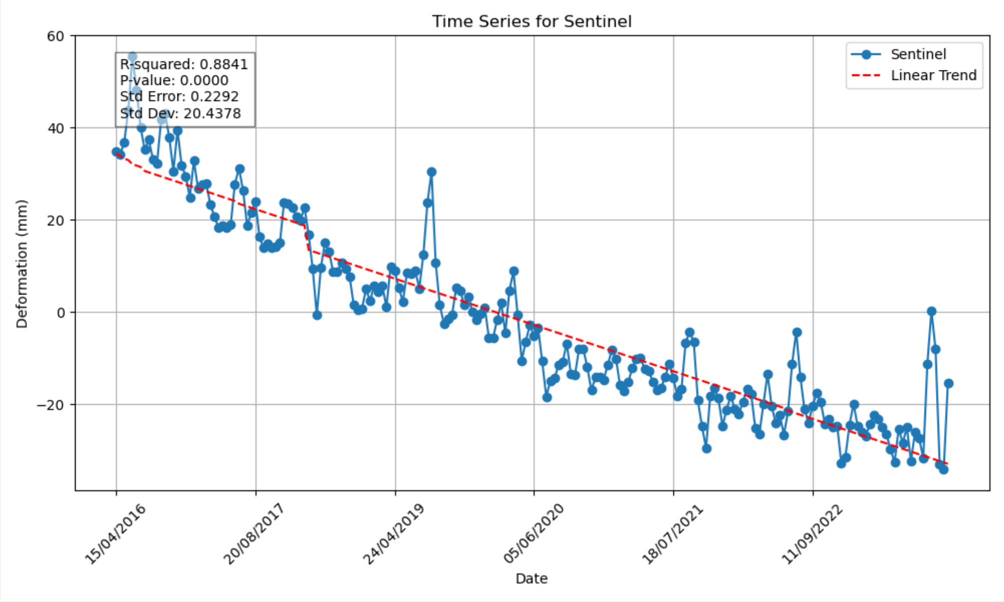

Figure 3.6 Time series of the PS points with the highest subsidence rates in the middle of the Antwerp harbour for the periods 1992–2001, 2003–2010, and 2016–2023.

The displacement rates and their associated uncertainties are well-supported by statistical parameters. The R^2 values for the ERS (0.94), Envisat (0.92), and Sentinel (0.88) data indicate that the linear models fit the time-series data with high accuracy, capturing between 88% and 94% of the variance. The small p-values (0.0 for all missions) further confirm that the observed trends are statistically significant, implying that the linear model is a valid representation of subsidence over time. For the ERS data, the standard error (SE) of the estimated subsidence rate was 0.16 mm/year, for Envisat it was 0.23 mm/year, and for Sentinel, the SE was 0.22 mm/year. These values reflect the uncertainty in the linear trend estimation and indicate that the subsidence rates reported for each mission are reasonably precise within their respective confidence intervals. The standard deviation values (12.87 mm for ERS, 19.03 mm for Envisat, and 20.43 mm for Sentinel) are a combination of the noise in the observations and the non-linear component of the displacement mechanism. This indicates that while the linear model captures the overall trend well, subsidence behavior may exhibit short-term variations within each dataset.

The city center of Antwerp, situated on the eastern bank of the Scheldt River, exhibited relative stability with average displacement rates of 0.2 mm/year during 1992–2001, -0.1 mm/year during 2003–2010, and 0.2 mm/year during 2016–2023. These reported values are relative to a reference point in the PS-InSAR processing framework. The reference point is critical for calculating relative displacements, as PS-InSAR measures the change in distance between a satellite and the Earth’s surface, rather than absolute motion. For each time-series stack, displacements are measured with respect to the unique reference point, whose absolute motion cannot be known, only postulated. The ERS data were processed over a broader region that extends beyond the Antwerp area (Declercq et al. 2021), and the reference point used for this analysis is located at 4.54° E, 50.93° N. This reference point is not within the Antwerp region but is positioned roughly at the centroid of the triangle formed by the cities of Leuven, Mechelen, and Brussels. For the Sentinel and Envisat stacks, the reference point was chosen on the eastern side of Antwerp city, outside the city's ring. For the Sentinel and Envisat stacks, the reference point was chosen on the eastern side of Antwerp city, outside the city's ring (Figure 3.5. b and c). Geologically, this location was selected due to the sedimentary layers beneath that region, which consist of aeolian sands and silts from the late Pleistocene (Gent Formation). These sediments are significantly old and consolidated. The consolidation of these layers over thousands of years supports the assumption that this area is currently relatively stable, making it a reasonable choice as the reference point. Yet, this choice is necessarily 'assumptions-based', and may (i) not be correct (e.g. due to deep dynamic processes or due to autonomous motion of the scatterers), and (ii) not be identical between different sensors and time-series. The consequence is that reported absolute displacement rates (or changes in absolute displacement rates between sensors) of less than, say, 0.8 mm/y, need to be considered as not significant, and that geophysical interpretation of such small rates should be avoided. Additionally, the reference point was averaged from a cluster of values within a 30-meter radius of the point indicated in Figures 3.5, b, and c, ensuring a robust reference point. Since the noise of the reference PSs propagates to the time series of each PS point, interpretation of the time series becomes more reliable when a reference point is chosen with limited scattering noise, i.e., the most coherent PSs (Van Leijen 2014). This is the second reason that the reference point is chosen in the reason that many human-made structures act as high-coherence PSs. The TerraSAR-X data also used the same reference point as Envisat and Sentinel, though its results are not shown here as they will be discussed in a separate study.

The reference point plays a crucial role in InSAR time-series analysis, as all displacement measurements are calculated relative to it. If the reference point in the one stack were moving downward by 0.5 mm/year while we assume it is stable (0.0 mm/year), this would introduce a systematic error in the displacement measurements. Specifically, all measurements would indicate less subsidence than what is actually occurring by 0.5 mm/year. In other words, the displacement values across the study area would be underestimated by that amount. This could lead to an incorrect interpretation of the deformation patterns, especially over long time periods, where the cumulative error becomes more significant. The approach to mitigate potential systematic errors introduced by the reference point in displacement measurements is discussed in Chapter 5.

In the case of the Antwerp subsidence, which is mainly driven by the compaction of sediments beneath the harbour and potentially due to groundwater extraction, horizontal displacement components are generally expected to be minimal. This is because compaction processes tend to cause predominantly vertical subsidence as the ground compresses under its own weight or due to external stressors such as reduced pore pressure from groundwater pumping. In such cases, the sediment layers typically settle vertically rather than moving laterally. Moreover, the geological structure in the study area does not indicate any significant tectonic or lateral movement that would result in noticeable horizontal deformation. Therefore, the horizontal displacement components can be reasonably neglected in this context.

In summary, various methods have captured the Antwerp land subsidence patterns over the years. To explain the causes of such displacements, the subsequent section will explore hydrogeological data.

3.4.1.2. Hydrogeological Data

For groundwater modeling, accurate information regarding the geometry and the hydrogeological properties of the different layers is needed. The simulation of groundwater flow and consolidation processes necessitates values for the key parameters such as the horizontal hydraulic conductivity (K_h), the vertical hydraulic conductivity (K_v), and the specific storage (S_S) of each layer. Data about the source/sink of groundwater, such as groundwater extraction rates and recharge, also play an important role. The hydrogeological characteristics of aquifers and aquitards can be assessed using various techniques, this falls outside the scope of this paper. In situ measurements such as pumping, and recovery tests data are usually available only in aquifers. For aquitards, lab-scale measured data based on permeameter and oedometer tests are only exceptionally available. As a result, first-guessed values for those parameters are often based on estimations gathered from the literature (Dassargues 2018) on the basis of the identified lithologies. The main problem is however that a large uncertainty usually remains for these values of parameters that is only partially solved by calibration of the model on measured data. The reliability of the calibration depends then strongly on the availability of historically measured potentiometric heads in each aquifer and in different locations.

In the study conducted in Antwerp, we were facing significant challenges related to data scarcity. For several layers, hydraulic conductivity parameters are derived either from direct measurements or from prior calibrations documented in other studies, as detailed in Table 3.1 (Gedeon et al. 2007). Most hydraulic conductivity values were inferred from grain size distribution analysis, occasionally supplemented by pump or slug tests. Two potentiometric maps were available in Antwerp: one for the Miocene aquifer (2011) (Layer 2) and another for the Oligocene aquifer (2009) (Layers 4 and 6) (Vandersteen et al. 2012; Vlaamse Milieumaatschappij 2016). As the deeper aquifers are characterized by a high salt content, they are less exploited than the shallow layers, which offer reserves of high-quality groundwater (Vandersteen et al. 2012).

Table 3.1 Values of vertical and horizontal hydraulic conductivity in different layers used for the Antwerp local model, derived from various sources including the Central Campine model (Verbeiren et al. 2006), Brulandkrijt model (Ministerie van de Vlaamse Gemeenschap 2004), and direct measurements (Vandersteen et al., 2012).

Layer	$K_h (m/s)$[a]	$K_v (m/s)$	K_h and K_v source
1	1.5×10^{-5}	3.0×10^{-6}	Central Campine model
2	6.5×10^{-5}	1.3×10^{-6}	Central Campine model
3	3.8×10^{-9}	1.7×10^{-10}	Brulandkrijt model and Central Campine model
4	2.7×10^{-5}	6.7×10^{-6}	Brulandkrijt model
5	1.8×10^{-10}	5.4×10^{-11}	measured
6	2.3×10^{-6}	2.3×10^{-8}	Brulandkrijt model
7	1.2×10^{-11}	1.2×10^{-13}	Brulandkrijt model
8	4.1×10^{-5}	1.0×10^{-5}	Brulandkrijt model
9	1.2×10^{-9}	1.2×10^{-11}	Brulandkrijt model

[a] For model layers that combined two zones with similar lithology, a geometric mean of their values was calculated to obtain a single representative value for each unified layer. Furthermore, where the literature provided two calibrated values from different models for the same layer, we also calculated their geometric mean. In cases where a range of values was provided, geometric means of these ranges were determined.

In the broader Antwerp region, the Miocene aquifer system experiences thus significant pumping activity. However, this aquifer was not being exploited locally within the area of our local model. On the contrary, within the Oligocene aquifer, a centrally located pumping well with an extraction rate of 2,800 m^3/year is taken into account within the Oligocene aquifer. The layer corresponds to layer 6 (Lower Oligocene Sandy Aquifer) of our model (Figure 3.3). Given the limited availability of data on groundwater levels and fluxes, calibration of the model and optimization of the parameters were considered inappropriate within the scope of this research.

3.4.1.3. Geomechanical Data

The consolidation process leading to land subsidence is inherently linked to a decrease in pore pressure. The specific storage coefficient (Ss) acts as the primary coupling parameter, closely linked to the volumic compressibility of the saturated porous medium (Dassargues 2018). The oedometer test represents common one-dimensional vertical consolidation lab tests in drained conditions. The results of oedometer tests are used for compressibility assessment (Yong and Townsend 1986).

The compressibility value is dependent on the effective stress state, and thus, on the current pore pressure. Furthermore, the change of compressibility values is dependent on whether the current effective stress is higher or lower than the pre-consolidation effective stress (σ'_{max}), which is the maximum effective stress previously endured (Dassargues 1998). For each layer, the pre-consolidation effective stress influences thus the further geomechanical A ‘compression constant’ (C) and a ‘swelling constant’ (A) can be defined for describing the effective stress-strain relationship. These last are defined in a linearized ($\ln \sigma'$, relative deformation) diagram, which shows the presumed elasto-plastic geomechanical behaviour. The 'swelling constant' (A) illustrates the reversible elastic behaviour (below the pre-consolidation effective stress), whereas the 'compression constant' (C) describes the non-reversible plastic behaviour (above the pre-consolidation effective stress) (Figure 3.7a).

Similarly, in a linearized ($\log \sigma'$, void ratio e) diagram, a compression index (C_C) and a swelling index are depicted (C_S) (Figure 3.7b). Oedometer tests allow to determine those characteristics as cited in various studies (Lambe 1951; Jorgensen1980; Yoon et al. 2011; Dassargues 2018).

Considering the intrinsic connection between the specific storage coefficient and compressibility values, groundwater literature often distinguishes the elastic and inelastic (plastic) geomechanical behaviours via elastic and inelastic specific storage coefficients (S_{ske} and S_{skv}) (Zhuang et al. 2017; Li et al. 2022).

In the local model, our assessment of geotechnical parameters was based on thorough reviews of geotechnical reports and studies. For the shallow layers, tested samples from four boreholes, located near the eastern boundary of the local model (Geotechnics Department in Flanders 1999) were analyzed to derive the C and A constants. For the deeper low-permeability layers, comprehensive geomechanical studies conducted in the region (i.e. Kallo, Mol, and Essen), together with hydrogeological reports, have provided C_C and C_S index values (Deng et al. 2011; Nguyen et al. 2014). For the sandy aquifers corresponding to layers 4, 6, and 8 (Figure 3.3), the same geomechanical parameters were used than those of the sandy layer 2, a shallow layer for which we had direct borehole data. This decision was based on similarities in lithology between them, even though both their depths and thicknesses differed significantly. We also considered the same parameters for layer 5, a deep clay aquitard, as we did for Boom Clay (layer 3). For layers 7 and 9, corresponding to the deep clay aquitards, characteristics similar to those of the Ieperiaan clay (Nguyen et al. 2014) were chosen.

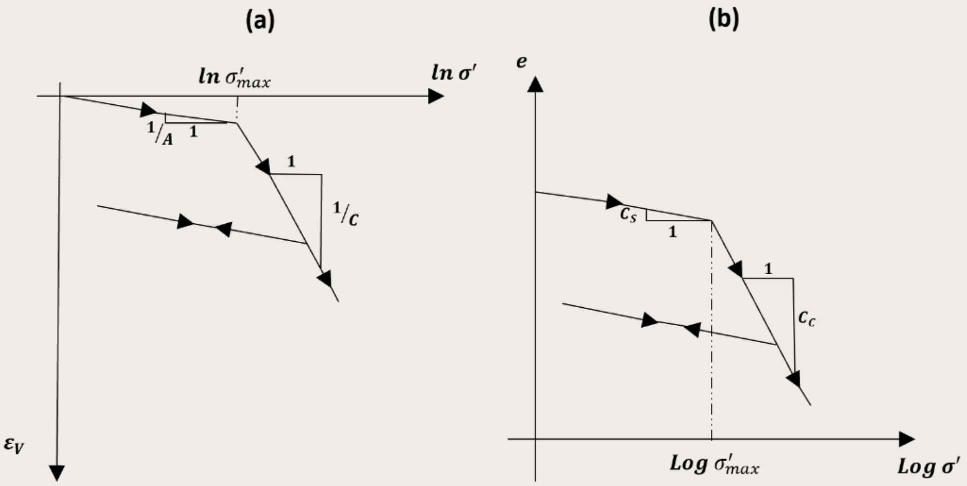

Figure 3.7 Schematic representation of oedometeric results in different axis systems: **a** diagram of relative deformation (ε_V) in function of the natural logarithm of effective stress $(\ln \sigma')$; **b** diagram of void ratio (e) in function of the logarithm of effective stress $(\log \sigma')$ (modified from Dassargues (2018))

Using the oedometer test results, we calculated the elastic (S_{ske}) and inelastic skeletal specific storage (S_{skv}) coefficients introduced in the 1D-geomechanical model (Hoffmann 2003). To drive these coefficients, we started by calculating the compressibility (α). When geomechanical parameters (A, C) were available, the compressibility was determined using the formula (Dassargues 2018):

$$\begin{cases} \alpha = \frac{1}{A.\sigma'} & \sigma' < \sigma'_{max} \\ \alpha = \frac{1}{C.\sigma'} & \sigma' \geq \sigma'_{max} \end{cases} \quad (35)$$

where σ' is effective stress, and σ'_{max} is pre-consolidation effective stress. In cases where the geomechanical parameters (C_C, C_S) were provided the compressibility was calculated using the relationship (Jorgensen 1980):

$$\begin{cases} \alpha = 0.434 \times \frac{C_S}{\sigma'} & \sigma' < \sigma'_{max} \\ \alpha = 0.434 \times \frac{C_C}{\sigma'} & \sigma' \geq \sigma'_{max} \end{cases} \quad (36)$$

Once the compressibility values (α) were obtained, the specific storage coefficients can be directly written in relation to volume compressibility (Pa^{-1}) [M^{-1}LT^{2}] (Dassargues 2018):

$$S_S = \rho g \alpha \quad (36)$$

where ρ is the density of water and g is the acceleration due to gravity. Finally, to obtain the elastic and inelastic skeletal specific storage coefficients for the geomechanical model, the specific storage values were multiplied by the thickness of each layer (b) (Hoffmann et al. 2003):

$$\begin{cases} S_{ske} = S_{S\,(elastic)} \times b & \sigma' < \sigma'_{max} \\ S_{skv} = S_{S\,(inelastic)} \times b & \sigma' \geq \sigma'_{max} \end{cases} \quad (38)$$

These parameters, which are fundamental for deformation simulation in each layer, are detailed in Table 3.2, including sources for the (A, C) and (C_S, C_C) values with appropriate references. Further, the pre-consolidation effective stress $(\sigma'_{max})$for the uppermost layer was assumed based on the current potentiometric head at the initial date of simulation, representing a normally consolidated state. This implies that the uppermost layer behaves inelastically as it adjusts to changes in stress.

Table 3.2 Elastic and inelastic skeletal storage coefficients for each model layer. These values are calculated from oedometer test results conducted on samples from four boreholes on the eastern boundary of the local model (Geotechnics Department in Flanders 1999), Essen and Mol (Deng et al. 2011), and Kallo (Nguyen et al. 2014)

Layer	S_{ske}(-)	S_{skv}(-)	A and C source location	C_S and C_C source location
1	3.0×10^{-3}	2.3×10^{-2}	Eastern boundary boreholes	-
2	3.5×10^{-3}	2.1×10^{-2}	Eastern boundary boreholes	-
3	3.5×10^{-2}	8.0×10^{-2}	-	Essen and Mol
4	9.2×10^{-4}	5.3×10^{-3}	Derived from similar lithology (see Layer 2)	-
5	2.3×10^{-3}	5.1×10^{-3}	-	Derived from similar lithology (see Layer 3)
6	8.3×10^{-4}	4.8×10^{-3}	Derived from similar lithology (see Layer 2)	-
7	1.5×10^{-2}	4.4×10^{-2}	-	Similar to Ypresian clay [a] in Kallo
8	1.1×10^{-3}	6.3×10^{-3}	Derived from similar lithology (see Layer 2)	-
9	2.7×10^{-3}	8.1×10^{-3}	-	Derived from similar lithology (see Layer 7)

[a] For Layer 7, data sourced from Ypresian clay samples in Kallo is used due to its lithological similarity and comparable depth characteristics, although it is not directly part of the modeled layers

For the deeper, over-consolidated layers, the pre-consolidation effective stress is considered as the equivalent to the potentiometric head of 50 meters below the current head in each layer. This reflects sedimentary paleo loading and unloading events, implying an over-consolidation state. Consequently, these deeper layers exhibit elastic behavior when the effective stress is below this historical maximum and inelastic behavior when it exceeds this threshold.

In summary, geotechnical data from diverse sources with inherent assumptions were adopted. Indeed, uncertainties on these values are large due to data limitations and lithological variability. Table 3.2 lists the values for both elastic and inelastic skeletal storage coefficients across the layers of the model considered for the geomechanical computations. They are our best approximations based on existing data and limitations.

3.4.2. Impact of Data Scarcity on Modeling

The challenges arising by data scarcity significantly influenced the groundwater modeling process in our study. Accurate prescription of boundary conditions was particularly problematic due to limited piezometric data. Specifically, prescribed heads were implemented on the lateral boundaries of the main aquifers (layers 1, 2, 4, 6, and 8), while no-flow conditions were assigned to the bottom, top, and lateral boundaries of the aquitard layers. The scarcity of piezometric data on the border of the local model posed significant challenges for prescribing boundary conditions. A limited number of piezometers were available near the model borders, and all the aquifers considered in the model were not surveyed. Therefore, to prescribe boundary conditions, we projected transient water level values from the nearest piezometers outside the region onto the model borders, using the gradient of the only two available piezometric maps. Another significant issue was the lack of data on solicitation, as only one pumping well is recorded in the region, which might not represent the full extent of groundwater extraction activities. This introduces uncertainties in our understanding of local groundwater dynamics. Additionally, the scarcity of hydrogeological and geomechanical parameter data, as discussed in previous sections, further compounded the uncertainty in our model. The temporal data gaps also posed a challenge. The study used PS-InSAR data from different temporal series: ERS (1992–2001), Envisat (2003–2010), TerraSAR-X (2019–2022) and Sentinel-1A (2016–2023). Groundwater level data were available only for the period from 2007 to 2016. Given these data constraints, we decided to run our model simulation from 2007 to 2023. The initial period (2007–2009) was characterized by unstable model conditions due to the model starting from an equilibrium state, requiring time to stabilize. Therefore, only the results from 2009–2023 are considered reliable.

Between 2010 and 2016, the lack of PS-InSAR data prevented continuous comparisons of deformation data. After 2016, the absence of piezometric data meant the model had to rely on solicitation data from a single recorded pumping well, which was insignificant and might not fully capture the extent of groundwater extraction activities. This limitation affects the reliability of the simulation results for the 2016–2023 period. These data limitations highlight the challenges in achieving accurate and reliable subsidence modeling and in comprehensively comparing these results with PS-InSAR estimations.

3.5. Simulated Delayed Deformation

In most numerical models, the water pressure variation is assumed linear within one finite element or one finite difference cell. This induces an unrealistic approximation of the pore pressure in the aquitard compressible layers if they are modelled by one layer of cells or elements. For obtaining a better approximation of the vertical distribution of the pore pressure, the compressible layers must be discretized with finer sublayers. Thus, using MODFLOW, the discretization of Main Layers (MLs) into finer Sub-Layers (SLs) enhances the accuracy of simulations, even if these SLs are given the same hydrogeological and geomechanical parameters. A finer vertical resolution allows a more detailed representation of water pressure and thus distribution within each layer. This is particularly critical for thick, low-permeability layers, which are more susceptible to delayed consolidation due to slower pore-water pressure dissipation in the low-permeability and compressible layers. By subdividing layers (i.e., in our case layer 2 into four, layer 3 into eight, layer 5 into four, layer 7 into eight, and layer 9 into four) finer vertical resolution was achieved (Figure 3.8). The increased number of SLs introduces a time-stepping aspect to the mechanical behavior of the model, thereby enabling the simulation to approximate the delay in deformation that is observed in hydrogeological materials exhibiting elastic or inelastic characteristics. Through this discretized layering, the model can more accurately simulate deformation over time in each SL and eventually each ML of the local model.

MODFLOW simulations were conducted to model fluid flow and water head dynamics across these adjusted SLs. The simulation spanned from 2007–2023, providing temporal evolution of the hydraulic head which is used as input for deformation calculations. Hydrogeological and geomechanical parameters were maintained across the SLs, with values corresponding to their original ML.

From the pore pressure (and thus the effective stress) calculated at each time step and in each sublayer, a 1D vertical geomechanical model is used to simulate the deformations. Our custom script calculates incremental deformation (Δb) at each time step, for each sublayer, using the following equations:

$$\begin{cases} \Delta b = S_{skv} \times \Delta h & h < h_{min} \\ \Delta b = S_{ske} \times \Delta h & h \geq h_{min} \end{cases} \quad (39)$$

In Equation (37), S_{skv} and S_{ske} are the inelastic and elastic skeletal specific storage coefficients of each SL, respectively, h is the hydraulic head at a given timestep at the center of each cell and h_{min} is the preconsolidation head corresponding to the maximum preconsolidation stress. The script compares h and h_{min} at each timestep and determines the type of deformation: the initial h_{min} for sublayer 1 was set to the initial head at the start of the simulation and for the other layers, an overconsolidation corresponding to a head of 50 meters below the initial head is considered, leading to only elastic deformation.

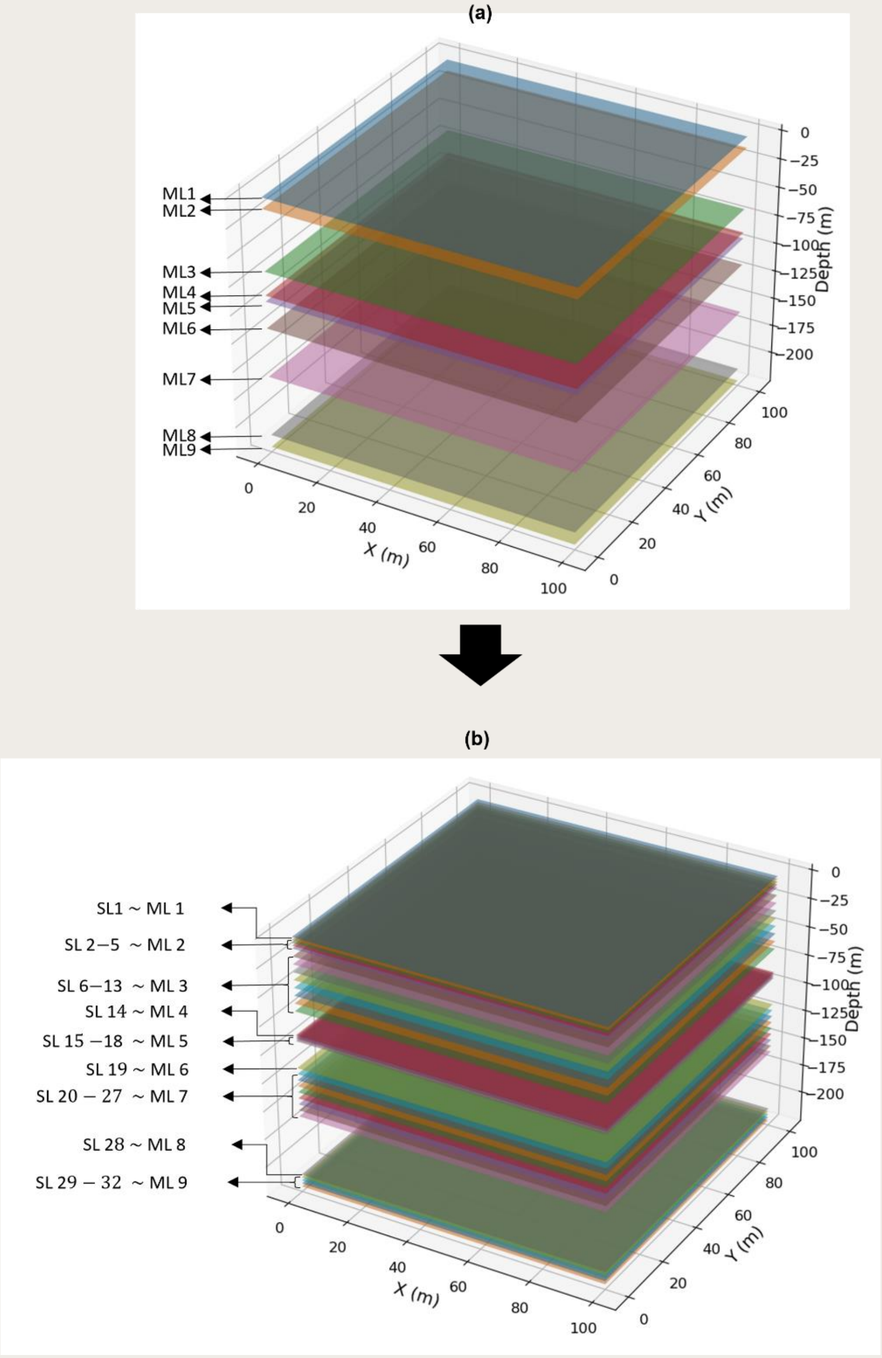

Figure 3.8 3D visualization of the hydrogeological model **a** with only the Main Layers (MLs); **b** with the finer discretization in Sub Layers (SLs)

3.6. Results

We used a 3D groundwater flow with the hydrogeological setup of our study area, which is situated on the southwestern border of Antwerp, specifically outside the harbor backfill. Piezometric heads were monitored from 2007–2016 using observations from three piezometric monitoring wells. At the lateral boundaries of the aquifer layers, hydraulic head values were prescribed, while for the low permeability remaining boundaries a no-flow condition was considered. Hydrogeological parameters were gathered from past studies conducted in this part of Flanders and each layer was considered as homogeneous. A regular grid was used in the XY plane, consisting of 110 by 110 cells, each with an area of 10 meters by 10 meters. In the Z axis, cell dimensions varied based on the thickness of each SL.

3.6.1. Water Head Evolution in Different Sublayers

To address the delayed responses in deformation, the 9 Main Layers (ML) were subdivided into 32 Sublayers (SL).

The evolution between 2007 and 2023 of the water head across SLs corresponding to each ML is illustrated through nine subplots (Figure 3.9). The uppermost SL (ML 1), composed of a mix of sand and clay, shows water head fluctuations similar to those observed in ML 2, which includes four SLs classified as an aquifer. This similarity is attributed to the applied identical boundary conditions for both MLs. This assumption was made due to the lack of direct piezometric data for ML 1, assuming that the hydrogeological influences are comparable to those affecting the adjacent aquifer. Main Layer 3, as a low-permeability aquitard, reveals stability of the water heads in time across its sublayers (SL 6-13), isolating the overlying aquifer (ML 2) from deeper hydrogeological influences. The base of ML 3 (SL 13) exhibits a minor but consistent decline in water head, decreasing at a rate of -0.03 m/year. This subtle change is attributed to the hydraulic gradient induced by lower prescribed heads in the adjacent ML 4. ML 4 is a dynamic sandy aquifer experiencing the highest change, showing a water head drop at a rate of -0.23 m/year linked to groundwater extractions or natural drainage processes within the aquifer. The ML 5 is an aquitard. The influence of the dynamic aquifer above begins to be moderated as evidenced by the decreasing water head declines from the uppermost SL 15 at -0.17 m/year to deeper SLs, which show reductions to -0.09 m/year and -0.06 m/year respectively. The computed water head decline in SL 18 to -0.08 m/year, reversing the previous downward trend, suggests an influence from the aquifer conditions of ML 6 below. In ML 6, the rate of decline in the water head is -0.11 m/year, showing less variation than in the aquifer ML 4. In the aquitard ML 7 water heads are stable in time across the SLs. The water head increases from higher elevation SLs to lower ones (from SL 20 to SL 27) due to the head gradient between the adjacent aquifers ML 6 and ML 8. The aquifer ML 6, exhibits a decline in water head (-0.11 m/year), creating less downward pressure, while the aquifer ML 8, with a rising water head (+0.13 m/year), exerts more upward pressure on the lower sublayers of the aquitard ML 7. The rising water head in ML 8 is likely due to the cessation of pumping wells that were active in the past, allowing for the recovery of the water heads. ML 9 (SL 29 to 32) as the base of the model is classified as a low permeability aquitard. The slight increase in water head (+0.02 m/year) observed in the uppermost SL 29 is attributed to the influence of the aquifers ML 8 above, which imposes an increasing head. In contrast, the deeper SLs (SLs 30 to 32) show almost no change due to their depth and the aquitard properties.

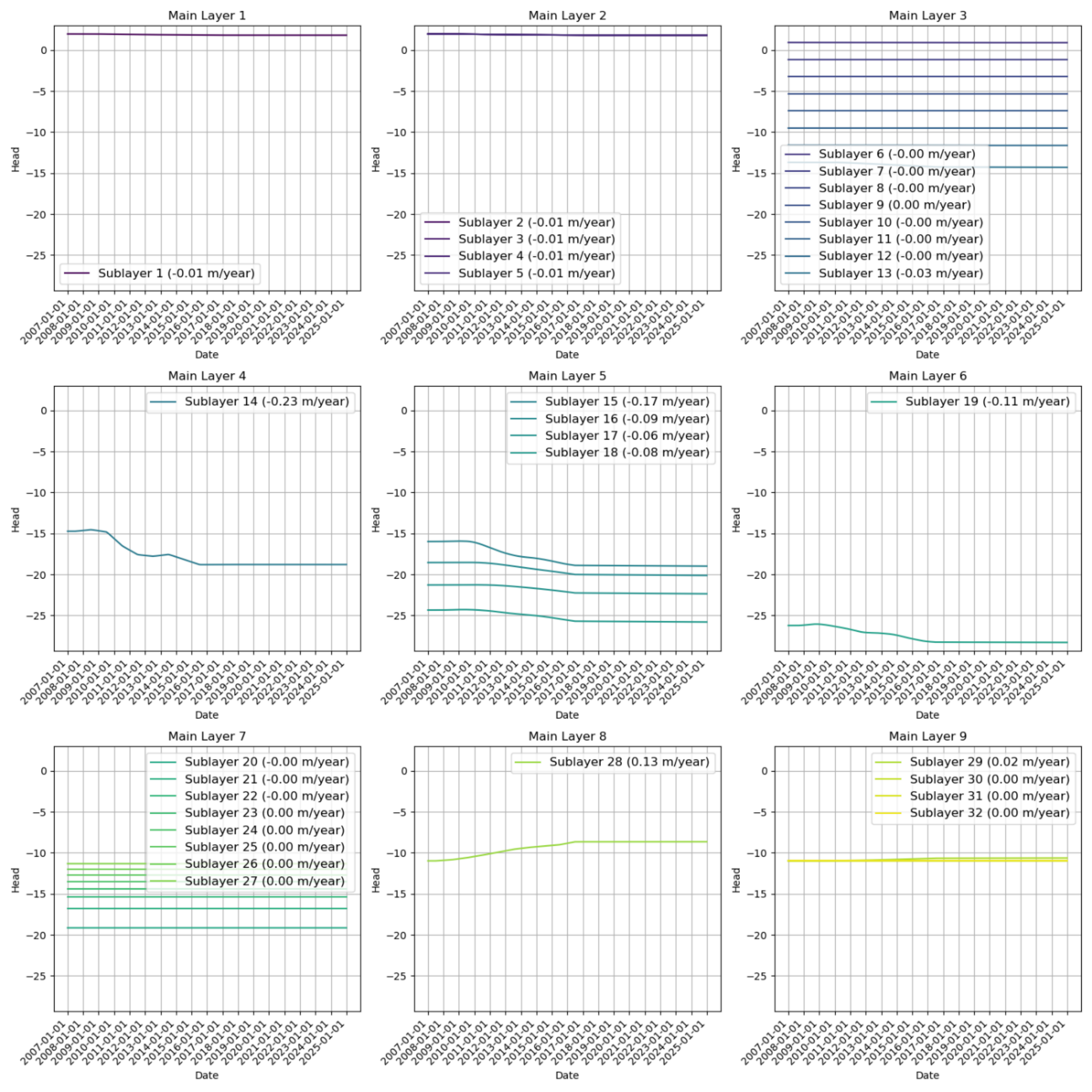

Figure 3.9 Temporal evolution of water head across different sublayers of 3D-flow transient simulation, spanning 2007-2023. The rates of change for each layer are indicated in meters per year (m/year)

3.6.2. Pore Pressure Distribution Across Model Layers

Figure 3.10. illustrates the distribution of pore pressure in the function of depth in one vertical column in the center of the local model. Logically the graph shows the pore pressure increases with depth. In ML 1, 2, 3, and 7, pore pressure profiles remain stable over time. The last SL of ML 3 shows evolving lower water pressures with time, reflecting its interaction with the aquifer pressures in ML 4. ML 5, an aquitard, similarly exhibits evolving lower pressures indicating the significant pressure changes driven by lower water heads in the aquifer ML6. This is due to its position between ML 4 and ML 6, both aquifers, creating a strong hydraulic gradient. In contrast, ML 8 shows a slight increase in pore pressure over time, indicating rising water heads. Stable and consistent pore pressures are computed in ML 9, with nearly no variation over time.

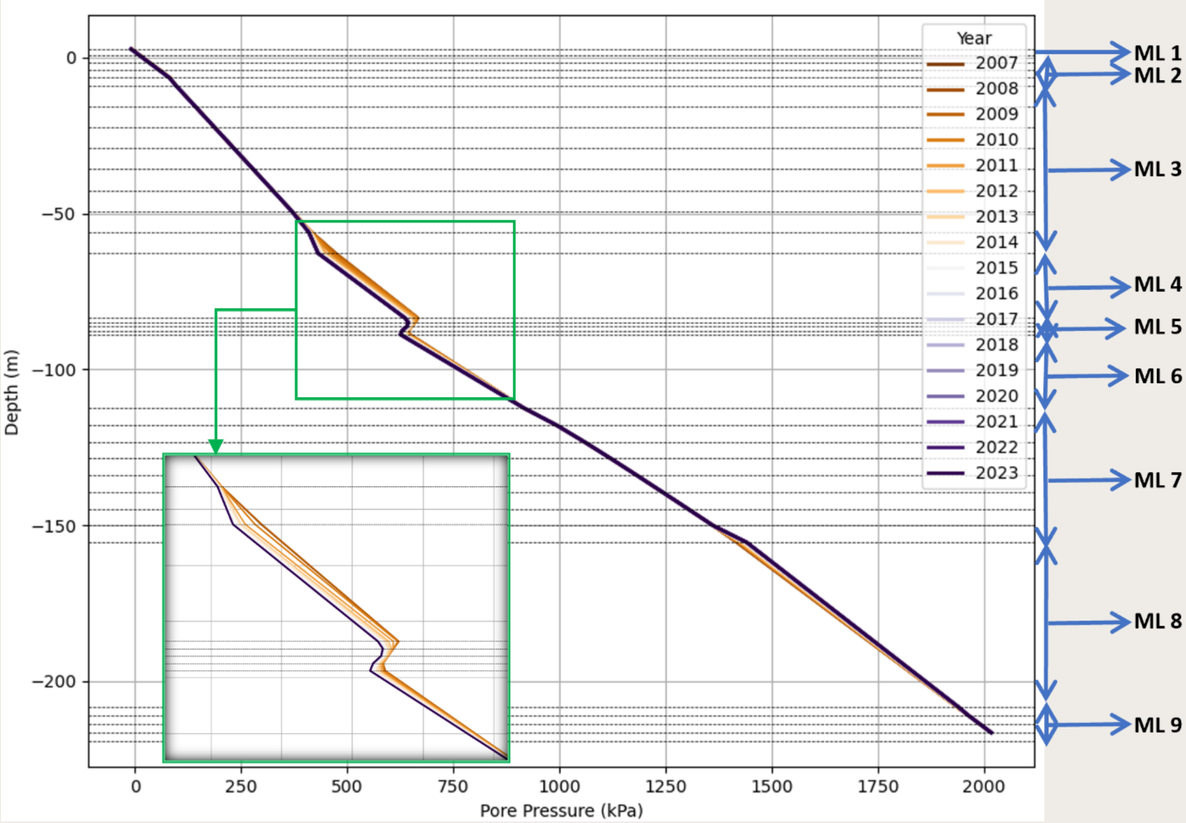

Figure 3.10 Temporal evolution of water head across different sublayers of 3D-flow transient simulation, spanning 2007-2023. The rates of change for each layer are indicated in meters per year (m/year).

3.6.3. Computed Deformation Across Model Layers

The variations in deformation are linked to the characteristics and water head fluctuations within each main layer (ML) and sublayers (SL). Figure 3.11 presents the deformation time series computed across the SLs within each ML during the simulation period.

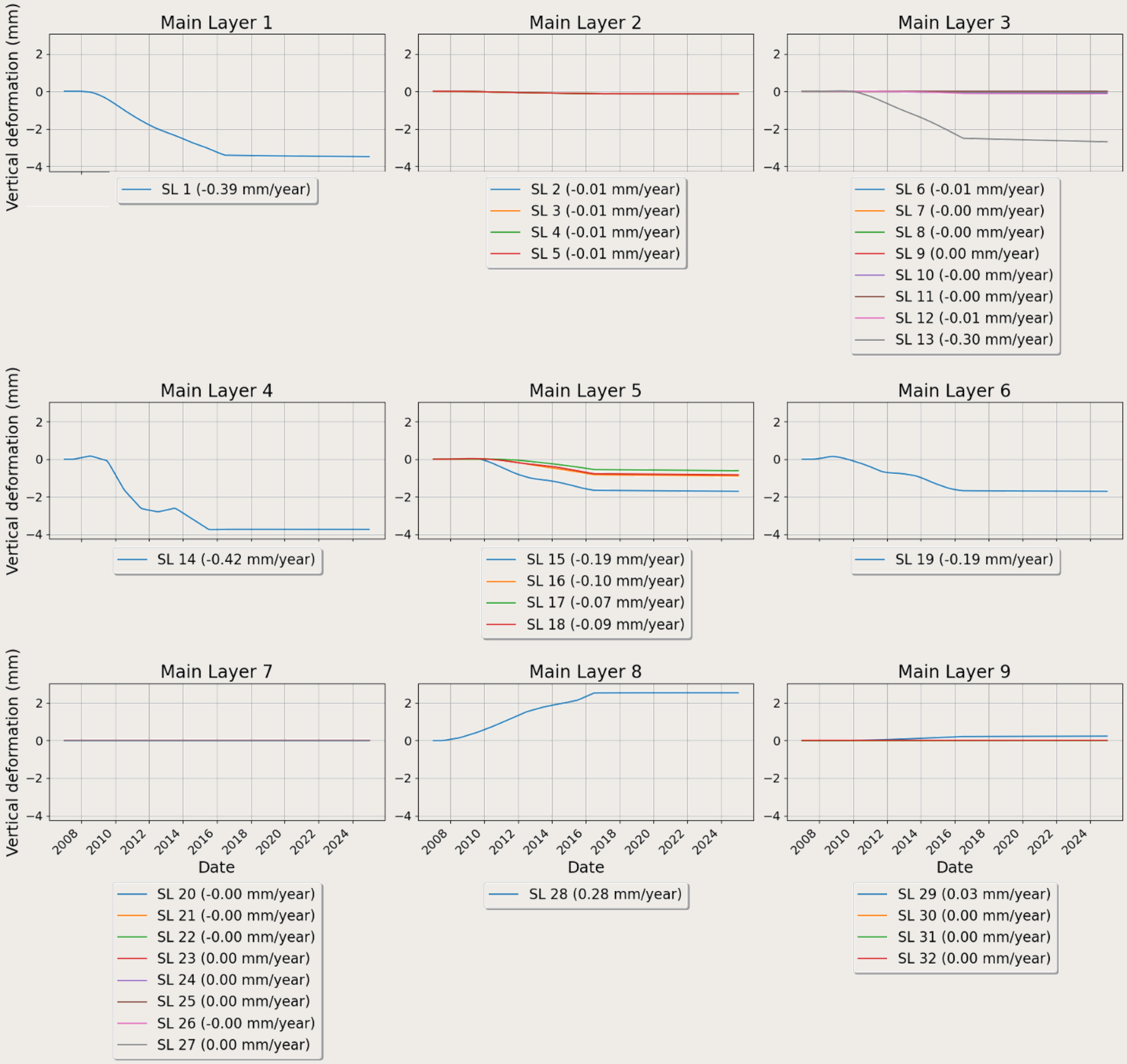

Figure 3.11 Temporal evolution of deformation (in mm/year) across different sublayers of the 1D-geomechanical model, during the 2007-2023 period.

In ML 1, the deformation rate of -0.39 mm/year is significantly high compared to other layers, despite only slight water head variation. This shows the effect of the inelastic storage coefficient that is higher than the elastic storage coefficient.

In contrast, each SL of ML 2 shows negligible elastic deformation of -0.01 mm/year despite a similar water head variation as in ML 1. In ML 2 and deeper, deformation is only elastic. ML 3 exhibits minimal deformation across its sublayers (SL 6-13) except for the sublayer closest to ML 4 (SL 13). Very low deformation rates in the SLs of ML 3 are consistent with their stable water head in time. In the deeper part of ML 3 (SL 13) a slight deformation is computed at a rate of -0.3 mm/year, induced by the lower heads in ML 4. Although this rate of displacement is minimal, the Boom clay in this layer has a high compressibility and low permeability, making it highly sensitive to even small changes in water pressure. This means that a very negligible water pressure drop can result in significant deformation, leading to a total displacement of up to 2 mm over the period 2007–2016. ML 4 shows the highest rate of deformation, with a deformation rate of -0.42 mm/year, which corresponds to the significant rate of water head decline. This aquifer is primarily composed of sand with shells and glauconite, explaining its compaction. In ML 5, deformation rates decrease with depth: the uppermost SLs (SL 15) exhibit a rate of -0.19 mm/year, reducing to -0.10 mm/year in the middle of ML 5, and further to -0.07 mm/year in the deeper SL. The deformation rate of -0.09 mm/year in SL 18 illustrates the effects of the influence of aquifer ML 6 below. ML 6 shows a moderate deformation rate of -0.11 mm/year, as the water head is declining. ML 7, another aquitard, shows no deformation across SLs 20-27 due to stable water heads in time, preventing experiencing deformation. In ML 8, rising water heads at a rate of +0.13 m/year lead to swelling of +0.28 mm/year rather than compaction. Finally, ML 9 at the base of the model shows minimal deformation due to the stable water head in time. While SL 29 shows a slight swelling of 0.03 mm/year, influenced by the upward pressure from the upper ML 8, this deformation is too small to be significant. Overall, negligible deformation is computed in ML 9.

3.6.4. Comparison Between 1D Geomechanical Results with PS-InSAR Estimations

Figure 3.12 shows the comparison between computed vertical deformation values from the 1D geomechanical model coupled to the 3D groundwater model (specifically plotted for the central cell of the model) and deformation values Projected onto the Vertical (PoV) direction estimated by PS-InSAR across different periods. The PS-InSAR data, extracted from four PS-InSAR data processed in this study, SkyGeo, and EGMS, represents the average time series of PS points located within the limits of the local model area, rather than single PS points. This averaging approach ensures a more reliable and representative comparison by mitigating the effects of local anomalies and measurement noise that could affect individual PS points but doesn't correct for the differences in the reference frame.

The PS-InSAR estimations are relative time series of the displacements. It is important to note that the results from the various missions, processing procedures, and providers use different reference points, i.e., different reference frames, as discussed earlier. Only if all these reference points can be guaranteed to be identical and/or stable, the results can be considered unbiased, comparable, and geophysically interpretable. If a reference point is assumed to be stable but is moving, this would result in an under- or overestimation of displacement across the entire region relative to that point. Such a guarantee of having identical and/or stable reference points for all the products cannot be given. Consequently, different numerical values for the different products cannot be unambiguously interpreted from a (geo)physical perspective.

Only for visualization purposes, the initial values of the Envisat, Sentinel, and TerraSAR-X timeseries were aligned with the ERS trendline. However, it is important to recognize the limitations of this approach. First, the projected displacement onto the vertical differs for each dataset due to variations in satellite viewing geometries. This means that aligning trendlines does not account for the different ways in which deformation is observed by each satellite potentially leading to misinterpretation of the compared deformation data. Additionally, the reference points for each dataset are not the same. Since each reference point plays a key role in calculating relative displacements, assuming equivalence across missions can introduce biases, particularly if the stability of the reference points varies. Lastly, deformation rates in the Antwerp region change over time due to factors like groundwater extraction and sediment compaction. Aligning trendlines implies a consistent subsidence trend across different missions, but this assumption overlooks the evolving nature of subsidence. The ERS trendline represents historical data and should not be assumed to continue unchanged in later periods observed by other missions. Thus, while this alignment allows for easier visual comparison, it does not accurately reflect the distinct deformation behaviors across different periods and mission

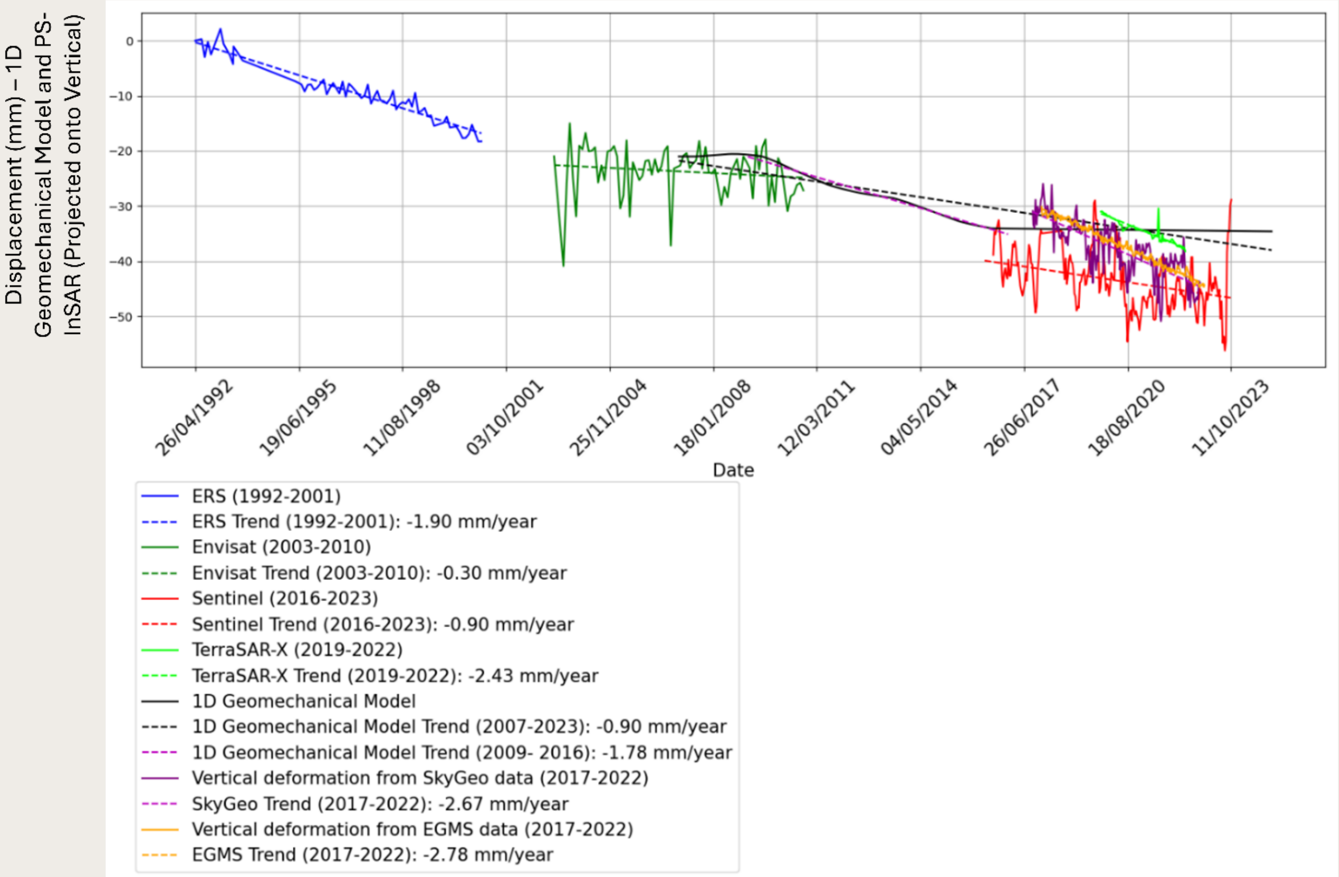

Figure 3.12 *Comparison between PS-InSAR estimations of displacement values projected onto the vertical direction from different datasets, and simulated deformation from the 1D geomechanical model coupled to the groundwater model. Note that the different products each refer to a different reference frame, as they choose a different reference point (or point set). Therefore, the observed differences cannot be unambiguously attributed to (changes in) geophysical processes.*

InSAR inherently measures 3D deformation projected onto LOS. Thus, it is important to address the potential horizontal component of deformation when interpreting InSAR results. For the case of Antwerp, the horizontal deformation is not expected to be significant enough to impact the overall interpretation of subsidence patterns. To justify this there are two different perspectives. From an InSAR perspective, the data are sensitive to displacements along the LOS, but the sensitivity of LOS displacement to vertical components is typically higher than that to horizontal components (north-south and east-west). This is because the radar signal is more aligned with vertical movements, while horizontal sensitivity, particularly in the north-south direction, is reduced due to the satellite's flight geometry. Specifically, the smaller heading angle between the satellite flight path and the north direction diminishes InSAR's ability to detect north-south deformation (Ren and Feng 2020). Moreover, the horizontal component of the displacement would cause variations in LOS displacement between ascending and descending passes, as the satellite's look direction changes. In this study, however, no significant difference between the LOS displacements in ascending and descending passes was observed, which indicates minimal horizontal movement in the region. Based on results from SkyGeo, for a set of random PS points in the middle of Antwerp harbour with a high rate of deformation during the Sentinel (2017–2022) period, the region shows minimal variation between ascending and descending LOS displacements, as illustrated in Figure 3.13. The average velocity of deformation from the descending pass is -8.12 mm/year, while the ascending pass shows -7.52 mm/year. This small difference in velocity between the two passes suggests that horizontal movement is minimal in this area. If significant horizontal deformation were present, we would expect larger discrepancies between the ascending and descending observations, as the horizontal component would contribute differently to the LOS displacements in each pass due to the varying satellite look directions.

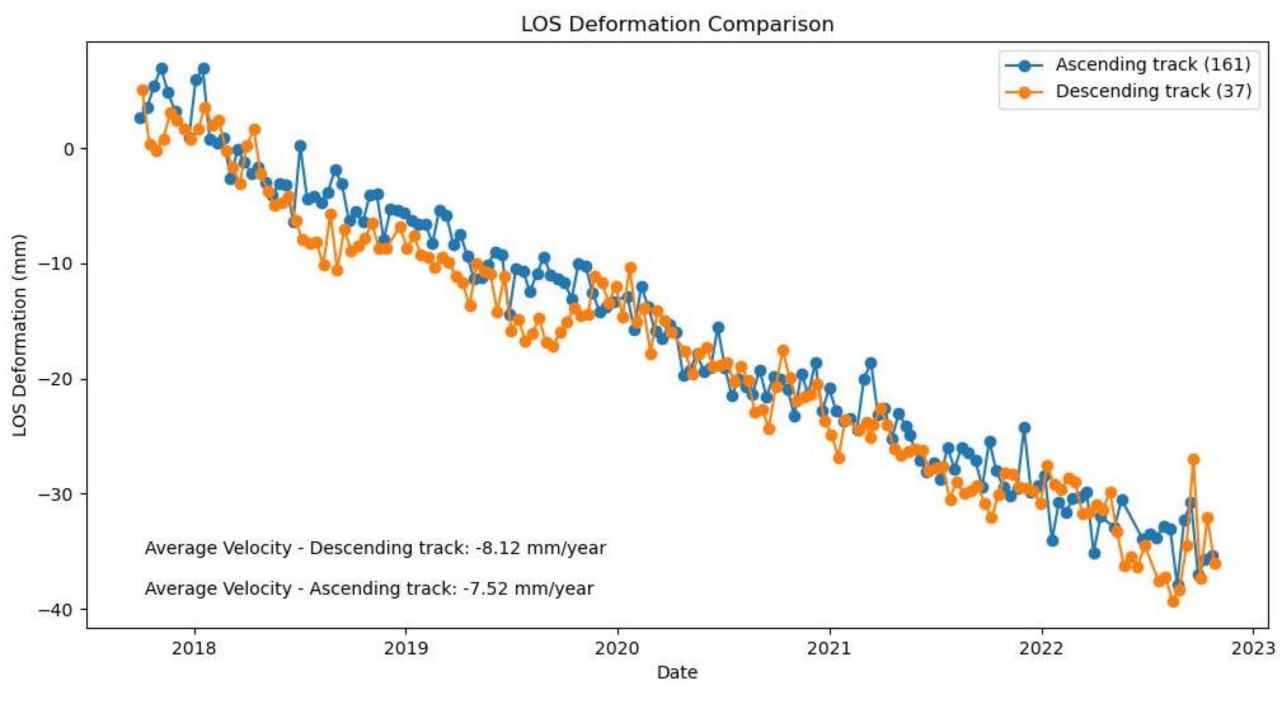

Figure 3.13 Comparison of LOS displacements between ascending and descending passes for a set of PS points located in the middle of the harbour (2017–2022). The difference of 0.6 mm/y is not considered to be significant (i.e., based on ascending and descending reference frame differences, different physical scatterers, and precision of the estimated rates). This suggests that the displacement can be considered to be pure vertical

From a hydrogeological and geological perspective, the primary cause of subsidence in Antwerp, particularly in the harbor area, is attributed to the consolidation of soft Holocene sediments and potentially, groundwater extraction. These processes typically lead to vertical compaction of the sediments due to the loss of pore water, which in turn results in subsidence. While horizontal movement are always expected with subsidence patterns due to driving mechanisms at depth, their contribution scales with the subsidence gradient, and is often less than 10-15% of the vertical component. The consolidation of clayey and silty layers due to effective stress increases following groundwater withdrawal further supports the idea that the subsidence is predominantly vertical. Horizontal forces, which would lead to significant lateral movement, are typically absent in this context. Without significant tectonic activity, lateral spreading, or horizontal strain, the deformation will be dominantly vertical. Despite the unclear trends of PS-InSAR estimations during data gaps, this provides a practical solution for visualization and allows for simultaneous comparison of deformation rates across the datasets. Computed deformations in model were also shifted vertically to allow the comparison. PS-InSAR data provides deformation estimations along the LOS of the satellite, which was projected onto the vertical direction for comparison purposes.

While the ERS data offers historical insight into subsidence from 1992–2000, showing a trend of -1.9 mm/year, it does not overlap with the deformation phase simulated in the geomechanical model (i.e., post-2007) limiting long-term comparisons. Similarly, the Envisat data, spanning from 2003–2010, only has three years in common with the modeled time series and shows a rate of -0.3 mm/year, which falls within the noise level. The early stage of the model, from 2007–2009, is not considered reliable as the model is too much dependent on initial conditions during the first years of the simulation. Later, we lack PS-InSAR data from 2010–2016. Post-2016, both the model and PS-InSAR provide time series, but the model results are based only on quite uncertain water pressure induced by a single pumping well with a nearly insignificant discharge rate, rather than on head values from measured piezometric data, which were, unfortunately, not anymore available during this recent period. All these data issues affect the comparison reliability and interpretation. Concerning PS-InSAR data processing, the Sentinel data periods are not entirely aligned: our processing through ISCE-STAMPS covers 2016-2023 (green), while SkyGeo and EGMS data span 2017-2022 (purple and orange, respectively). The Sentinel data which serves as the input for both SkyGeo and EGMS are the same. However, the final InSAR information products generated by these providers differ due to variations in processing techniques, such as noise filtering, threshold settings, reference point selection and other choices. Both products exhibit low noise and clear deformation rates, complementing the results from our processing. Additionally, our processing of TerraSAR-X data through SARPROZ for 2019–2022 shows a rate of -2.43 mm/year similar to those estimated by SkyGeo and EGMS.

From 2009 to 2016, the 1D geomechanical model shows a rate of -1.78 mm/year, which falls between the vertical deformation rates observed from PS-InSAR estimations (excluding the non-reliable 2007–2009), closely matching the SkyGeo which shows slightly higher rate of -2.67 mm/year and similar to EGMS data from the same period showing -2.78 mm/year. Later from 2016 to 2023, deformations computed by the model are probably underestimated as these results are based on incomplete recorded pumping data (as mentioned previously). The TerraSAR-X data processed in this study, covering 2019–2022, shows a deformation rate of -2.43 mm/year, which aligns closely with the estimates from SkyGeo and EGMS. The Sentinel data processed through ISCE-STAMPS shows a lower rate of -0.90 mm/year during 2016–2023. These variations can be attributed to differences in processing techniques, regional factors, and the inherent limitations of InSAR as an estimation method.

3.6.5. Sensitivity Analysis of 1D Geomechanical Model

To evaluate the sensitivity of the 1D geomechanical model to changes in specific storage parameters, we considered ten different scenarios with an increase of 100% for the inelastic specific storage in ML 1 and the elastic specific storage in the rest of the MLs. Computed deformations from the 1D geomechanical model under these different scenarios compared to the reference scenario are shown in Figure 3.14. Scenario 10 represents the combined effect of a 100% increase in specific storage across all model layers, providing the overall system sensitivity. The sensitivity analysis indicates that a 100% increase in specific storage of each layer results in varying impacts on computed deformations. For instance, the cumulative deformation at the end of the period for scenario 5, is -17.6 mm, compared to -13.6 mm in the reference scenario. Results show that ML 4 is the most sensitive layer to changes in specific storage values, where a 100% change in the parameter results in a 27% change in cumulative deformation. For scenario 1 (inelastic specific storage increased by 100% in ML 1), an additional deformation mean rate of 0.44 mm/year during 2009–2016 is computed with respect to the reference scenario. In the case of ML 8, where water heads are rising, a 100% increase in elastic specific storage results in a 23% decrease in cumulative deformation compared to the reference scenario. This represents the highest swelling from the reference scenario.

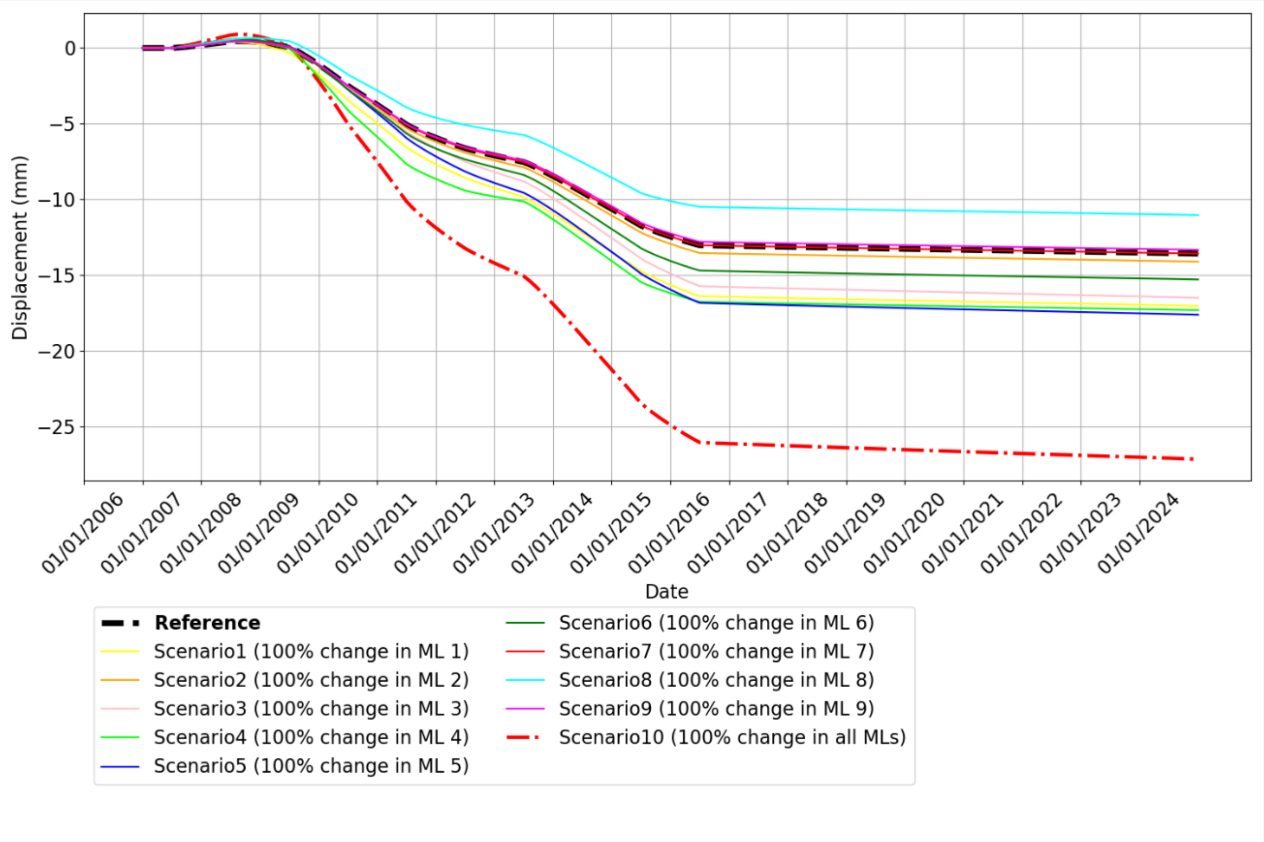

Figure 3.14 Comparison of deformations from the 1D geomechanical model under different scenarios, showing the sensitivity to a 100% increase of the inelastic (scenario 1) and elastic (scenarios 2-9) specific storage parameters, and the combined effect (scenario 10).

On the other hand, MLs 2, 7, and 9 showed the least sensitivity, with an identical cumulative deformation as with the reference scenario. This is because there is nearly no pressure change over the simulated period in these layers meaning their exact values are less critical and can vary without greatly affecting the model results. For scenario 10, with a 100% increase in specific storage across all layers simultaneously, the cumulative deformation was significantly different from the reference scenario, indicating the cumulative impact of changes in all layer's specific storage on the total deformation. If the parameters were chosen incorrectly, even a 100% increase in specific storage (which is a modest change in geotechnical terms) would result in a 100% increase in deformation. This highlights the importance of carefully selecting the parameters, as even modest changes can significantly impact the model results.

3.7. Conclusions

In previous studies, it was concluded that the deformation observed by InSAR in the Antwerp region was significant where backfill is present, mainly within the harbor, and that areas without backfill did not experience substantial deformation. Therefore, subsidence was attributed solely to backfill compaction. This interpretation, however, oversimplified the causes of subsidence in the region. By focusing only on backfill compaction, previous studies neglected other potential factors contributing to the deformation. In this study, we demonstrated that outside of the backfill areas, groundwater extraction plays a role in subsidence, a factor that was largely overlooked in earlier studies.

This study demonstrates the value of comparison of PS-InSAR estimation projected onto the vertical direction, with vertical deformation calculated by a coupled hydro-geomechanical model to provide a more comprehensive understanding of land subsidence mechanisms. This is illustrated in a case study near Antwerp. We developed a detailed 3D groundwater flow model using MODFLOW and then used a customized code executing a 1D geomechanical model based on the same geomechanical equations as the SUB package of MODFLOW (Hoffmann et al. 2003). By dividing the nine MLs into 32 SLs, we were able to implicitly consider delay effects for the water pressure propagation in the low permeability layers. For our study case, the significant water head declines in the Ruisbroek-Berg Aquifer (ML 4) and the Lower Oligocene Aquifer System (ML 6), lead to notable compaction while the increase in water head in the Wemmel-Lede Aquifer (ML 8) results in swelling. This swelling compensates for a part of the total compaction, leading to less resulting land subsidence. Additionally, relatively stable water heads in time in aquitards resulted in minimal deformation except in ML 5 (Tongeren Aquitard) and its SLs, influenced by the declining water heads in ML 4 and ML 6. In the polder deposits (ML 1) and Pleistocene and Pliocene Aquifer System (ML2), the water heads are only slightly decreasing. However, due to the inelastic deformation in ML 1, slight deformations are computed. No deformation is computed in ML 2 despite experiencing the same negligible water head decline. The period 2007–2009 was not considered in calculating the rate due to the model dependency on initial conditions, which resulted in slight uplift and unreliable results. During 2009–2016, the maximum deformation was simulated, primarily because this period had the most significant changes in water heads. After 2016, due to the lack of measured piezometric data, the model output relied only on pumping data from a single well. This is probably quite incomplete, as it may not account for all groundwater extraction activities of unauthorized pumping in the area resulting in underestimating deformation after 2016.

This study aligned PS-InSAR datasets (ERS, Envisat, TerraSAR-X, and Sentinel) only for comparison purposes of deformation rates over time.

LOS deformation estimations from PS-InSAR were projected to the vertical direction. The ERS data from 1992–2000 indicated a subsidence trend of -1.9 mm/year, though it did not overlap with the post-2007 deformation phase simulated in the geomechanical model. The Envisat data from 2003–2010 showed a rate of -0.3 mm/year within the noise level, with only three years overlapping with the model time series. The early stage of the model (2007–2009) can be considered unreliable due to the influence of initial values, and the lack of PS-InSAR data from 2010–2016 further complicated comparisons. Post-2016, both the model and PS-InSAR data provided time series, but model results were based on incomplete pumping data.

The 1D geomechanical model rate of -1.78 mm/year during 2009–2016 closely matches the SkyGeo, EGMS, and TerraSAR-X rates of -2.67, -2.78, and -2.43 mm/year respectively. Considering that in PS-InSAR, detecting small-scale deformations in the millimeter range is challenging due to several inherent limitations, the deformation rates obtained from the different PS-InSAR datasets of SkyGeo, EGMS, and our Sentinel processing (all Sentinel-based) along with the results of TerraSAR-X are remarkably consistent. This consistency is a significant achievement, considering the various uncertainties and limitations in the PS-InSAR process, especially the challenge of selecting a stable reference point, which can introduce biases if the reference itself is subject to any movement. On the other side, the 1D geomechanical model coupled to the 3D hydrogeological model also carries its own set of uncertainties. The model is sensitive to key geomechanical parameters, and the accuracy of these parameters directly impacts the deformation simulations. Despite these uncertainties, the model produced a deformation rate of -1.78 mm/year for the 2009–2016 period, which is closely aligned with the deformation rates from the PS-InSAR datasets. This convergence between the model simulation and the PS-InSAR estimations demonstrates a high level of agreement between independent approaches, suggesting that both the model and the satellite-based observations are capturing the main mechanisms driving subsidence in the Antwerp local model. This emphasizes the model effectiveness in capturing subsidence mechanisms, though comprehensive data integration is crucial for reliable subsidence assessment. The pore pressure profiles have indicated hydrostatic pressure evolution with depth and time, influencing subsidence, and highlighting differences in response between aquifers and aquitards. The sensitivity analysis has shown that changes in specific storage parameters can significantly impact the model results, particularly for some layers such as layers 4 and 5. Despite uncertainties and assumptions in parameter estimation, the combined use of PS-InSAR data and coupled hydro-geomechanical models provided valuable insights into subsidence mechanisms and driving factors.

A critical finding of this study is the importance of selecting and interpreting the reference point in PS-InSAR processing. In this study, it was assumed that the reference points for all missions (ERS, Envisat, Sentinel, TerraSAR-X, SkyGeo, and EGMS) were stable. Although this assumption is reasonable based on prior knowledge of the physical characteristics of the area, high coherency of the selected point, and geological stability, any slight movement of the reference point could introduce bias into the displacement calculations. For example, if the reference point itself moves vertically, it can lead to under- or overestimation of the subsidence rates. Since it is inherently impossible to ‘detect’ reference point instability from the InSAR data only, this possibility must be considered, particularly in long-term studies. In Chapter 5, we discuss a solution to ensure reference point stability using corner reflectors equipped with GPS, which would allow for independent validation of the reference point position.

Furthermore, potential horizontal deformation was evaluated. Differences of 0.6 mm/y were detected between ascending and descending orbits, which suggests that horizontal movement in Antwerp's subsidence is expected to be less than 1 mm/y. This aligns with the geological context of sediment compaction and groundwater extraction, the introduced causes of vertical subsidence in this region.

Although the focus of this study was on a local area outside the Antwerp harbor, the findings can be extended to help explain the subsidence observed in the harbor itself. The hydrogeological and geomechanical processes modeled in the local area share similarities with the larger Antwerp region. The geology and hydrogeology of both areas are very similar as they share similar lithology, except that Antwerp Harbour contains backfill material, including material excavated from the river, which is not present in the local model area. Additionally, results from the local coupled hydrogeological model to the 1D geomechanical model showed that after 2016, when the model was no longer based on piezometric data (which were unavailable post-2016) and relied only on pumping well data, deformation was likely underestimated. This indicates that there may be more unauthorized pumping in the local model area. Given that the local model is located outside the harbor, it raises the question of how much groundwater pumping, both authorized and unauthorized, may be contributing to subsidence within the Antwerp harbor itself, where industrial activity is significantly higher. This suggests that subsurface processes driven by groundwater extraction are not only active but may be even more pronounced in the harbor region.

Future work could specifically focus on obtaining more detailed geomechanical parameters, and also detailed hydrogeological parameters like hydraulic conductivity and specific storage coefficient. However, acquiring more comprehensive and detailed datasets of stress factors, including actual data on groundwater extraction rates and other transient influences, appears to be crucial. Thus, more extensive and detailed data sets of historical data concerning water pressure changes and pumping changes would significantly enhance the accuracy of subsidence predictions and the overall reliability of the models. A key recommendation is to increase the number of piezometric wells across the entire Antwerp region, particularly in layers most sensitive to water level fluctuations, as these are critical for understanding the full extent of subsidence driven by groundwater extraction. It is recommended to develop the same coupled hydrogeological and geomechanical model, this time for the entire Antwerp region, to accurately estimate the vertical deformation caused by groundwater extraction across the whole area. This would allow us to isolate the share of deformation due to the compaction of backfill from that due to groundwater extraction, providing a clearer understanding of the contributing factors to subsidence in the region. Additionally, there is a need to use the Integrated Geodetic Reference Stations (IGRS) within the region to ensure the stability of a reference point or to accurately measure its velocity if any. The IGRS is a corner reflector that is equipped with a GPS antenna. In other words, it is a collocated benchmark whose movement can be estimated as a single physical structure. This station is already installed in the Antwerp harbor, close to the Doel Nuclear plant, and is investigated in detail in Chapter 5. However, it is recommended that the data from this station needs to be actively used. With this, we are capable of measuring the absolute physical deformation of the reference point. This would allow us to determine whether the reference point is stable or moving, and, if it is moving, to account for this movement in the PS-InSAR analysis. This would significantly enhance the reliability of the PS-InSAR results, allowing them to be more confidently compared with the outputs of the geomechanical model, leading to improved subsidence assessments in the Antwerp area.

4

Land Surface Deformation in Saint-Vaast

This chapter is based on the paper titled, " Assessing Hydrogeological Hazards in the Post-Mining Region in Saint-Vaast, Belgium: Insights from Three Decades of SAR Data and Piezometric Analysis," by A. Choopani, P. Y. Declercq, B. Ronchi, X. Devleeschouwer, which is currently under review at the Journal of Natural Hazards.

4.1. Abstract

This study assesses hydrogeological hazards in the Saint-Vaast region, Belgium, impacted by three decades of deformation post-coal mine closure. Using Persistent Scatterer Interferometric Synthetic Aperture Radar (PS-InSAR) applied to 30 years of Synthetic Aperture Radar (SAR) data along with geological investigations and 13 years of piezometric well data, we analysed subsurface dynamics leading to environmental hazards in the region. We focused on identifying key periods of significant deformation pattern changes. The soft Wealden terrains (Lower Cretaceous) are characterized by alternating sandstones, clay, and sand facies, composing the sedimentary roof of an old mine drainage adit dug at 30 meters depth. The presence of this mined adit structure is contributing to the current vulnerability of the region. Especially, when the abandoned mine drainage adit was filled with water following the cessation of pumping. Due to an increase in the water level in the Wealden aquifer below the gallery, natural groundwater flow paths and pressures have increased over time. At least two significant mudflow outbursts, in 2009 and 2018, occurred. This study shows that both events were correlated with changes in water level and deformation. Moreover, results suggest a new phase of rising water levels and ground uplift due to increased pressure in the Wealden aquifer. A crucial outcome of this research is the assessment of the potential for another similar incident soon, informed by the correlation analysis of water level and ground displacement time series.

4.2. Introduction

Land subsidence is a gradual vertical or sinking movement of the Earth surface, arising from a variety of causes such as the compaction of underground strata and natural geological processes. This results in a noticeable decrease in ground elevation in specific regions (Galloway et al. 1999; Tomás et al. 2014; Figueroa-Miranda et al. 2018; Herrera-García et al. 2021; Bagheri-Gavkosh et al. 2021). Ground subsidence can be attributed to various factors, prominently the extraction of resources like oil, coal mines, and groundwater (Allen 1988; Meyer and Powley 1988). While many cases related to these causes have been extensively documented (Marschalko et al. 2012; Gonnuru and Kumar 2018; Métois et al. 2020; Cai et al. 2023; Chaussard et al. 2013; Orhan 2021), the impact of abandoned mines remains less explored in the literature. While the literature predominantly highlights the environmental problems of abandoned mines, it pays less attention to their physical hazards, and related issues (Salom and Kivinen 2020; Mhlongo 2023). The consequences of mining activities on the environment and human health extend well beyond the active mining period, persisting into the post-operational phase (Kivinen et al. 2018). Various factors drive mining closures—safety concerns, regulatory constraints, resource exhaustion, and economic considerations, among others (Rezun et al. 2001; Hartman and Mutmansky 2002; Syahrir et al. 2021). The geomechanical process underlying subsidence due to abandoned mines is complicated. When voids created by mining activities are left unfilled, they can become unstable over time. The overburden, or the layers of rock and soil above the void, starts to collapse into the empty space, leading to a decrease in ground surface level (Reddish and Whittaker 1989). The extent of subsidence, which can be influenced by factors such as the volume of the mined-out void, the depth of mining, and the geomechanical properties of the overburden (Lee and Abel 1983; Meng et al. 2021; Wang et al. 2022), has environmental implications. These include topographical changes (Palmer et al. 2010), disruptions to natural drainage (Lechner et al. 2016), ecosystem destabilization (Feng et al. 2022), groundwater pollution (Shepley et al. 2008), and the occurrence of challenges like acid mine drainage (Siriwardane et al. 2003).

The coal-rich region of Wallonia in Belgium has played an important part in the country's industrial advancement and overall economic growth (Saelens 2023). Coal mining began in the 12th century in Liège and Charleroi, and peaked in the 19th-20th centuries (Destatte 1997). With mining came the inevitable challenges – one of the most persistent of which is land subsidence. Mines in Wallonia, due to their depth and extraction methods, have led to various instances of ground deformation. Liège and Hainaut, in particular, experienced significant subsidence (Devleeschouwer et al. 2008a; 2008b; Declercq et al. 2021; 2023) , affecting infrastructure, and waterways, and even leading to occasional surface water inundation or minor flooding (Camelbeeck et al. 2022). By the mid-20th century, the coal reserves in Belgium were dwindling, and extraction costs surged. This culminated in coal mining becoming economically nonviable, leading to the closure of many mines (Esposito et al. 2021). This left behind environmental challenges, the main of which is land subsidence (Declercq et al. 2023; Schroeder et al. 2008).

As urbanized areas expand and interact with these historical underground cavities, the urgent need for careful monitoring, prediction, and management of associated ground hazards is revealed. Traditional monitoring methods such as leveling have long served as foundational techniques (Bitelli et al. 2000). The advent of technology introduced advanced systems like the Global Navigation Satellite System (GNSS) (Costantino and Angelini 2011) and Light Detection And Ranging (LiDAR) (Joyce et al. 2014). Despite their precision, these methods can sometimes be constrained in terms of spatial coverage or necessitate intensive data acquisition efforts (Palmqvist et al. 2021). Radar interferometry has introduced a range of methods suitable for different geospatial challenges. (Osmanoğlu et al. 2016). Techniques such as Differential Interferometric Synthetic Aperture Radar (DInSAR), a subset of Interferometric Synthetic Aperture Radar (InSAR), have been used to assess changes over time between multiple SAR acquisitions (Wang et al. 2020). Recent Multi-Temporal InSAR (MT-InSAR) techniques (Songbo et al. 2020; Tavakkoliestahbanati et al. 2024) including Interferometric Point Target Analysis (IPTA) (Werner et al. 2003; Yarmohammad Touski et al. 2023) and SqueeSAR (Ferretti et al. 2009) extend capabilities by analyzing displacement time series from both point-like and distributed scatterers. The Small Baseline Subset (SBAS) approach (Berardino et al. 2002) exploits small temporal and spatial baselines to minimize atmospheric artifacts and decorrelation effects, thereby enhancing the reliability and accuracy of surface displacement measurements over time. Persistent Scatterer Interferometric Synthetic Aperture Radar (PS-InSAR) is characterized by temporal consistency and extensive spatial coverage, particularly within urban environments. (Ferretti et al. 2000, 2001; Hooper et al. 2004). PS-InSAR uses coherent radar targets that remain consistent over a set of acquisitions (Estahbanati and Dehghani 2018). These Persistent Scatterers (PS) are typically associated with fixed elements. The advantage of PS-InSAR over other methods is its ability to detect millimeter-scale ground displacement across wide areas even in the presence of vegetation, by focusing on stable, reflective infrastructures. This capability is necessary for regions like Saint-Vaast, which, like many suburban areas in Belgium, is characterized by a combination of built environments and vegetation. Several studies have applied InSAR and its various techniques to investigate subsidence due to mining activities (Kim et al. 2022; Tian et al. 2024).

Saint-Vaast, a municipality located in Wallonia (Belgium), is an example of challenges associated with land surface deformation as evidenced by PS-InSAR (Choopani et al. 2022). Due to extensive coal mining that began in the late 19th century, the subsurface has experienced significant changes. These changes have transformed the region from a zone which was originally for resource extraction into the areas now characterized by high-risk of geohazards.

A drainage adit is situated approximately 30 meters below the surface in Saint-Vaast. The subsurface includes confined aquifers and sublayers that have been documented to have low mechanical stability. Historically, this drainage adit played a crucial role in coal mining period. In the present context, their existence, in combination with other subsurface features, is responsible for a series of geohazards. In February 2009, a clog rupture occurred causing significant damage to a residential area (7 houses, the pedestrian walkways, and the road itself were affected by ground deformations implying the formation of fissure cracks in the walls of the houses). In response to this event, a drainage pipe at the mouth of the adit was installed to drain the excess water to the river Haine, providing a mitigation measure against future similar incidents. Following the 2009 event, 6 piezometric wells were installed in the region to monitor the water level in the vicinity of the adit and the ground deformations observed at the surface. There was no piezometric data available to provide evidence of increasing water levels or instability prior to that event. This study aims to confirm and analyze these conditions, presenting evidence of deformation occurring before 2009. By 2018, the installed pipe became obstructed due to subsurface instabilities, likely including a collapse of loose sands from the Wealden deposits leading to a new phase of rise in the water level within the aquifer. This time the pipe effectively redirected the mudflow towards the river Haine, preventing further damage to the residential areas probably after a similar clog rupture inside the adit.

Analysis of these events has indicated a strong correlation between subsurface hydrodynamics indicated by piezometric wells and surface deformations observed by PS-InSAR. Consequently, this research enables the prediction of future similar events by integrating its findings.

For this research, we used satellite data that spanning a non-continuous period of 31 years for the Saint-Vaast region, including ERS (1992-2006), Envisat (2003-2010), and Sentinel-1A (2016-2023), acquired. The deformation maps resulting from processing of radar data, showed changing zones of gradual subsidence and uplift over time, closely aligning with areas historically associated with coal mining. The piezometric wells data closely align with the displacement time series obtained from PS-InSAR, indicating a strong agreement between the two.

Following the introduction, the paper is structured as follows: Section 2 outlines the geography and geology of the Region of Interest (ROI). Section 4.4 details the research methods and materials used. Section 4 presents the results, providing a clear understanding of the phenomena observed. Section 5 discusses the insights and implications of the findings. Finally, Section 6 concludes the paper with a correlation analysis between the displacement time series obtained from PS-InSAR and the water level data from piezometric wells. By identifying periodic patterns in these data sets, we aim to predict similar events in the future and develop a monitoring system to prevent and alert against recurring subsurface events, thereby protecting communities and infrastructure.

4.3. Region of Interest

4.3.1. Geographical and Geological Setting

The ROI is in Saint-Vaast, within the Hainaut region of Wallonia, Belgium. This region has historically been a significant coal mining zone. The ROI, situated in the Center coal basin, primarily encompasses La Louvière and extends to parts of five neighboring municipalities, including Manage, Morlanwelz, Binche, Estinnes-au-Val, and Mons. Adjacent towns include Le Roeulx, Seneffe, Chapelle-lez-Herlaimont, and Anderlues (Figure 4.1a).

Geologically, the subsurface consists of a Paleozoic basement corresponding to the NamurianWestphalian series (Upper Carboniferous) overlain by sedimentary series from the Meso-Cenozoic, Pleistocene, and Holocene eras. These latter deposits are primarily composed of colluvial and alluvial materials. The location of cross-section AA' has been added to Figure 4.1a.

The deep geological layers are mostly composed of Namurian-Westphalian (Upper Carboniferous) coal-bearing deposits from the Brabant para-autochthonous unit (Laurent et al. 2021). The folded coal-bearing sequence of the Paleozoic basement is divided by regional faults into several structural units referred to as 'massifs.' These massifs are grouped into three structural units on the Binche-Morlanwelz geological map: in the north, the Parautochthonous massifs; further south, at the edge of the study area, the thrusted massifs; and south of the study area, the Massif du Midi. In the studied region the Parautochthonous massifs are the Comble Nord Massif below the Placard Fault containing a normal sequence of Lower (carbonate) to Upper (detrital and coal-bearing rocks) Carboniferous. The ‘Massif du Placard’ is lying on the Comble Nord Massif through the Placard Fault. The ‘Massif du Centre’ is lying on the ‘du Centre’ Fault and is covered by the ‘Massif de Masse’ corresponding to a very complex thrusted structural and thick unit (1200 m) topped by the Midi Fault.

Figure 4.1 Location of both 2009 and 2018 events on a geological map from Wallonia geoportal (modified from (Frippiat et al. 2013)). The location of cross-section AA' has been highlighted, b topographical map from Shuttle Radar Topography Mission (Farr et al. 2007) and highlighting hydrographic networks and Wealden terrains and watersheds.

The southern area reveals Lower Devonian rocks (essentially sandstones, phyllites, and conglomerates rocks) of the Ardennes allochthonous unit thrusted towards the North by the Midi Fault on top of the Upper Carboniferous coal-bearing deposits. The northern area is marked by limestones and dolomite rocks of the Lower Carboniferous also part of the faulted and folded Brabant Para-autochtonous unit. Above the strongly structurally deformed Paleozoic sequence, the Meso-Cenozoic cover is a combination of Cretaceous clays and sands (Wealden deposits), marls (Turonian in age), and chalks (Turonian to Santonian in age), forming part of the Mons basin. The upper part of the Meso-Cenozoic cover contains Paleocene and Eocene clays and sand sediments (the Hannut and Carnières Formations respectively) linked to the North Sea basin extension (Drevet et al. 2010). The Saint-Vaast area is overlain by Pleistocene loam deposits and alluvial sediments along the alluvial plain of the Haine River. The Wealden deposits are Lower Cretaceous sediments, but their age is changing throughout the Mons Basin from the western side (Barremian) to the eastern side (Albian) (Yans, 2003). The Wealden sediments are generally found in kilometric lenses trapped in the depressions of the Palaeozoic basement but also inside natural karstic features distributed throughout the Paleozoic carbonate top surface. The Wealden deposits have been mapped originally by Marlière (1946) and more recently from core descriptions and allowing to propose of a revised cartography of the Wealden deposits around Saint-Vaast (see Figure 4.1, report ISSeP from 2010).

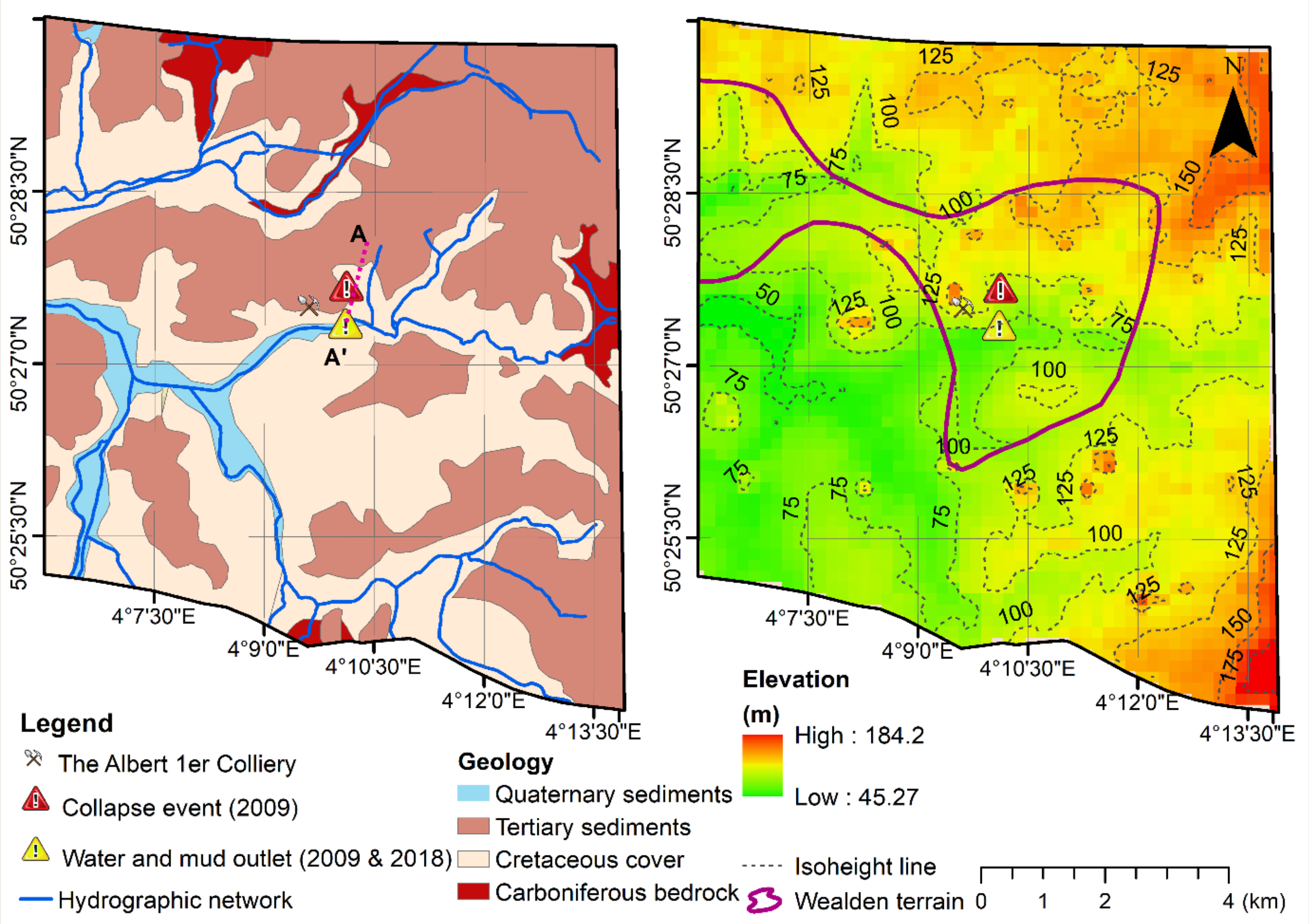

Figure 4.1 Location of both 2009 and 2018 events on **a** geological map from Wallonia geoportal (modified from (Frippiat et al. 2013)). The location of cross-section AA' has been highlighted, **b** topographical map from Shuttle Radar Topography Mission (Farr et al. 2007) and highlighting hydrographic networks and Wealden terrains and watersheds.

Hydrographically, the region lies in the Haine sub-basin of the Scheldt basin, which reaches the Canal du Centre to the north and is flowed by the Haine from east to west (Figure 1.b). Prominent tributaries include the Ruisseau des Estinnes and Ruisseau de la Princesse. The Haine originates in Anderlues and is fed by multiple smaller streams, like the Olive stream and Marais stream. Urbanization is most prevalent in the north, where the Canal du Centre intersects the region. This area is marked by the Strépy-Thieu boat lifts and the Canal du Centre Historique. Waterway routes in this zone, such as the Thiriau du Luc and its tributaries, often intertwine with the Canal du Centre Historique path (Drevet et al. 2010).

The study area relief is affected by traversing watercourses and is marked by colliery spoil heaps, some even exceeding 190 m in height (Figure 1. b) (For detailed information on the Albert 1er spoil heap, see Destination Terrils: Terril Albert 1er.). Its average altitude is around +100 m, but this varies with +75 m elevations to the northwest and about +150 m to the southeast (Figure 1.b). The river Haine is the predominant hydrological feature in the study area, situated 608 m to the south of the initial incidence point. Central to the study area is drawn the mapping of an underground adit corresponding to an old adit located in the upper part of the thick lens of Wealden deposits. A detailed view of the geological features, including the direction and approximate depth of the adit, along with the schematic location of drilled piezometric wells is shown in the cross-section (Figure 4.2).

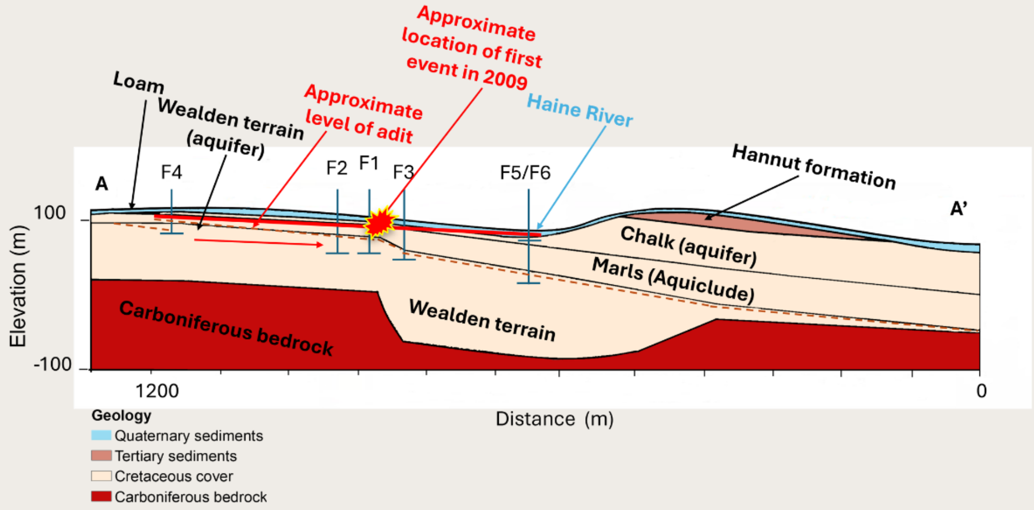

Figure 4.2 Cross-section AA' (highlighted in Figure 4.1a) illustrating the geological layers and the position of the drainage adit. The section highlights the direction and approximate depth of the adit relative to the Wealden deposits, as well as the overlying Turonian marls and Cretaceous aquifer.

This mining adit is horizontal or slightly inclined and was possibly excavated to access a water-bearing storage level inside the Saint-Vaast hill. The “Charbonnages de La Louvière et Sars-Longchamps” colliery with the mine shafts 9 and 10 of the coal extraction site Albert 1er, started in 1914 and stopped in 1961, is the nearest active colliery in Saint-Vaast (Nicau, 2024). The latter colliery ceased the same year and was included in a bigger operational colliery named “Charbonnages de Ressaix-Mariemont-La Louvière" still supervised administratively by the regional Walloon administration. Given the proximity of the adit drainage with the active coal exploitation Albert 1er site, there is an issue most probably in relation to underground water fluxes from the nearby hill area containing the Cretaceous aquifer (chalks) and aquiclude (Wealden and Turonian marls). Turonian marls constitute a relatively impervious cover with a thickness of 20-30 m acting as a hydraulic barrier and confining the Wealden underground water located in the sandy layers, potentially located at the top of the Wealden deposits (Frippiat et al., 2013). The significance of this adit is further highlighted by its evident role in the documented events and the geospatial estimations of land subsidence and uplift as revealed by PS-InSAR data. Given its importance, our focus will narrow to the region surrounding this adit, offering more detailed research and discussions (Figure 4.3).

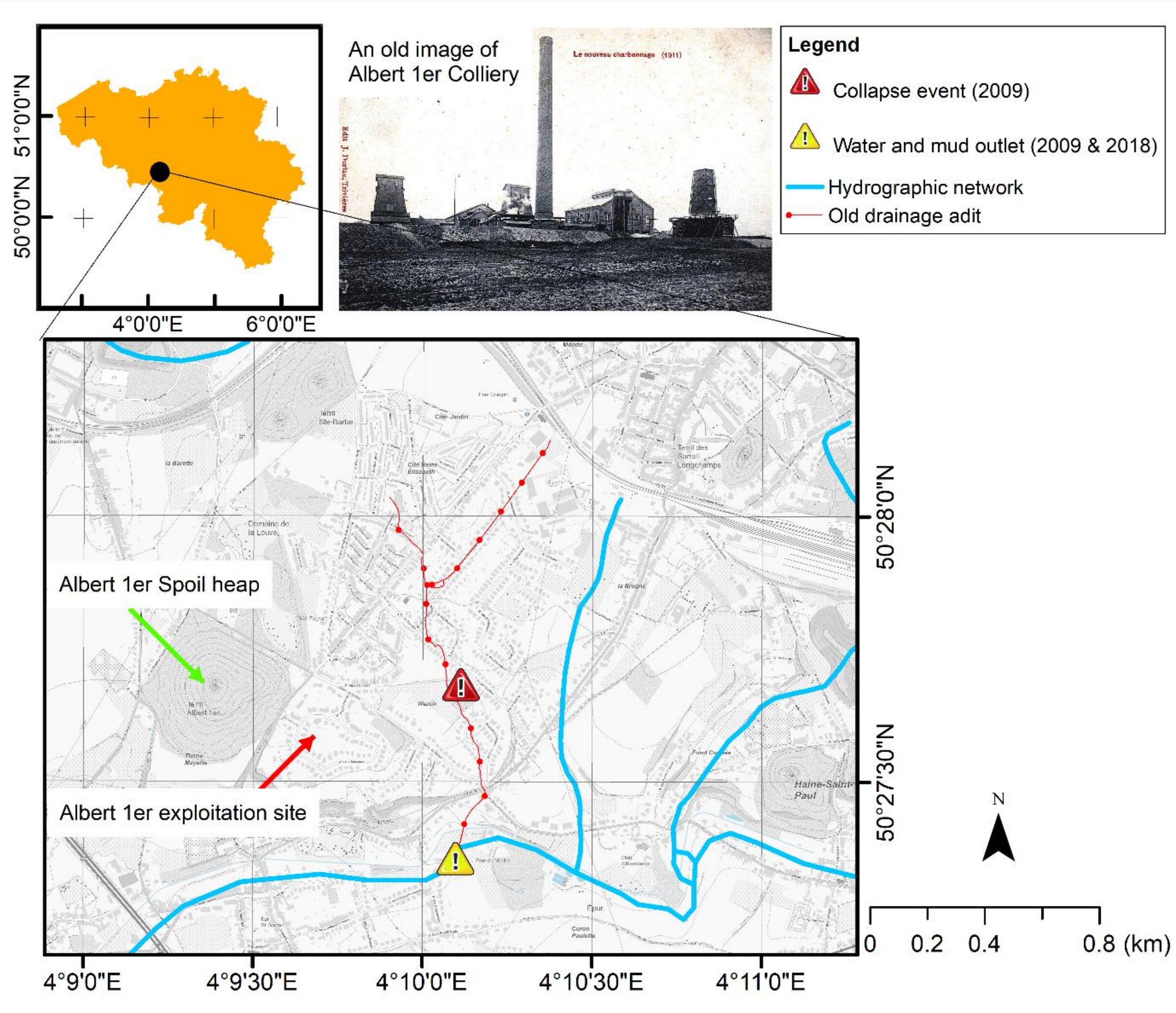

Figure 4.3 Detailed geospatial mapping of the historical underground gallery near Albert 1erColliery. The topographical background map is sourced from CartoWeb (NGI).Inset black and white photo adapted from (Hudson Institute of Mineralogy, n.d.) showing the Albert 1er colliery in Saint-Vaast (photo copyrighted to J. Duriau, Trivières).

4.3.2. Saint-Vaast Incidents of 2009 and 2018

The most important geological feature in the Saint-Vaast subsurface is the presence of the Wealden terrains (Figure 4.1a). The Wealden geological layer features a complex stratigraphical sequence, with clayey horizons at the top transitioning to more mixed sandy-clay compositions at depth. These deposits are kilometric lenses located in very localized depressions of the Paleozoic basement in general and specifically present here in the Saint-Vaast area. Their formation resulted from continental sedimentary processes and environments during the Early Cretaceous period, characterized by alternating deposition of clay and sandy layers. The clayey horizons are originally located in the middle and lower part of the sequence, while the mixed sandy-clay deposits are found at the top. The sandy portions have high permeability and can store and transmit substantial volumes of water. In contrast, the clayey sections act as impermeable barriers, often trapping and isolating water bodies in sandy lenses inside the clay horizons. Alongside these terrains, coal-bearing aquifers are present, which are essentially water-bearing layers associated with the exploited coal seams. These aquifers play a pivotal role in the hydrogeological dynamics of the region although the top of the Paleozoic basement has been strongly affected by the weathering with clay sequences that are sometimes very difficult to distinguish from the clay layers of the Wealden deposits itself. Their interactions with the overlying and underlying terrains, especially the Wealden clayey horizons, determine much of the subsurface water flow and storage patterns (Drevet et al., 2010). Given the geological characteristics of the Wealden terrain, this study examines the incidents that occurred in 2009 and 2018 in Saint-Vaast where Cretaceous chalk layers overlay impermeable Turonian marls above the loose sands of the Hainaut Group. These sands, saturated and under excessive pressure, put the gallery at risk due to the pressure difference between the upper underground aquifers and the high level of the Haine River. Over long periods, such conditions can accumulate significant potential energy. A natural or anthropogenic disruption in the Wealden clay horizon could cause the pressurized water from the Wealden confined aquifer to be released suddenly, as observed in the 2009 and 2018 incidents. The pressurized release can be even more pronounced if the coal aquifer, at any given point, directly interfaces with the sandy Wealden terrains. Considering the extensive mining history of the region, abandoned mining galleries and shafts may have served as potential pathways or reservoirs for groundwater flow. Given their expansive and interconnected nature, this adit plays a crucial role in subsurface hydrodynamics.

To better understand these dynamics, a cross-section showing the hydrogeology of the region, including the locations of piezometric wells and the variabilities in the lithology of the Wealden terrain at each piezometer, has been created (Figure 4).

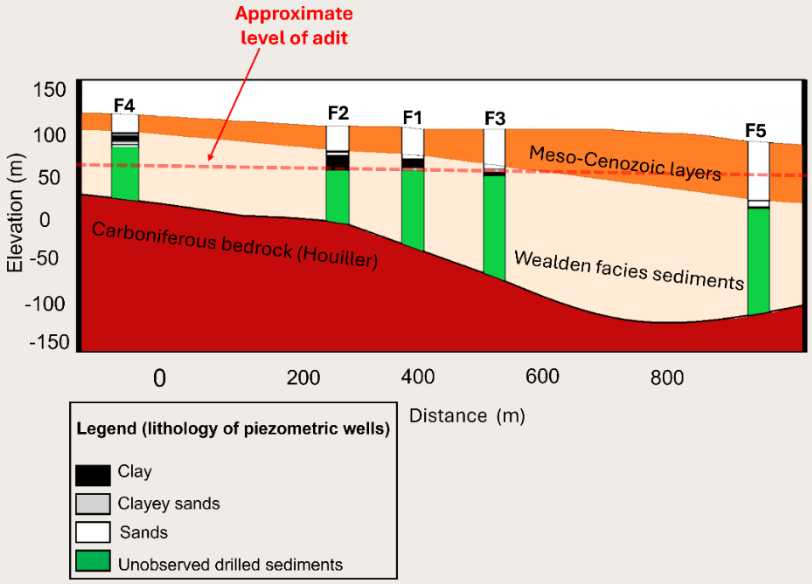

Figure 4. 4 Geological cross-section over the piezometric wells F1 to F5 in the Saint-Vaast region, illustrating the lithological variability of the Wealden terrain across different piezometric wells, modified from (Drevet et al. 2011).

When active, mining operations often involve dewatering processes to keep these galleries free from groundwater influx. This is typically achieved by pumping out the water that seeps into the mine shafts and the exploited underground galleries. However, once mining ceases and dewatering is stopped, groundwater starts to reclaim these anthropic voids left from the exploitation. The abandoned galleries and shafts begin to act as conduits, allowing water to flow more freely than through the surrounding rock or sediment. Indeed, they can significantly change the natural flow paths of groundwater. This has profound implications for the hydrogeological dynamics of the region. If these saturated galleries and shafts are close to or intersect with other geological formations, like the Wealden terrains or coal-bearing aquifers, they can influence water movements between them. For instance, the presence of adit features inside the Wealden deposits in the Saint-Vaast hill where these galleries are near the surface or have compromised mechanical integrity due to the presence of loose sand pockets might imply sudden water discharges, especially if there is a significant pressure differential due to the formation of a plug associated to the confined water-bearing sandy lenses in the Wealden deposits. This can explain the anomalies observed in the area.

4.4. Methods & Materials

4.4.1. PS-InSAR Technique, Processing, and SAR Datasets

Synthetic Aperture Radar (SAR) data, when analysed through the PS-InSAR technique, has significantly advanced the monitoring of ground deformations from space. A challenge, however, arises when there is an absence of man-made structures in the study area, or when the deformation does not conform to a predefined temporal model (Crosetto et al. 2016). Stanford Method for Persistent Scatterers (StaMPS) is developed to overcome traditional PS-InSAR limitations. The method did not rely only on the presence of man-made structures for detection and was able to find low-amplitude natural targets (Hooper et al. 2004, 2007). The methodology creates N interferograms from a set of N+1 SAR images, acquired over different time intervals (Sadeghi et al. 2013). These images are then related to a designated master image, a process optimized to maximize stack coherence. The criteria for selecting PS candidates are based on the amplitude dispersion index (Shamshiri et al. 2018). This quantitative measure evaluates the stability of the target radar backscatter over time. Stable targets typically exhibit lower amplitude dispersion values and are, therefore, indicative of potential PS candidates. The fundamental inputs for PS-InSAR are interferograms – products that include the phase difference between two SAR acquisitions, thus revealing ground displacements that occurred between the two acquisition times. To produce these interferograms, a set of SAR images is required, where a specific image is chosen as a 'reference' and the others are termed 'secondary'. The difference in phase between the reference and each of the secondary images generates individual interferograms (Dehghani and Nikoo, 2019). In our study, the Delft Object-oriented Radar Interferometric Software (Doris) (Kampes 1999), was used for interferometric processing of Single Look Complex (SLC) data of both the ERS and Envisat satellites. While Doris can handle Sentinel-1A data, for our research goals, Sentinel-1A data was processed using the InSAR Scientific Computing Environment (ISCE) (Rosen et al. 2012). Upon interferogram generation, PS-InSAR protocol, driven by the StaMPS, employs the amplitude dispersion index as a foundational metric (Osmanoglu 2011). This criterion which is linked to the stability of radar backscatter over time, is very important in the detection and monitoring of PS points. This method ensures that the detected deformation signals belong only to those scatterers exhibiting stability, thus refining the accuracy and reliability of the resultant deformation insights. To measure the expansion and dynamics of ground deformation in Saint-Vaast, we integrated three C-Band SAR datasets spanning three decades. Our study started with an analysis of ERS1/2 satellite imagery spanning the period from 1992 to 2001. This was succeeded by ENVISAT images, covering the years from 2003 to 2010. We subsequently incorporated Sentinel-1A imagery from the years 2016 through 2023 into our dataset. The resolution of these data is presented in Table 4.1 (Zebker et al. 1994; Small et al. 2003; Bourbigot 2016). An external Shuttle Radar Topography Mission (SRTM) Digital Elevation Model (DEM) was used to mitigate topographic distortions inherent in the interferometric phase data. Following SAR data processing, we identified PS by applying a threshold for temporal coherence, set at a value bigger than 0.7. This threshold is usually considered as specific criteria, which assess the reliability of scatter points based on their consistency in reflecting radar signals across multiple acquisitions (Kenner et al. 2016; Chen et al. 2018). Certain temporal gaps between ENVISAT and Sentinel-1A were evident. Nonetheless, the integrated data provides the deformation dynamics in Saint-Vaast across a non-continuous span of three decades. We used 98 descending ERS, 129 descending Envisat, and 187 Sentinel-1A ascending images spanning between April 1992 to January 2001, March 2003 to October 2010, and June 2016 to April 2023 respectively. Table 4.1 delineates the specific attributes of the three SAR datasets employed in this study. Figure 4.5 shows the perpendicular baseline against temporal baselines of the generated interferograms.

Table 4.1 Summary of SAR datasets used for analysis.

Satellite	Number of interferograms	Start date of spanning	The end date of the spanning	Reference date	Number of PS per km^2	Imaging geometry
ERS 1/2	74	26/04/1992	03/01/2001	18/02/1998	98	Descending
Envisat	73	19/03/2003	13/10/2010	15/08/2007	129	Descending
Sentinel-1A	203	07/06/2016	20/04/2023	20/09/2019	187	Ascending

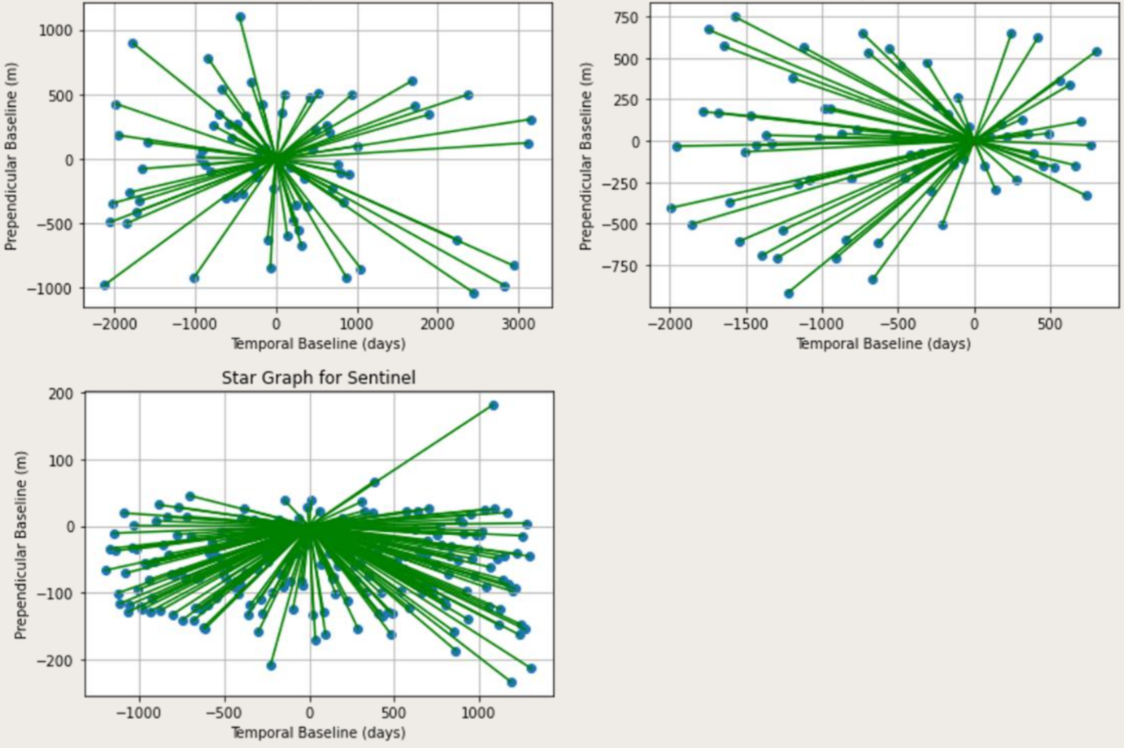

Figure 4.5 Star graphs showing perpendicular baselines (in meters) against acquisition dates for three SAR-image datasets, spanning the ERS, ENVISAT, and Sentinel-1A periods.

4.4.2. Water Level Monitoring

To assess the risk of an accident of this type recurring in Saint-Vaast a detailed study of the piezometry of the aquifers was conducted by the Public Service of Wallonia. Piezometric wells, monitoring the Wealden and Chalk aquifers in the Saint-Vaast area, offer insights into the subsurface hydrology influenced by historical mining activities. Five piezometers (F1 to F5) near the collapsed area were cored in the Wealden facies to assess the potential influence of historical mining activities on groundwater pressures. Piezometer F6 in the vicinity of the collapse region was specifically set up to monitor the water level in the chalk aquifer to understand its hydrological behaviour and interactions. The location of the different available piezometers in the studied area is shown in Figure 4.6.

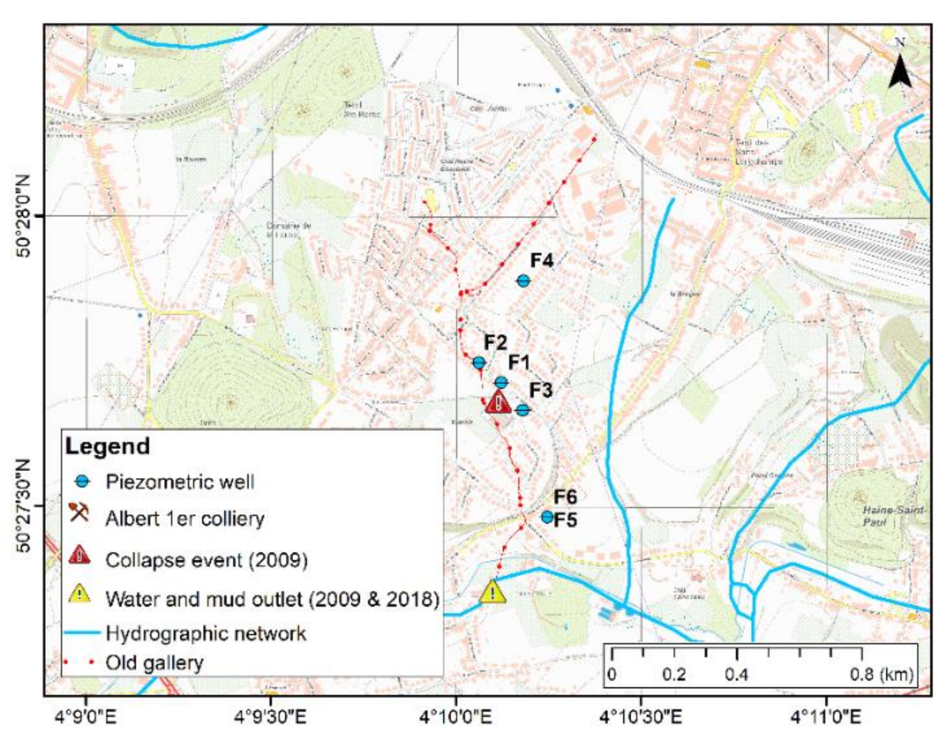

Figure 4.6 Location map of piezometric wells concerned with the study. The map background is sourced from CartoWeb (copyrighted to NGI).

4.5. Results

In this part of the paper, we present the results and discussion of our study on land surface deformation of the Saint-Vaast region. Our analysis using 3 decades of SAR data and 13 years of piezometric wells monitoring, explains the ground deformations and its hydrogeological drivers. Comparison between the SAR estimations with hydrogeological measurements shows a significant correlation between groundwater level variations and surface displacement during specific intervals within the study period.

4.5.1. PS-InSAR Displacements

In our investigation of ground displacement in the Saint-Vaast area, we used PS-InSAR analysis across three distinct radar datasets from 1992 to 2023. We estimated significant displacement trends within a 5.7 square kilometer region of historical mining activity. Initially, from 1992 to 2001, this zone exhibited uplift movement with an average displacement of 2.65 mm/year, peaking at 4.49 mm/year along the LOS (Figure 4.7a). The period between 2003 and 2010 showed a stabilization in LOS displacement rates, averaging 0.94 mm/year. During this time, fluctuations range from a slight subsidence of -0.96 mm/year to an uplift of up to 1.5 mm/year along the LOS (Figure 4.7b). This period indicates a transient equilibrium within the subsurface structures. Contrasting to these periods, the recent years from 2016 to 2023 marked a notable shift to land subsidence, with an average LOS displacement rate of -1.24 mm/year, descending to a minimum of -3.65 mm/year (Figure 4.7c). The velocity values along the Line of Sight (LOS) illustrated in Figure 4.7 provide a ground displacement velocity but should be interpreted with caution, as they may not fully represent the deformation dynamics over the entire estimation period. While the mean LOS velocity during the Sentinel-1A satellite monitoring period suggests a trend of subsidence, a closer examination of the recent time series data shows a beginning pattern of an uplift.

The displacement values obtained from PS-InSAR are calculated relative to a reference point. This reference point, assumed to be stable, is a key factor in PS-InSAR processing. For the ERS data (1992–2001), the reference point was located at a specific latitude and longitude (4.54° E 50.932° N), part of a broader regional processing. For the Envisat (2003–2010) and Sentinel-1A (2016–2023) datasets, a presumedly stable reference region was identified near the dynamic deformation area based on the stability observed during the ERS period. Specifically, the reference point for Envisat and Sentinel-1A data was located at coordinates [4.05, 50.51], with a 50-meter buffer around it. In other words, the time series shows displacement relative to the average deformation of all PS inside this specific area. All displacement values in the Envisat and Sentinel-1A analyses were calculated relative to this reference point, ensuring consistency and minimizing potential bias from reference point movement. However, the assumption of reference point stability remains a critical consideration in long-term subsidence assessments. It will be addressed in chapter 5 in detail.

Different trends over time, emphasize the complexity of deformation processes in the Saint-Vaast region, where short-term fluctuations can significantly deviate from longer-term trends. Figure 4.7 also illustrates how the pattern of deformation, including both uplift and subsidence phases, symmetrically aligns along the boundaries of the Wealden terrains. This alignment revealed by PS-InSAR time series analysis, emphasizes the geological influence on deformation dynamics. Additionally, Figure 4.7 shows the location of piezometric wells to highlight their position in the pattern of deformation.

In Figure 4.7, it is important to account for the incidence angle multiplication factors when interpreting the LOS velocity values. The LOS displacement values represent a combination of movements in 3D directions projected along the satellite's line of sight. Having the local incidence angle at each PS point, the deformation can be projected onto the vertical or horizontal direction. The scale factor for the projection of LOS deformation onto vertical directions is provided in Table 1.1 in section 1.3. In the table, the scale factor is based on the local incidence angle measured at the middle of each region, and it varies slightly depending on the geometry of the radar acquisition in different datasets. For the PS points located within a 200 m buffer area from the cross-sections BB' and CC' (solid purple lines in Figure 4.7), the LOS velocity during the three satellite periods is further estimated and illustrated (Figure 4.8). Additionally, a time-lapse of yearly changes in LOS velocity maps is provided in the supplementary materials.

As shown in Figure 4.8a, a consistent positive peak of deformation along the cross-section BB' during both the ERS and Envisat periods is centered around the longitude at 4.17. with increasing and decreasing LOS values respectively before and after the peak. The ERS data indicate a higher uplift at this peak, while during the Envisat period, the general deformation pattern across the region tends towards stability, yet a slight uplift is still estimated along the cross-section, with a lower peak compared to the ERS period. Conversely, Sentinel-1A data reveal a transition to subsidence displaying the highest rate of land subsidence along the cross section around the longitude 4.175.

This deformation pattern, with an increasing trend towards the centre of the land subsidence bowl, and the center of maximum movement shifting slightly over time compared to the peak in the uplift, indicates a dynamic subsurface process, evolving from uplift to land subsidence.It has to be noted also that the three periods have a significant stability area from the longitude interval 4.1775 to the end. An increasing trend in the LOS velocity values is also visible before the longitude 4.1775 starting from the lowest negative LOS velocity values. The end of the cross-section reached the urbanized area of La Louvière where the subsurface data seems to indicate a very reduced amount of Wealden deposits with a reduced cover of Meso-Cenozoic deposits.

CC' is along the axis of the semi-symmetrical shape of the Wealden terrains, running in a northwest-southeast direction. As shown in Figure 4.8b, during the ERS period, like BB', there is an uplift along the cross-section. However, moving from C to C', the value of uplift increases towards the lobe of the Wealden border. Unlike BB', the uplift at the end of the cross-section does not turn into subsidence but continues to show uplift, though at a lower rate.During the Envisat period, similar uplift is observed along CC'.

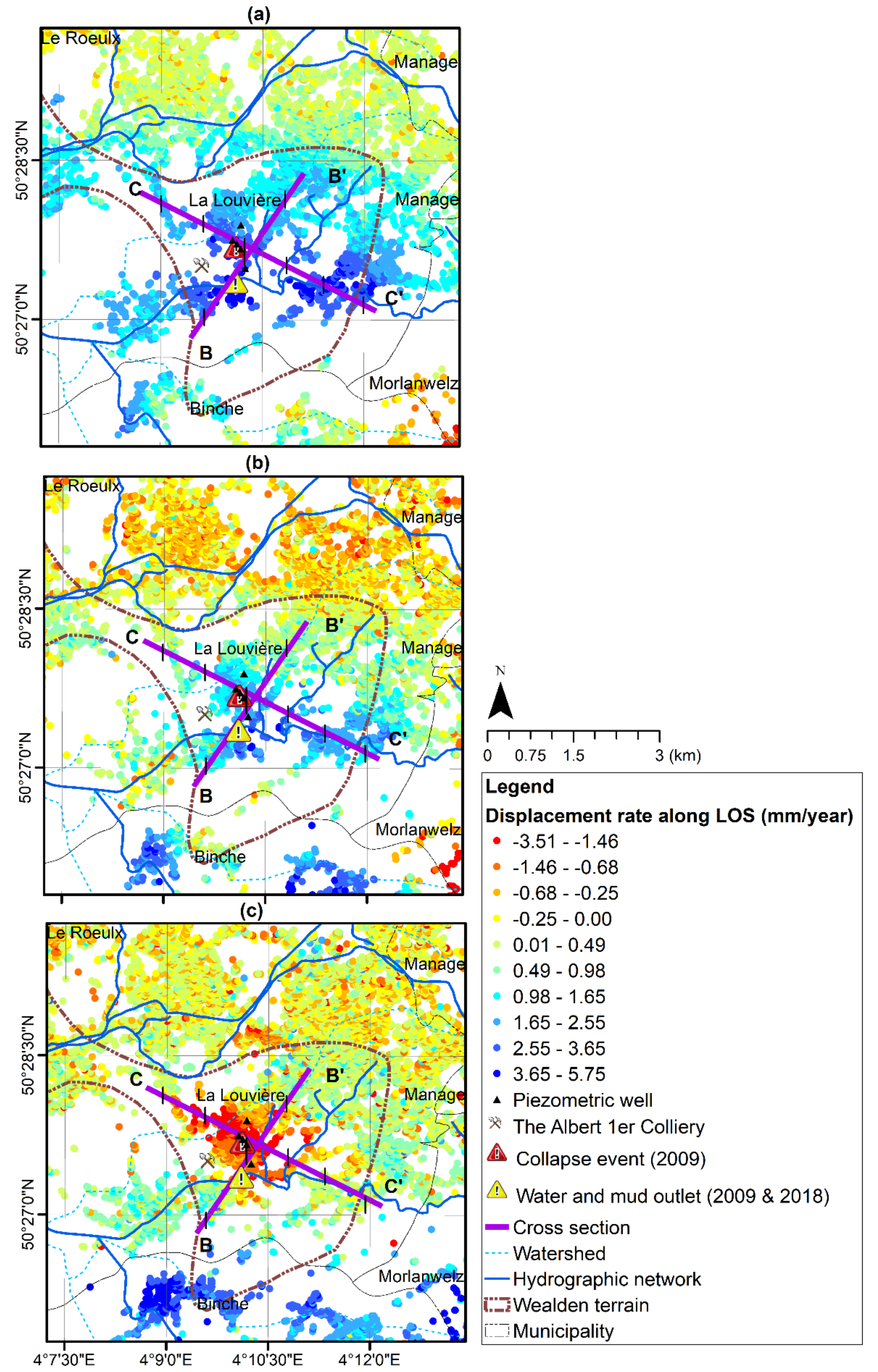

Figure 4.7 Mean velocity map of Saint-Vaast region along LOS direction during **a** ERS period (1992-2001), **b** ENVISAT ASAR period (2003-2010), and **c** Sentinel-1A period (2016-2023). Incidence angles for each plot, which affect LOS deformation interpretation, are provided in Table 1.1.

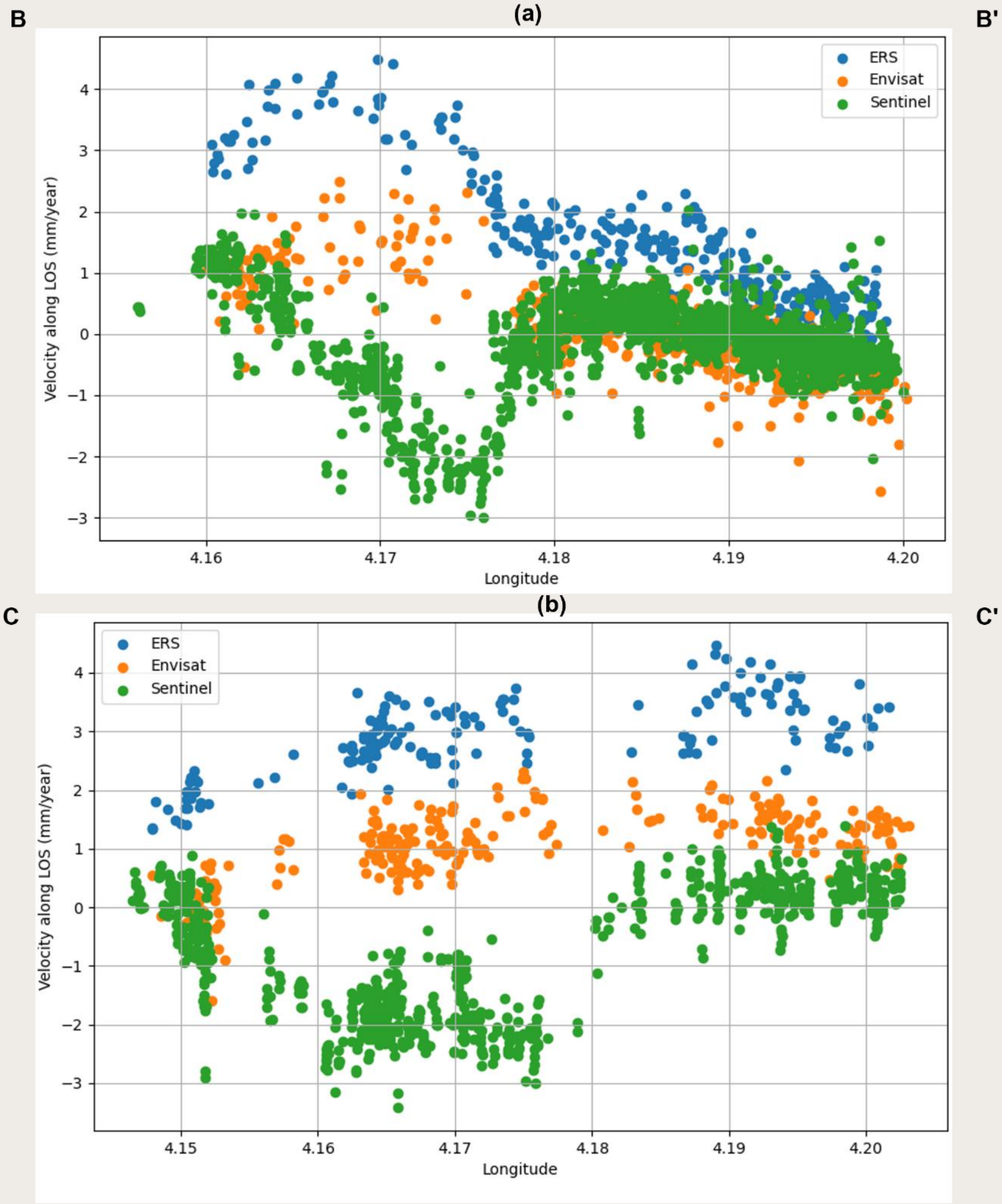

Figure 4.8 Average LOS velocity for PSs located within a 200 m buffer along **a** cross-section BB' **b** cross section CC' (highlighted in Figure 4.7) passing over the deformation zone during three periods.

However, the uplift rate is slower, and the general deformation pattern shows a gradual decrease in uplift. By the end of the cross-section at C', the deformation stabilizes. Sentinel-1A data reveals a transition to subsidence displaying the highest rate of land subsidence along the cross-section from C to C', similar to BB'. The value of the peak subsidence is the same as observed in BB'. However, in BB', the minimum peak is very sharp, indicating that the subsidence sharply reaches its lowest point around longitude 4.175, transitioning from stability at the beginning of B. In contrast, along CC', the subsidence smoothly reaches the same peak, maintaining this peak until around longitude 4.185, and then gradually stabilizes. The differences between the three periods are, in part, due to the use of different reference points for each satellite mission. The ERS data uses a specific reference point as part of a larger processing (located at specific coordinates mentioned previously), while the Envisat and Sentinel periods use a reference point that was chosen near the center of the area based on its stability during the ERS period. Any potential movement of these reference points could slightly influence the interpretation of the results. For example, while the reference points are assumed to be stable, even a slight shift in the reference point could cause a relative overestimation or underestimation of the displacement along the LOS for a given period.

Analysis of cross-sections BB' and CC' suggests that the deformation processes in the region are influenced by the orientation and distribution of the Wealden terrains, leading to more uniform deformation patterns along CC'.

4.5.2. PS-InSAR Timeseries Analysis

In the following, we implemented data processing and investigated land deformation, building upon the processed dataset of PS-InSAR time series derived from the StaMPS software. Our analysis concentrated on identifying and interpreting breakpoints within the time series data to gain a deeper understanding of the relation between displacement values and incidents in the region. Breakpoints are those dates where significant shifts in the deformation rate are observed, indicative of underlying hydrogeological processes and their influences that change the deformation dynamics. The identification of these breakpoints is crucial for understanding the temporal evolution of land deformation, as they signify periods where the deformation trend undergoes notable changes. Our analysis defines multiple linear trends by identifying breakpoints, which represent distinct phases of uplift or subsidence. Within these smaller sections, linear trends are sufficient to capture the nature of the deformation process. This approach focuses on the overall pattern of deformation, as it directly relates to significant changes in water levels. The goal is to understand the correlation between the main trends of uplift or subsidence and the rising or drawing of water levels, rather than accounting for seasonal or minor fluctuations that do not influence the broader trend.

This observation is significant as these breakpoints are consistently present across all five displacement timeseries (Figure 4.9). These timeseries correspond to the average timeseries of PSs located within a 100 m radius of five piezometers, labeled F1, F2, F3, F4, and F5/F6—the latter two being co-located (Figure 4.6). Incorporating these points helps explain the clog ruptures that occurred in 2009 and 2018. The ERS satellite data spanning from April 1992 to January 2001 provided the first estimations of displacement in the region. Throughout this period, the time series data indicated a consistent uplift until April 1998, after which a phase of relative stability was observed across all piezometric wells until 2001 except for F4, which showed subsidence after April 1998. (Figure 4.9). Although no specific incidents were documented during this stable phase from April 1998 to January 2001, the historical context and subsequent deformation patterns suggest the possibility of an unreported subsurface event occurring during that time. From March 2003 to the end of January 2009, our analysis of Envisat satellite data revealed a notable uplift in all 5 timeseries, with rates reaching 3.44 mm/year near F5/F6 wells and reducing to 1.3 mm/year around F4. The locations of these piezometers are shown on the velocity map (Figure 4.7). The last year of the Envisat period (January 2009-October 2010) showed a stabilization in the trends across the all-time series. This phase of relative stability ended just before the first documented clog rupture event in February 2009. This suggests a correlation between the end of the uplift phase and the hydrogeological disturbances.

One important point is that the ERS, Envisat, and Sentinel-1A data sets were processed independently, and the reference points used for each are different. Additionally, we cannot assume that the trend observed in the ERS time series should continue indefinitely or align perfectly with later datasets like Envisat and Sentinel-1A.

The SAR data showed that a regional pattern is visible and most probably in relation to the subsurface activities of the coal mines in this part of the basin. The cessation of the groundwater pumping activities due to mining closure led to a gradual rise of the groundwater levels, increasing pore water pressure and reducing effective stress in the subsurface, weakening the soil or rock structure. This long-term evolution is illustrated by a regional uplifting trend in the studied area that is still visible during the ERS period. The ENVISAT period is still highlighting this trend in the southern area while the northern area showed negative LOS velocities suggesting a land subsidence affecting the urban areas of Le Roeulx, La Louvière, and Manage. The end of this uplifting trend is clearly visible during the Sentinel-1A data where the LOS velocity values indicate stable conditions mostly for the central and northern areas while the southern area continued to show uplifting conditions.

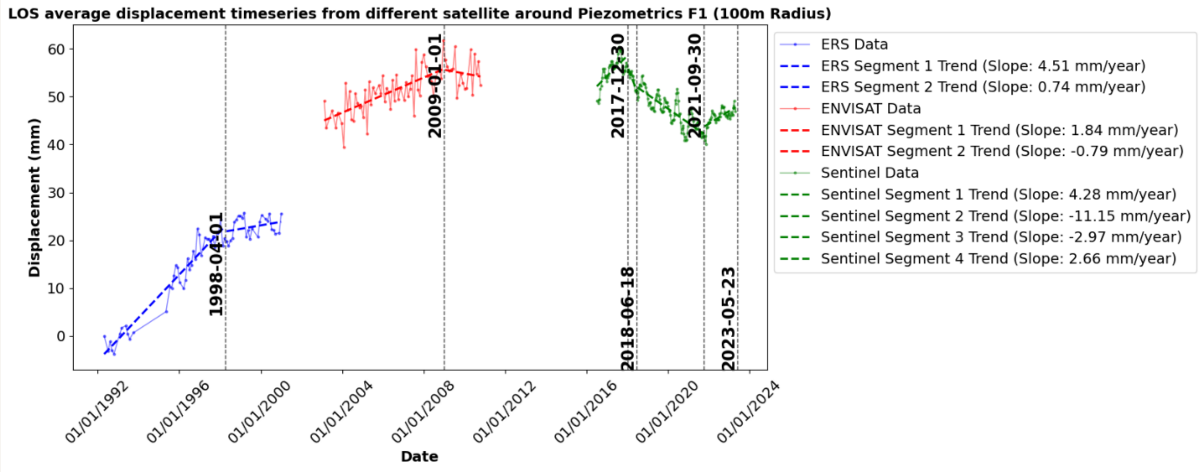

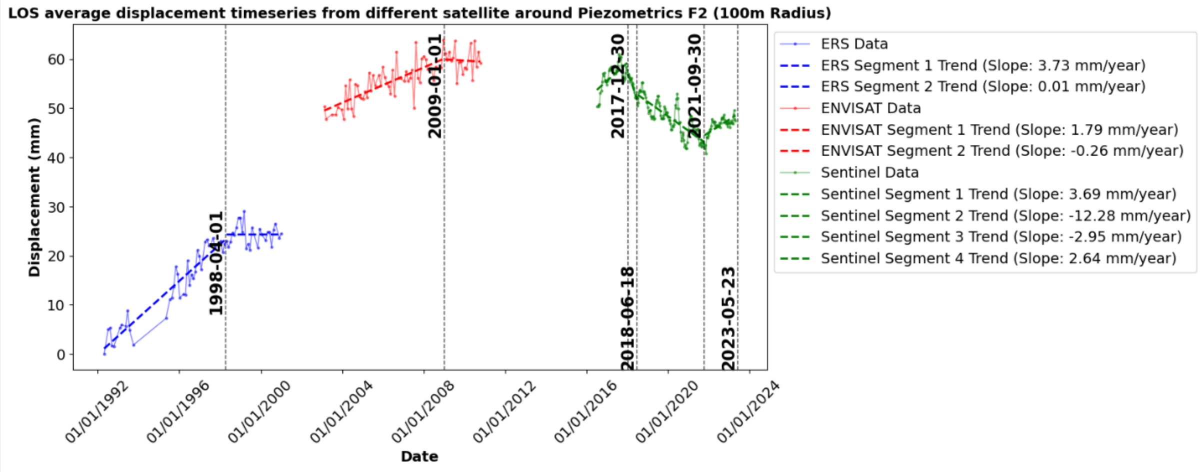

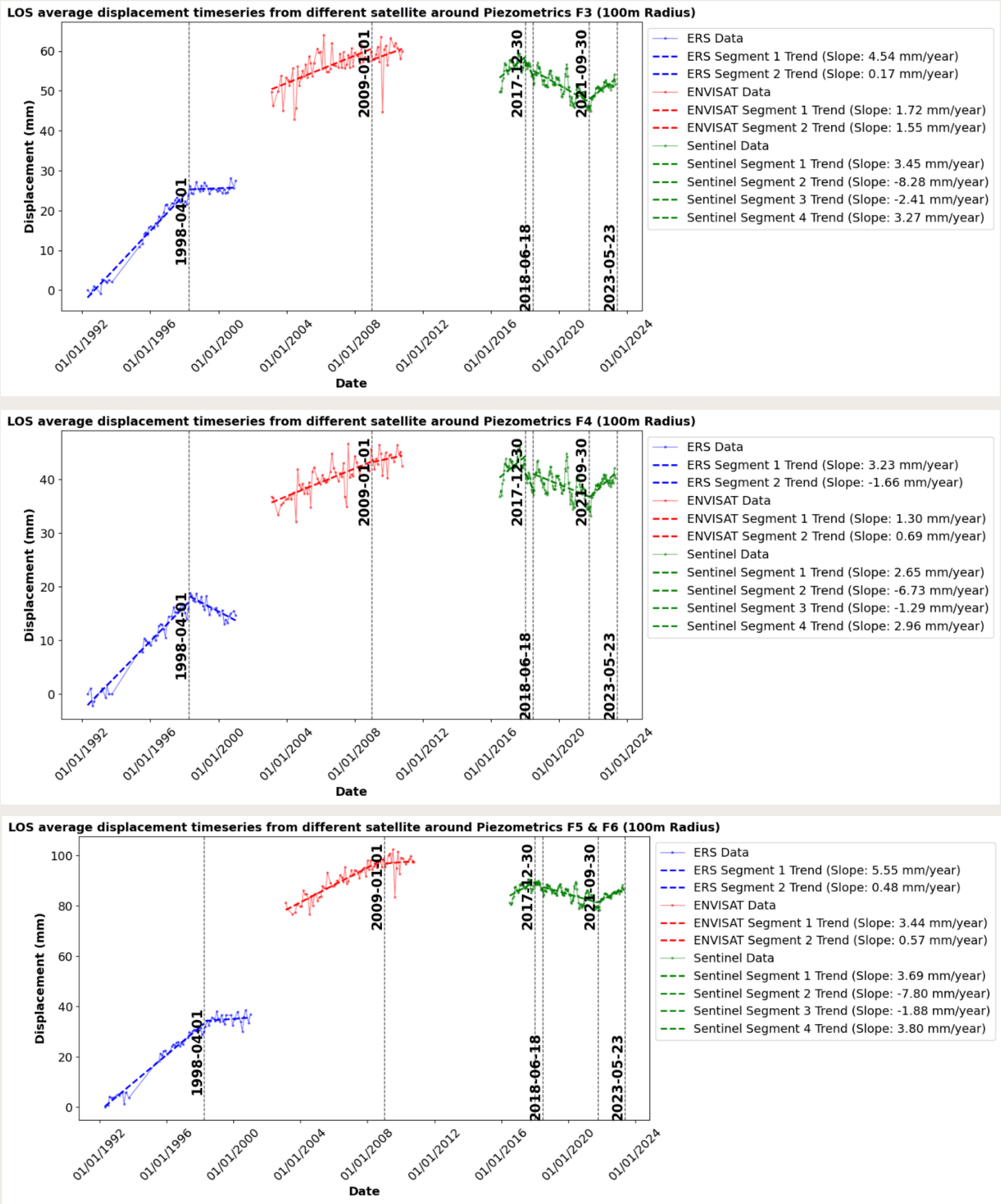

Figure 4.9 LOS displacement timeseries from ERS, Envisat, and Sentinel-1A data for the PS points in the vicinity of piezometric wells, averaged for all PS points located within a radius of 100 m from each piezometer. Incidence angles for each plot, which affect LOS deformation interpretation, are provided in Table 1.1.

Looking now to the studied area of Saint-Vaast, a different pattern is visible with strong positive, slightly positive to almost stable, and negative LOS velocity values respectively during the ERS, ENVISAT, and Sentinel-1A time interval. This process illustrated the change of the behaviour from uplifting conditions to the progressive development of the land subsidence bowl. The rising trend indicates the progressive influx of groundwater that can accumulate in the confined Wealden water-bearing sandy lenses causing an initial uplift (2003-2010), followed by a period of stability (January 2009-October 2010) as pressures balanced. Eventually, the continuous pressure buildup exceeded the subsurface material strength, triggering the 2009 clog rupture through sudden pressure release. The radar data gap from October 2010 to June 2016 limited direct estimations, yet it is possible that the ground surface initially subsided during this time. This resulted from the expulsion of large volumes of water and mud due to the 2009 rupture. Not only the release of water but also the transition of the materials of sand and clay from the Wealden terrain contributed to this subsidence. This temporarily reduced the sub-surface pressures, leading to land subsidence. However, with the clog of the pipe, which was installed after the event of 2009, pressures would have gradually built up again, initiating a new uplift phase. The exact onset of this uplift is uncertain, but Sentinel-1A data from June 2016 onwards captures the final phase of this uplift period till December 2017. During this period maximum and minimum uplift of 4.28 and 2.65 mm/year in the vicinity of F1 and F4 was observed respectively. This was followed by a shift to subsidence (around June 2018). The start of this subsidence phase coincided with the second clog event in the pipe installed post-2009, leading to an increase in pore pressure once again. However, unlike the previous incident, no rupture occurred this time due to the effective water and mud transfer by the same pipe to the river Haine. This managed discharge initiated a rapid subsidence phase post-2018, with the subsidence rate peaking at -12.28 mm/year near F2 in the first half of 2018, the highest among all other piezometric vicinities. The subsidence rate then decelerated significantly in the latter half of 2018 and continued at a reduced pace until September 2021. Among the piezometric wells, the highest and lowest subsidence rates were observed near F1 and F4, at -2.97 and -1.29 mm/year, respectively. After September 2021, a new uplift phase started, observable across various parts of the region. This uplift, occurring around all piezometric wells, exhibits a consistent positive displacement rate estimated between 2.64 to 3.8 mm per year. Given the historical patterns described so far, it is reasonable to anticipate another significant event in the near future. The next section explores the relationship between deformation and piezometric wells, highlighting their interconnected dynamics.

4.5.3. Analysis of Piezometric Wells

Concerning the relationship between piezometric wells and incidents, several key insights were identified. The hydrogeological characterization of the Wealden terrain with a variable composition is critical for understanding the subsurface water dynamics and their influence on surface deformation. The installation of piezometers F1 to F5 after the 2009 incident and the subsequent monitoring of water table levels provided a direct insight into the aquifer response to external pressures and events. Piezometer F6 was also installed but for the purpose of monitoring the chalk aquifer. Notably, the water table levels show distinct trends and anomalies.

Table 4.2 shows the characteristics of piezometric wells installed in the region. A detailed time series visualization of water levels across six piezometric wells, with Wells F5 and F6 situated in the same location, is also provided (Figure 4.10). In the figure, the legend clarifies which data comes from which company or method, identifying the different sources of data collection. Visual examination of the fluctuation reveals not only unexpected events but also potential measurement issues. Initial data from F2 appear accurate, yet exhibit unusually high fluctuation rates, possibly due to installation issues with the piezometer. Rates exceeding 10 cm/h are unlikely to be natural, suggesting sensor malfunctions or external disturbances. F1 exhibited rapid water level rises in early October 2009, early March 2010, and early November 2010 (red vertical dashed lines in Figure 4.10). The first one aligns with a tracer test based on our knowledge, providing a clear explanation for this fluctuation. However, the origins of the subsequent increases in March and November 2010 are not as readily identifiable.

Table 4.2 Summary of SAR datasets used for analysis.

Well	Latitude	Longitude	Natural Ground Elevation (m)	Aquifer/Layers Monitored
F1	50.462492	4.167734	+90.97	Wealden terrains
F2	50.462606	4.167733	+93.38	Wealden terrains
F3	50.461011	4.169797	+90.35	Wealden terrains
F4	50.464950	4.169780	+105.65	Wealden terrains
F5	50.457987	4.170972	+77.25	Wealden terrains

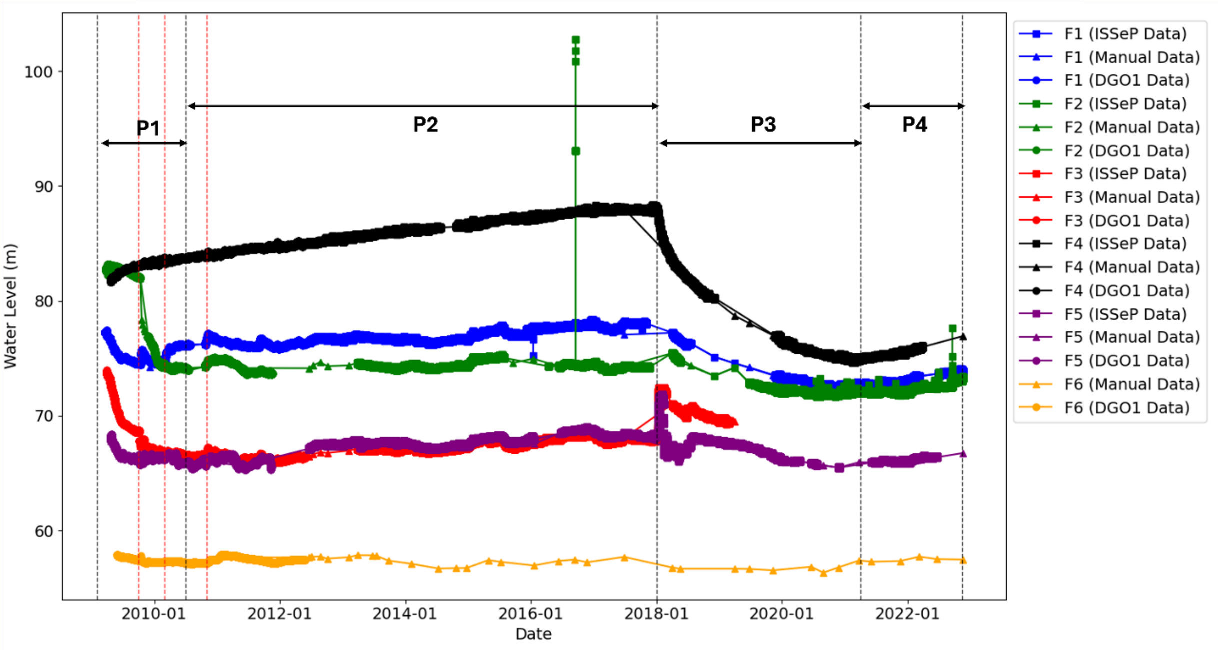

Figure 4.10 Time series of the 6 piezometric wells installed near the location of the mudflow outburst and the damages at the surface in the residential area of Saint-Vaast after the first event in 2009. The red dashed lines indicate rapid water level rises observed in F1 during early October 2009, early March 2010, and early November 2010.

The water table at F5 in the Wealden terrain stands roughly 10 meters above the chalk aquifer level at F6. With the lower sampling frequency of F6, yet it exhibited no significant fluctuations within the chalk aquifer throughout the entire observation period, suggesting that the chalk strata were probably not a contributing factor to the documented incidents. It makes sense as the chalk aquifer is separated from the Wealden aquifer by a thick aquiclude comprising the Cretaceous formations and the thickness of this aquifer is reduced on the hill of Saint-Vaast residential area compared to the southern area on the other side of the Haine river. Five piezometers, even F2, despite its considered lower reliability, exhibited remarkably consistent responses, indicating a coherent hydrogeological behaviour across the monitored area. Within this dataset, critical breakpoints are highlighted with vertical dashed black line marking key dates in the monitoring timeline. They are segmented into four distinct phases: beginning with the initial setup in 2009 after the first clog rupture event, leading into Phase 1 (P1) which continues until mid-2010. It is then followed by Phase 2 (P2) from mid-2010 to February 2018, Phase 3 (P3) from February 2018 to April 2021, and Phase 4 (P4), from April 2021, through to the end of our dataset in late 2022. To investigate the water level fluctuations, a more detailed analysis of the piezometric time series between these breakpoints is provided (Figure 4.11). Immediately after the 2009 incident, a substantial release of water and mud was observed, leading to a decline in water levels across all piezometers, except for F4, during Phase 1 (P1). F4 exhibited a gradual increase in water level at a rate of 1.58 m/year, different from the general pattern observed in the other wells. The negative water level trends observed in P1 across all wells except F4 transitioned in P2 to either stabilization, as seen in F2, or to recovery, with rising levels in F1, F3, and F5. The rising trend in F4 persisted during P2, at a reduced rate of 0.58 m/year. A strange observation was made towards the end of 2018. A sudden and pronounced rise in water levels in F3 and F5, accompanied by a sharp decline in F4, indicates an anomalous hydrogeological event or a potential shift in subsurface dynamics.

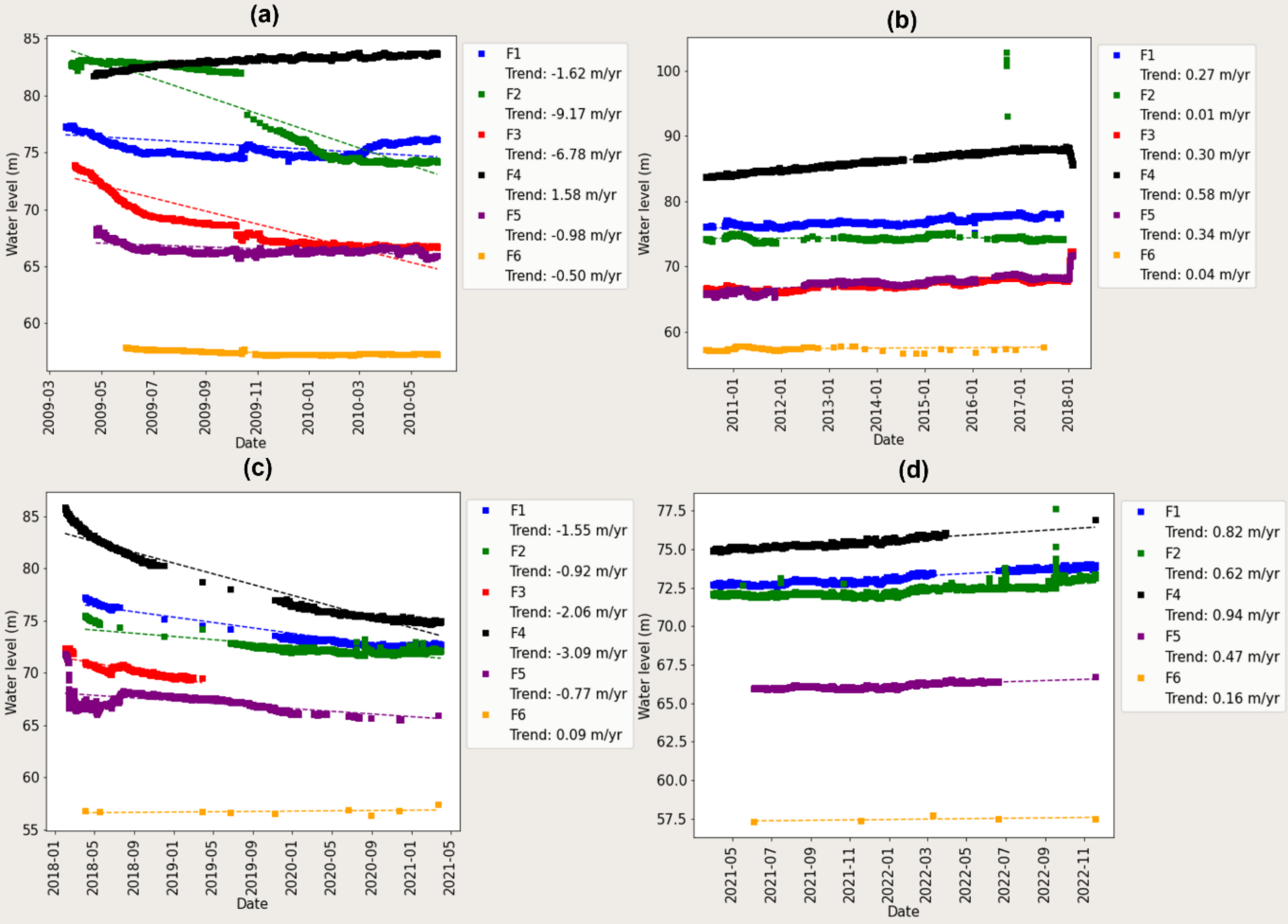

Figure 4.11 Water level evolution in piezometric wells installed near the incident site after the first event in 2009. The figure is segmented into four distinct phases: **a** initial setup to mid-2010 (P1), **b** mid-2010 to February 2018 (P2), **c** February 2018 to April 2021 (P3), and **d** April 2021 to late 2022 (P4), showing detailed fluctuations during these significant phases

The second incident coincided with this hydrological behaviour observed at the end of the P2 and beginning of the P3 phases. Initially, in early 2018, there was a sharp increase in water levels in F5 and F3, which suddenly transitioned to a decline, followed by a gradual decrease. A similar pattern was noted in F1 and F2, although data for the initial phase of the drop in F3 and F5 are missing for these wells due to irregular sampling during that time. F4 water level fell sharply, at a rate 3.09 m/year, yet showing a different steeper decline compared to the other wells, despite a similar downward trend. The different behaviour of F4, compared to F1, F3, and F5, despite all being situated within the Wealden terrains, could be explained by lateral variations in the geological composition of these sites. The Wealden terrains are generally characterized by sandy layers at shallower depths transitioning to clay materials with increasing depth, as observed in F1, F3, and F5. However, drillings at F2 and F4 have more clayey horizons closer to the surface (Fig. 4). This could explain F4 unique hydrogeological response, and the different water level trends observed. The clay layers, known for their lower permeability compared to sandy formations, could restrict water movement, thereby decoupling F4 water level responses from those observed in the more permeable, sandy environments of F1, F3, and F5. Another potential explanation could rely on the aspect of a lateral clog issue more to the northern part in the adit, implying that another clog was created after the 2009 event in between the positions of the F1-F2-F3 piezometers and the F4 piezometer. This other clog related to a collapse event inside the adit, might have initiated a change in the hydrogeological response to groundwater accumulation much further to the North of the adit implying already a pressure change leading to an uplift. If this scenario is correct, it might explain why the 2018 event is characterized by a strong water level decline in the F4 area while the F1-F2-F3 also follow the same pattern with a smaller amplitude. Nevertheless, the potential lateral location of the second clog associated with the 2018 event has not created damage to the surfaces in another part of the residential area of Saint-Vaast nor right at the surface of the 2009 event.

P4 marks a potentially new hazardous phase, characterized by a noticeable rise in water levels, signaling the risk of a new incident. This period, showing the start of an upward trend in water levels aligns with uplift estimations from the recent Sentinel-1A data. Essentially, the rising water levels, with limited outlets for relief, could escalate subsurface pressure, heightening the risk of further incidents.

4.6. Discussion & Conclusions

The events experienced in Saint-Vaast typically follow a pattern of progressive clogging, rupture, and subsequent surface deformation. However, rather than occurring at a fixed interval, the recurrence of these events is highly dependent on hydrological conditions, particularly infiltration rates. During periods of significant water infiltration, the confined aquifer system becomes pressurized, leading to uplift. When the water cannot escape due to clogging, pressure continues to build until rupture occurs, releasing water, mud, and transition of sediments out, which in turn initiates a subsidence phase. The duration of each phase—uplift, stability, and subsidence—can vary considerably, depending on local weather patterns and groundwater recharge rates. Since late 2021, the region has shown signs of uplift again, suggesting a potential recurrence of clogging events like those in the past. This poses a recurring geohazard issue in this densely populated urbanized area of Saint-Vaast that requests a detailed monitoring approach in the long term to follow up a post-mining hazard.

Piezometric analysis showed significant correlations between water level fluctuations in the Wealden aquifers and instances of ground deformation. The events of 2009 and 2018 highlight the region's vulnerability to hydrogeological hazards due to post-mining activities. The combination of piezometric well evolutions and PS-InSAR time series of deformation provides a comprehensive explanation for these events.

The temporal analysis identified critical breakpoints in displacement trends and piezometric well time series, offering insights into subsurface processes. These breakpoints align with observed hydrogeological events, indicating a direct link between subsurface water pressures and ground stability.

Starting from these considerations, a simple approach is here proposed to continue the monitoring of the whole area by combining the two techniques (i.e. piezometric wells and PS-InSAR data). The purpose of this approach is to give an overview of the collapse risk and clogging effect inside the abandoned mined adit considering how to tackle input data uncertainty. Frequently, in risk analysis a strong interference between uncertainty and decision-making is present and therefore it is crucial to generate an easy, accessible and transparent decision procedure capable of solving also complex problems characterized by poor local information. The case of Saint-Vaast is associated to the presence of an adit structure that has been mapped on old mine documents and to a long period of digging using many shafts to reach the level. The adit is potentially precisely located while the depth and the size (height and dimensions of the adit) are almost unknown. The lithology of the Wealden facies has been recently investigated through the 5 piezometric levels but only on a very limited depth implying a strong uncertainty in the presence, thickness and numbers of water-bearing sandy lenses inside the Wealden deposits through the entire thickness of the series but also in the lateral facies variations that might be very relevant for such kind of continental deposits. The depth of the adit and the dimensions do not allow visual inspections neither while it would be very suitable to have a clear view of the stability of the roof along the entire length of the adit. The 5 piezometers are also not very well distributed, and their number is insufficient to cover the entire adit. The unknow lithologies forming the roof of the adit are also creating large uncertainties in the places where mechanical instabilities might create roof collapses leading to clogging issues. Depending on the location of the potential future clog issue, the incident might be either almost not visible or generate again surface displacements. The management of post-mining hazards associated to such kind of features at shallow depth requires a combined monitoring system as the one used in this paper by two different technologies. It is potentially worth the time to check the other mapped adit features found in the area and associated with the Wealden deposits to determine whether other areas might also be influenced by similar surface displacements.

The analysis of land surface deformation in the Saint-Vaast region, Belgium, over three decades (1992-2023), using PS-InSAR techniques and correlating these findings with piezometric well data, has enhanced our understanding of the hydrogeological dynamics and associated geohazards of post-mining activities. This study highlights the relationship between subsurface water dynamics and resulting land deformation due to the presence of an old mining gallery.

The PS-InSAR time series analysis shows the temporal progression of ground displacement across three radar datasets. ERS data mainly (1992-2001) exhibit an uplift phase from 1992 until 1998, transitioning into stability from 1998 to 2001. Envisat observations (2003-2010) continue the uplift from 2003 to 2009, followed by stability in 2009-2010. Sentinel-1A data (2016 onwards) show an uplift phase from 2016 to 2018, a dramatic subsidence after 2018, and a reduced subsidence rate until 2021. From 2021, a new uplift phase is observed. Velocity maps align with the geological features of the Wealden terrains, emphasizing subsurface hydrogeological processes impact on ground deformation.

This investigation demonstrates the importance of integrated SAR and piezometric analyses in understanding and predicting geohazards in the post-mining region of Saint-Vaast. The dynamic interaction between geological structures, historical mining activities, and hydrogeological processes presents a complex but understandable pattern of ground deformation. This approach is crucial for early detection and mitigation of potential geohazards, safeguarding communities and infrastructures in this vulnerable post-mining region. Historical piezometric and PS-InSAR data show a clear correlation. Whenever there was an increase in the water level, an uplift was monitored. This is linked to sand and clay roof collapse in the gallery, leading progressively to a clog. Mudflow outbursts are associated with water floods and eventually cause subsidence.

5

Performance Assessment of Corner Reflectors

5.1. Introduction

The integration of multiple geodetic observation techniques has become increasingly essential for precise and accurate monitoring of the Earth's surface deformation. One innovative approach in this domain is the use of Integrated Geodetic Reference Stations (IGRS), which combine various measurement technologies including Global Navigation Satellite Systems (GNSS), Interferometric Synthetic Aperture Radar (InSAR), leveling, and others.

This chapter focuses on assessing the performance of corner reflectors within the IGRS framework installed at Doel. The need for IGRS becomes particularly evident when addressing the challenges encountered in previous chapters regarding the selection of a stable reference point for PS-InSAR processing. As discussed, comparing data from different satellite missions (e.g., ERS, Envisat, Sentinel-1) introduces significant uncertainties and potential bias due to differences in reference points. These biases can lead to misinterpretations of subsidence or uplift trends across missions. An IGRS provides a consistent, stable reference to minimize these uncertainties, significantly reduce bias, and ensure more reliable comparisons across satellite datasets. Moreover, the implementation of IGRS is not only crucial for current satellite missions but also for future missions that may come online. As new satellites with varying orbital parameters, sensor technologies, and resolutions are launched, the IGRS will serve as a standardized reference point, enabling integration and comparison of InSAR data from different sources. This will enhance the long-term monitoring of deformation and ensure continuity in data quality, making the IGRS an indispensable tool for future geodetic research. Evaluating these corner reflectors is critical for enhancing the accuracy and reliability of geodetic measurements, thereby contributing to a more accurate measuring of land surface deformation.

Artificial radar reflectors, such as corner reflectors, play a significant role in geodetic applications, particularly in enhancing the precision of InSAR measurements. Theirprimary purpose is to provide a stable, well-defined reference point for detecting motion in the context of surface deformation studies. These reflectors are used to tie the InSAR data to a known position, which can be continuously monitored using GNSS. The integration of GNSS measurements ensures that any motion of the corner reflector reference point is accurately tracked over time, providing a precise and stable basis for assessing land surface deformation. Additionally, they serve in InSAR datum connection and geodetic integration. Initially, SAR observations are positioned in a 2D radar datum (azimuth and range), which can be transformed into a Cartesian geocentric terrestrial reference frame using the range-Doppler equations and an external elevation model.

The IGRS concept addresses the challenge of integrating multiple geodetic techniques by providing co-located reference points. This ensures that observations from different methods represent the same physical processes. GNSS, for example, provides 3D spatial positioning through satellite signals, while InSAR monitors deformation by analyzing differences in radar signal phases between two images. By integrating these methods, IGRS facilitates the translation of InSAR measurements into a consistent geodetic datum (Kamphuis 2019).

The main goal of IGRS is to integrate GNSS and InSAR data to ensure that time series represent consistent deformation characteristics. This integration is crucial for accurately interpreting measurements from various sensors and monitoring methodologies. The known location of the IGRS in a global coordinate reference system allows for calibrated deformation time series and improved geolocation estimates for InSAR scatterers.

In the following chapter, it aims to develop and evaluate the performance of IGRS corner reflectors installed in Doel, Belgium. The objectives include establishing a standard procedure for analyzing the SAR time series of artificial radar reflectors to estimate their Radar Cross Section (RCS), Signal-to-Clutter Ratio (SCR), and time series of range and azimuth movements. The goal is to implement this procedure using an efficient, open-source toolbox called GECORIS.

5.2. Theoretical Background

The performance of corner reflectors is crucial for accurate SAR positioning. Unlike transponders, passive corner reflectors are simpler to manufacture due to the absence of electronic components. However, their design and installation require careful consideration of various factors such as application requirements, weather conditions, materials used, background noise at the installation site, and the satellite's signal wavelength and orbit geometry. For a corner reflector to be effective, its reflected signal must be distinguishable in the SAR image, meaning the backscattered signal must be stronger than the surrounding background noise, known as clutter. The SCR quantifies this relationship. High SCR values are essential as they directly impact the accuracy of LOS measurements. For instance, a high SCR ensures that the phase variations caused by nearby scatterers do not significantly affect the measured phase of the dominant scatterer, thus reducing errors in point target measurements.

Extensive research and development efforts have focused on optimizing corner reflector designs for geodetic applications. Various types, including triangular and square trihedral reflectors, have been tested for their backscattering performance and robustness under different weather conditions. These tests aim to identify the most effective and durable designs.

These reflectors have been tested in diverse field conditions and orientations to ensure their effectiveness. For instance, corner reflectors have been evaluated for their performance in both ascending and descending satellite tracks. Following successful testing, these reflectors have been permanently installed at strategic locations to enhance geodetic measurements. The choice of reflector design, including the use of thicker aluminum plates and protective covers, ensures consistent performance in various environmental conditions.

The integration of these theoretical and practical considerations into the design and deployment of corner reflectors directly influences the accuracy of SAR positioning. To further understand and optimize this process, it is essential to delve into the mathematical formulations that govern SAR measurements, SCR, and RCS.

SAR measurements can be represented by the Impulse Response Function (IRF), which is crucial in determining the resolution cell on the Earth’s surface. This IRF is typically modeled as a 2D sinc-like function in both azimuth and range directions. For a corner reflector, the signal observed in the SAR image is a combination of its dominant point scattering and the contributions from surrounding scatterers, or clutter. The power of the signal y captured by SAR can be expressed as:

$$y = Aexp(i\psi) \tag{40}$$

where A represents the amplitude, and ψ is the phase. The power P or intensity I of this signal is then:

$$P = A^2 = \Re(y)^2 + \Im(y)^2 \qquad (41)$$

where $\Re(y)$ and $\Im(y)$ are the real part and imaginary part of the complex signal y.

For distributed scatterers, the radar brightness β^0 is a useful measure. It provides a normalized value that accounts for the strength of the radar signal as a function of the resolution cell area particularly in the slant-range direction. Radar brightness is derived from the pixel values (Digital Numbers, DN) recorded in the SAR image and is given by:

$$\beta^0 = \frac{DN^2}{K_{DN}^2 K} \qquad (42)$$

This expression includes both a pixel scaling factor K_{DN} and calibration constant K. These factors are used to properly scale the digital number DN values and convert them into a standardized radiometric measure.

For idealized point scatterers like corner reflectors, RCS is a critical parameter. It measures how much power is reflected to the radar from a target and is expressed in square meters. The RCS can be estimated using two primary methods: the integral estimation method and the peak estimation method. In the *integral* estimation method:

$$RCS \approx \frac{I_P}{K}\frac{P_A}{C_F} \qquad (43)$$

In this equation, I_P is the integrated power within the main lobe of the radar signal response, P_A is the pixel area in the SAR image, and C_F is accounting for the relative power in the sidelobes. In the *Peak* estimation method:

$$RCS \approx \beta^0 \Delta_{az} \Delta_r \qquad (44)$$

In this equation, Δ_{az} and Δ_r are the azimuth and range resolution respectively.

SCR is another key parameter, which is determined by the ratio of the reflector's signal power to the power of the surrounding clutter within the resolution cell. Mathematically, it is expressed as:

$$SCR_{CR} = \frac{I'_{CR,peak}}{\bar{I}_{clutter}} \approx \frac{RCS_{CR}}{\bar{\beta}^0{}_{clutter} \Delta_{az} \Delta_r} \qquad (45)$$

In this equation, $I'_{CR,peak}$ is the highest intensity of reflector, corrected for the clutter, $\bar{I}_{clutter}$ the expected intensity of the clutter, and $\bar{\beta}^0{}_{clutter}$ multiplied by the resolution cell area is the expected radar brightness of the clutter. The SCR directly impacts the accuracy of the LOS measurements, as it influences the phase variance σ_ϕ which in turn affects the standard deviation of the LOS displacement $\sigma_{d_{LOS}}$. The phase variance can be approximated by:

$$\sigma_\phi \approx \sqrt{\frac{2}{2SCR - \sqrt{3}/\pi}} \qquad (46)$$

and the corresponding standard deviation of LOS displacement is given by:

$$\sigma_{d_{LOS}} = \frac{\lambda}{4\pi}\sigma_\phi \qquad (47)$$

where λ is the wavelength of the radar signal (Czikhardt et al. 2021).

The careful consideration of corner reflector design is essential for achieving high SCR and RCS values, which directly influence the accuracy and reliability of InSAR measurements. As noted, the RCS depends heavily on the physical characteristics of the corner reflector, including its size, shape, and material. For instance, the theoretical RCS for a square trihedral reflector with an inner leg length of 0.7 meters is approximately 34.7 dBm^2, whereas a triangular trihedral reflector of the same size typically achieves a lower RCS of around 25.1 dBm^2 (Figure 5.1). These values, however, can vary in practice due to factors such as orientation errors and environmental conditions. The impact of RCS on SAR positioning is visually evident in Figure 5.1, which shows how RCS varies with the inner leg size of different types of corner reflectors. This figure underscores the importance of selecting a reflector with an optimal design to maximize the reflected signal's strength and improve measurement accuracy.

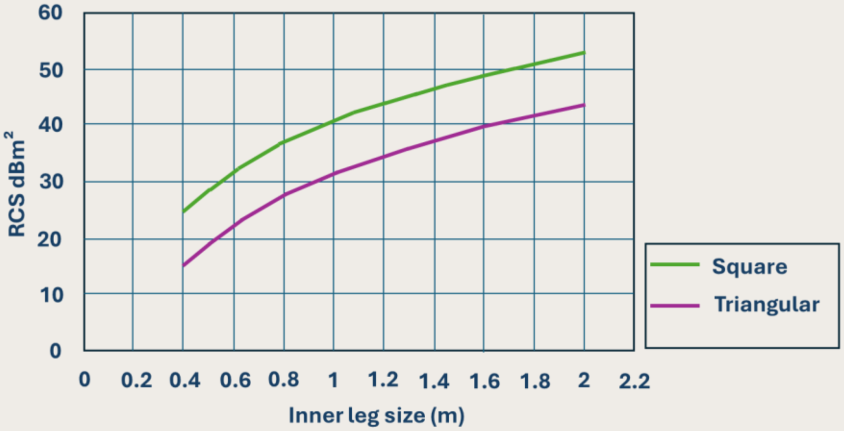

Figure 5.1 Relationship between Radar Cross Section (RCS) and inner leg length for C-band (Sentinel-1) trihedral corner reflectors, comparing triangular and square designs. The inset illustrates the geometric shapes of the reflectors. Adapted from (Garthwaite et al. 2015).

The design and installation process of corner reflectors also involves selecting appropriate materials and ensuring that the reflectors are oriented correctly relative to the satellite's line of sight. For example, using thicker aluminum plates and protective covers can help maintain consistent performance, even in adverse weather conditions.

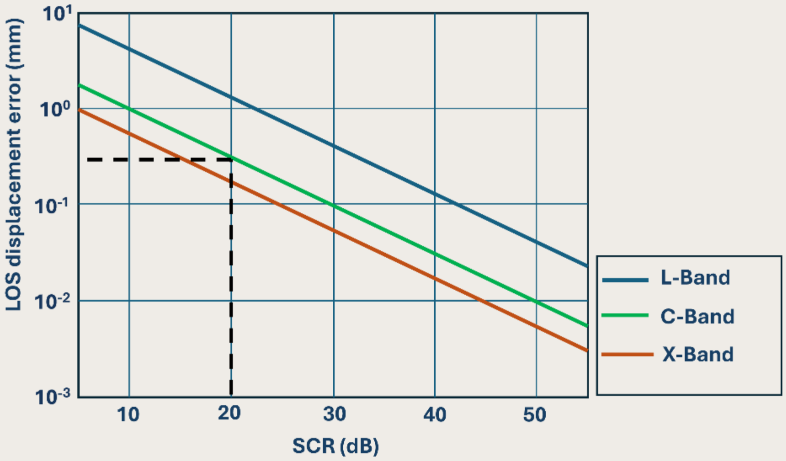

Figure 5.2 LOS displacement error as a function of Signal-to-Clutter Ratio (SCR) for L/C/X-Band InSAR data. Adapted from (Garthwaite 2017).

As discussed, the relationship between SCR and LOS measurement precision is critical. As illustrated in Figure 5.2, an SCR of 20 dB can lead to a LOS displacement error as small as 0.5 mm in C-band InSAR measurements. This precision is essential for high-accuracy geodetic applications.

These considerations highlight the necessity of optimizing both the design and deployment of corner reflectors to enhance the accuracy of geodetic measurements. The inclusion of Figures 5.1 and 5.2 not only provides a visual representation of these critical relationships but also reinforces the importance of SCR and RCS in achieving precise SAR positioning, thus making them indispensable tools for understanding and improving corner reflector performance in practical applications.

5.3. IGRS Installation in Doel

The installation of IGRS corner reflectors at the Doel site was a meticulously planned process, taking into account several critical factors to ensure optimal performance for InSAR measurements. One of the primary considerations was the location of the site, which needed to be carefully selected to balance accessibility with the technical requirements for accurate geodetic measurements. The Doel site, located within the protected area of the Doel nuclear plant in Belgium (location shown in Figure 5.3), was chosen based on its suitability for long-term monitoring and its minimal exposure to environmental and urban interference.

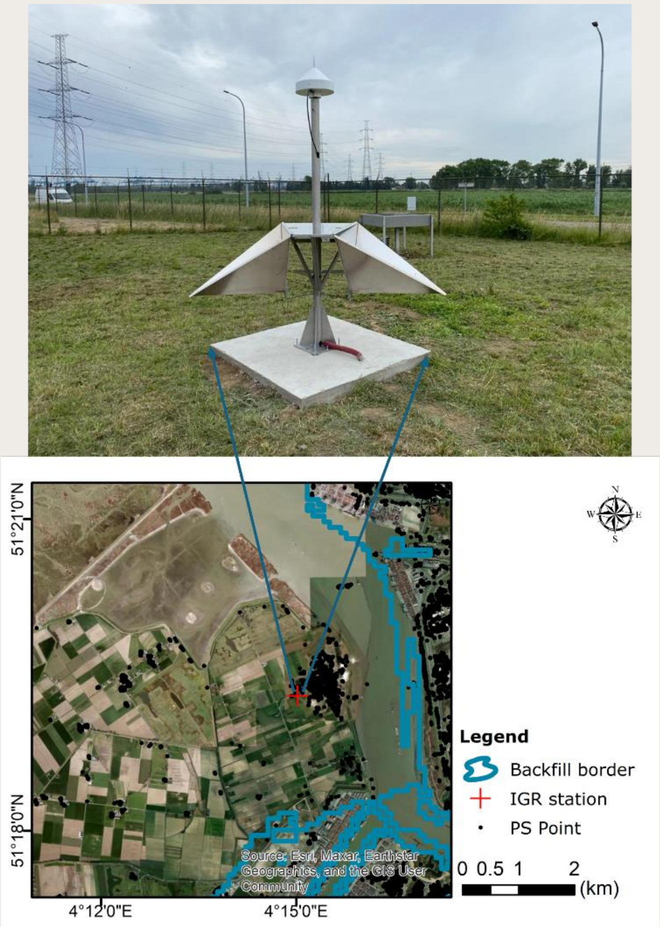

Source: Esri, Maxar, Earthstar Geographics, and the GIS User Community

Figure 5.3 Location of the IGRS corner reflector installation site within the protected area of the Doel nuclear plant in Belgium

Additionally, the site’s proximity to essential utilities, such as electricity and internet, was crucial to support the continuous operation and data transmission required for the monitoring activities.

Key factors considered during the installation included sky visibility, accessibility, and the specific application requirements for geodetic infrastructure monitoring. Ensuring unobstructed visibility toward the satellites was crucial for maximizing the effectiveness of the corner reflectors. The orientation of the reflectors was carefully calculated based on the azimuth and elevation angles relative to the known satellite orbits, such as those of Sentinel-1. This precise alignment was necessary to ensure that the reflectors would capture and return the satellite signals without obstruction, thereby providing accurate data for InSAR analysis.

In addition to these technical considerations, the installation process also took into account the potential for signal interference and clutter. A thorough SCR analysis was performed before installation to identify the best possible location for the reflectors within the site. This analysis ensured that the chosen location would minimize background noise and maximize the accuracy of the radar signal measurements. The SCR analysis at Doel was particularly important given the potential for interference from nearby structures or vegetation, which could affect the accuracy of the InSAR data.

On 22 July 2022, the first IGRS in Belgium was installed at the Doel site. This marked the beginning of the station's capability to support high-precision InSAR measurements. After the initial installation, further refinements were made to optimize the reflector's performance. On 15 May 2023, the reflector was adjusted to achieve an optimal inclination, ensuring it was correctly aligned to receive the maximum Radar Cross Section (RCS). This adjustment was crucial for enhancing the accuracy and reliability of the reflected signals, thereby improving the overall effectiveness of the InSAR measurements conducted at the site.

The GNSS station DOEL00BEL at Doel, Belgium, is a well-established site managed by the National Geographic Institute of Belgium. The IGRS in Doel is approximately located at 51.3218°N latitude and 4.2500°E longitude with an elevation of 45 meters. The station is built on a concrete slab foundation with a depth of 1.3 meters, a thickness of 55 cm, and approximate dimensions of 1 m^2 (with minor variations). Approximately 5 cm of the concrete slab is visible above the grass level. It features a SEPT POLARX5E receiver supporting GPS, GLONASS, and Galileo satellite systems. The single vertical pole monument stands 2.4 meters tall, anchored on a concrete foundation. The concrete slab rests directly on Quaternary sediments without deeper vertical steel poles; instead, four horizontal steel rods were embedded near the base of the slab, extending 30 cm into the surrounding Quaternary sediments and 30 cm into the concrete. This was done to stabilize and lightly anchor the foundation. The station uses a SEPCHOKE_B3E6 antenna with an SPKE radome, connected by a 30-meter coaxial cable and aligned 10 degrees from the true north. The foundation sits on a combination of sand, clay, and peat layers, which are on sedimentary bedrock. on sedimentary bedrock within the Eurasian tectonic plate, ensuring stable and precise geodetic measurements for regional monitoring. (For further details about the DOEL00BEL GNSS station, including technical specifications and comprehensive site information, readers can visit the official GNSS metadata website).

To complement the installation at the Doel site, ongoing maintenance and monitoring procedures were established. Regular checks are conducted to ensure that the reflectors remain properly aligned and free from obstructions, such as debris or vegetation growth, which could degrade the quality of the reflected signals. This proactive approach helps to maintain the high SCR and RCS values necessary for precise InSAR measurements, ensuring that the Doel IGRS continues to provide valuable data for geodetic and environmental monitoring.

5.4. Results

The processing of this chapter was done using the GECORIS open-source Python toolbox. In this analysis, SAR data from tracks ascending 88 and 161 and descending 37 and 110 were used to assess the positioning accuracy of corner reflectors under varying correction factors. Table 5.1 summarizes the RCS values, acquisition periods, and characteristics of used data for each track:

Table 5.1 Summary of RCS values, acquisition time, and periods for different SAR tracks, covering both pre- and post-installation periods.

Track	Geometry	Average RCS before CR installation (dBm^2)	Average RCS after CR installation (dBm^2)	Acquisition period	Acquisition time
110	Descending	9.84	28.8	04/01/2022-28/07/2024	05:58:57-05:59:12
37	Descending	5.21	28.6	11/01/2022-23/07/2024	05:50:47-05:51:03
161	Ascending	5.93	28.8	07/01/2022-25/06/2024	17:33:26-17:33-41
88	Ascending	14.16	28.4	02/01/2022-26/07/2024	17:25:16-17:25:32

The Absolute Positioning Errors (APE) in both range and azimuth are calculated as the difference between the detected subpixel peak positions and the expected radar coordinates, taking into account various timing biases. These biases include contributions from the ITRF position, solid earth tides (SET), tropospheric (tropo) and ionospheric (iono) delays, bistatic correction, Doppler effects, and FM-rate mismatches. For the Doel IGRS corner reflector, calculations were performed on a triangular corner reflector.

The impact of individual SAR positioning corrections was analyzed for ascending and descending tracks, as represented in Figure 5.4. Each scatter point in Figures 5.4a-d corresponds to a single Sentinel-1 acquisition, with each graph representing data from a different track (ascending 88, ascending 161, descending 37, and descending 110). These points illustrate how the application of various SAR positioning corrections progressively refines the accuracy, as shown by the clustering of points closer to the origin.

The analysis of range and azimuth errors across four Sentinel-1 tracks reveals distinct patterns in positioning accuracy. Ascending tracks (88, 161) show more initial scatter than descending tracks (37, 110).

However, all tracks benefit from corrections, with descending tracks generally showing tighter clustering after corrections. Across all tracks, FM-rate and Doppler corrections show the most substantial improvement in clustering, particularly in range.

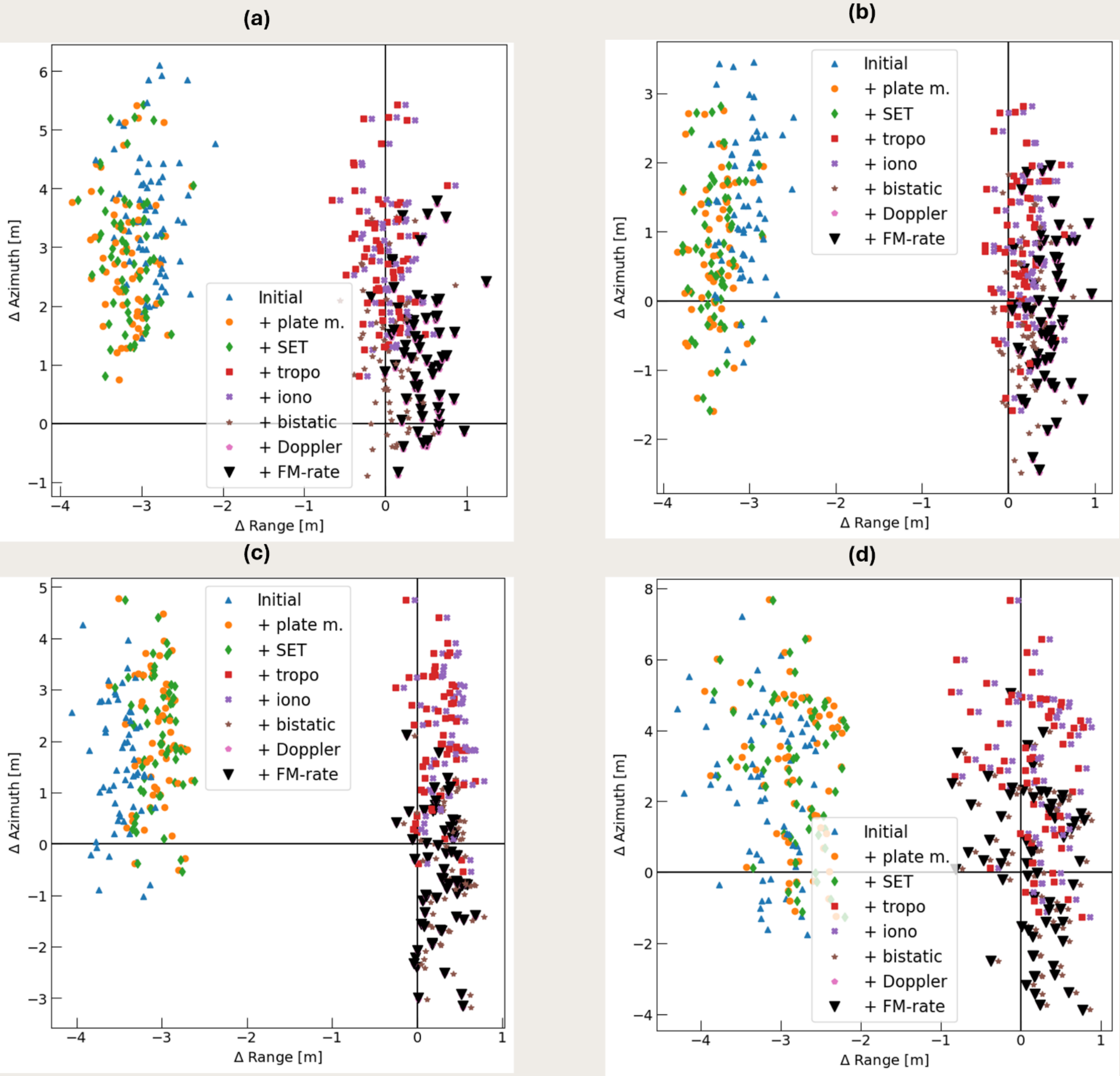

Figure 5.4 Impact of Individual SAR Positioning Corrections on Absolute Positioning Errors (APE) in Range and Azimuth for the Doel IGRS Corner Reflector. Stack of data from **a** Track 110 (Descending), **b** Track 37 (Descending), **c** Track 161 (Ascending), and **d** Track 88 (Ascending). Each scatter point represents a single Sentinel-1 acquisition, with different colors and markers indicating the various corrections applied, such as plate motion, SET, tropo, iono, bistatic, Doppler, and FM-rate.

The time series graphs in Figure 5.5 illustrate the range and azimuth errors for the four SAR tracks over time, with each colored marker representing a different track: blue triangles for ascending 88, green diamonds for ascending 161, orange circles for descending 37, and red squares for descending 110. The horizontal lines in each plot indicate the mean error for the corresponding dataset, serving as a baseline for comparison and highlighting each track's overall positioning accuracy. In the range plot, most tracks fluctuate around their mean lines, but ascending track 88 shows more variability, with some points below the mean, suggesting occasional deviations in range accuracy. Additionally, ascending track 88 shows the highest variability in azimuth positioning, indicated by the largest standard deviation (2.13 m) among the others. Descending track 37 demonstrates the most stability with minimal variation in both range and azimuth (0.19 and 1.01 m respectively).

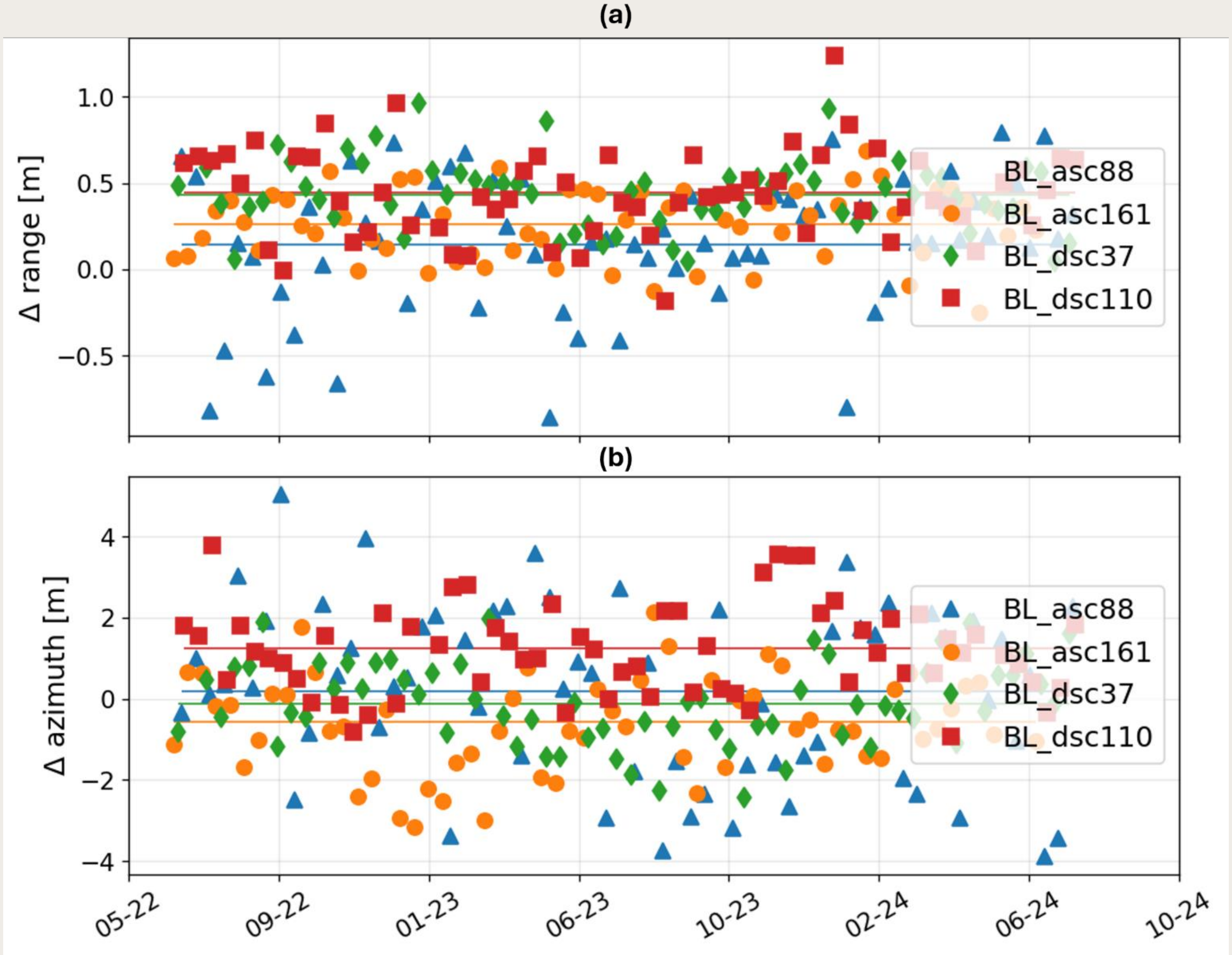

Figure 5.5 Time series of positioning errors for comparison of **a** range errors **b** azimuth errors, across different tracks.

Figure 5.6 shows the RCS time series for the Doel IGRS corner reflector apparent for four different Sentinel tracks. The SCR of each is calculated and written on the graph. These parameters are key factors that illustrate the performance of corner reflectors. The plotted data reveals how the reflectivity of corner reflectors varies over time. The dashed vertical line indicates the installation and alignment date of the reflector. Before the installation of the corner reflector, the observed RCS was dominated by clutter, as seen in the lower apparent RCS values. After installation, the RCS significantly increased, indicating the impact of the corner reflector on signal strength. The horizontal lines show the average RCS for each track before and after installation.

The SCR values in Figure 5.6 indicate that the descending tracks (Tracks 37 and 110) generally have higher SCRs—19.7 dB and 19.1 dB, respectively—compared to the ascending tracks (Tracks 88 and 161), which have SCRs of 16.5 dB and 16.1 dB. This suggests that the descending tracks experience less background noise, allowing for clearer detection of the corner reflector signal.

Conversely, the clutter RCS is higher for ascending tracks, indicating that these tracks encounter more background reflections, which could be due to their specific geometric configuration or environmental conditions. This higher clutter RCS may contribute to the lower SCR in the ascending tracks, making the signal less distinct against the background.

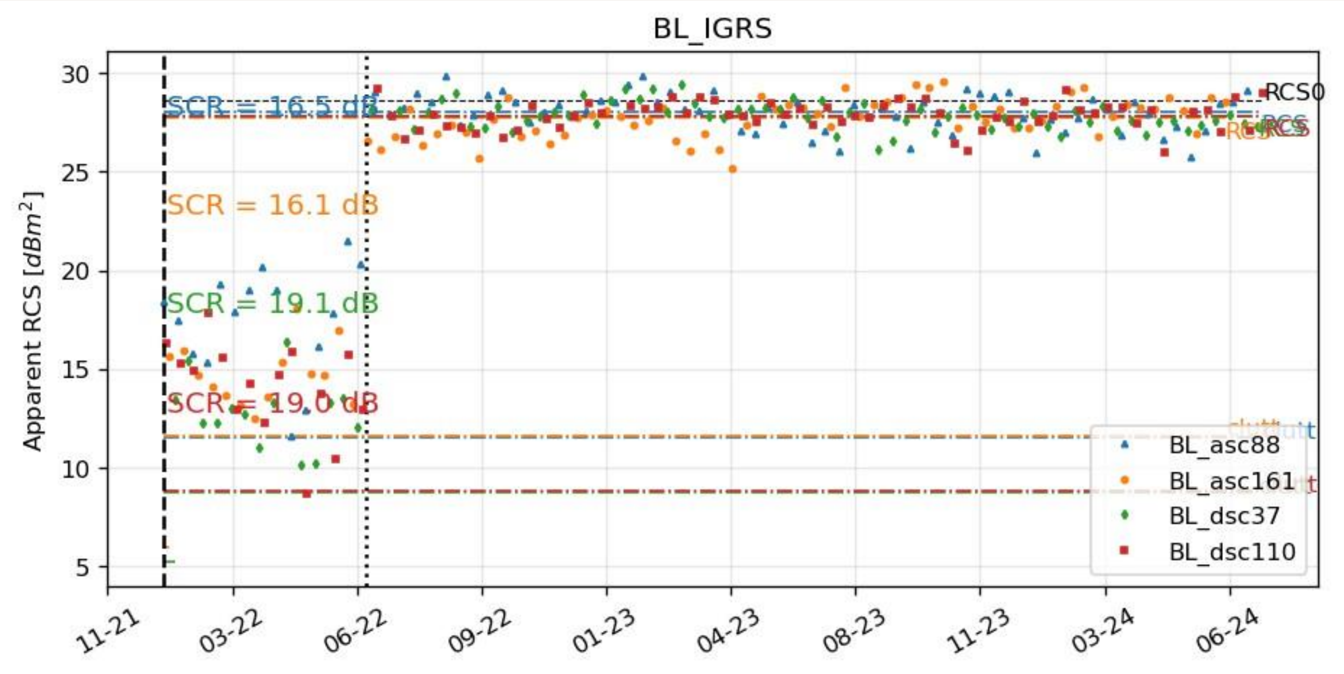

Figure 5.6 Apparent RCS time series of the Doel IGRS corner reflector for four different Sentinel-1 track

For the Doel IGRS corner reflector, the radar brightness (Beta0) before and after installation was evaluated for all four tracks. Figure 5.7 shows two examples, one from ascending track 161 (Figure 5.7a) and the other one from descending track 37 (Figure 5.7b). These are the result of smoothed data and the oversampling of the radar brightness, which is conducted with a factor of 32.

Figure 5.7 reflects the radar brightness before and after the installation of the corner reflector on the specified dates (07/01/2022 for track 161 and 11/1/2022 for track 37 for before installation, and 07/06/2023 for track 161 and 29/07/2023 for track 37 for after installation).

Beta0, or radar brightness, is typically calculated for each SAR acquisition. It represents the radar reflectivity of the surface for a specific acquisition, reflecting the power of the radar signal returned to the satellite after interacting with the ground. By analyzing Beta0 across multiple acquisitions, changes in reflectivity over time could be assessed, which can be useful for monitoring surface changes or selecting a master image for interferometric analysis based on the highest Beta0 values, ensuring the best signal quality for further processing.

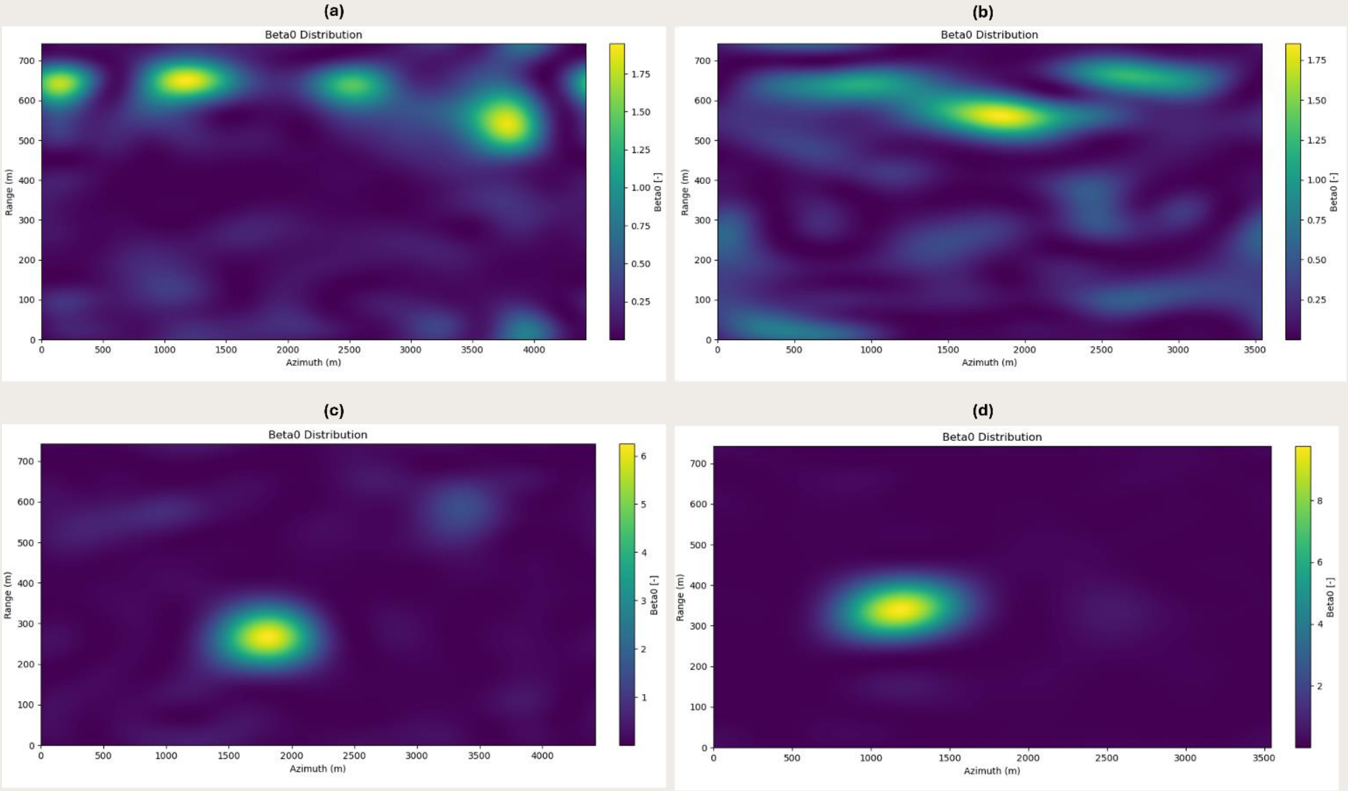

. **Figure 5.7** Radar brightness in azimuth and range geometry for **a** before installation for descending track 37 (11/01/2022), **b** before installation for ascending track 161 (07/01/2022), **c** after installation for descending track 37 (29/07/2023) and **d** after installation for ascending track 161 (07/06/2023).

Figure 5.8 presents cross-sectional views of the radar brightness (Beta0) at its peak value before and after the installation of the corner reflector. The cross-sections were taken along both azimuth and range directions for descending track 37 and ascending track 161, corresponding to Figure 5.7 specifically.

Figure 5.8a shows the azimuth and range cross-section for track 37 before the installation of the corner reflector, while Figure 5.8b presents the same cross-section for track 161 before installation. Figure 5.8c illustrates the azimuth and range cross-section for track 37 after installation, and Figure 5.8d displays the cross-section for track 161 after installation.

Before the installation of the corner reflector, the radar brightness (Beta0) profiles in both azimuth and range directions lacked a distinct peak, meaning the reflected signal was weak and dispersed. This makes it challenging to accurately pinpoint the position of the reflector, which is crucial for precise geolocation and positioning tasks.

After installation, the reflector creates a strong, sharp peak in the Beta0 profile, significantly improving the clarity and accuracy of the reflected signal. This sharp peak is essential for reliable positioning, as it ensures the reflector's location is easily identifiable in the radar data.

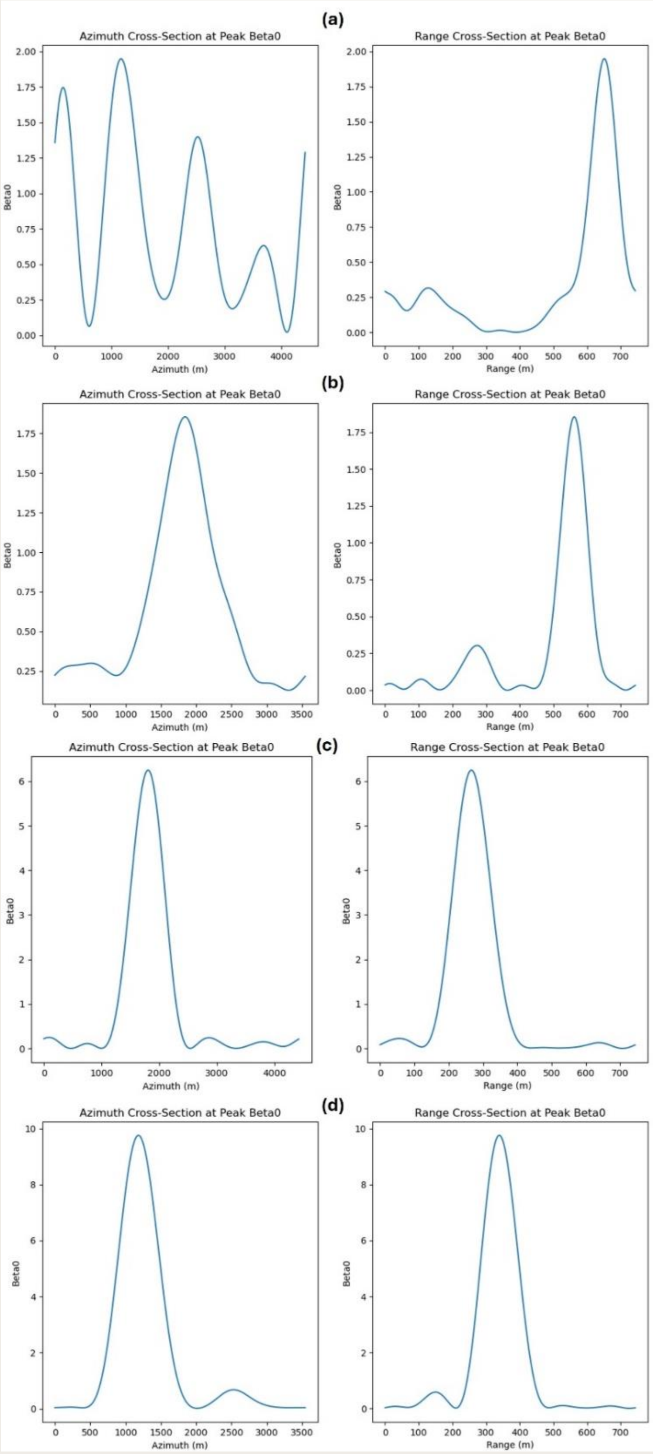

Figure 5.8 Azimuth and range cross-sections of Beta0 for **a** track 37 before installation of CR, **b** track 161 before installation of CR, **c** track 37 after installation of CR, and **d** track 161 after installation of CR.

Additionally, the relationship between SCR and phase noise is investigated. Table 5.2 summarizes values of SCR, standard deviation of phase, and displacement precision for four different tracks.

Table 5.2 Values of SCR, standard deviation of phase, and displacement precision for four different satellite paths

Path	SCR (dB)	Standard deviation of phase (degrees)	Displacement precision (mm)
Ascending 88	16.5	6.1	0.5
Ascending 161	16.1	6.4	0.5
Descending 37	19.1	4.5	0.3
Descending 110	19.0	4.5	0.4

The results demonstrate a clear relationship between SCR, phase noise, and displacement precision across the different SAR paths analyzed. As expected, paths with higher SCR values exhibit lower phase noise, leading to improved displacement precision. For example, the descending path 37, with the highest SCR of 19.1 dB, shows a phase standard deviation of only 4.5 degrees, resulting in a displacement precision of 0.349 mm. In contrast, the ascending path 161, which has a lower SCR of 16.1 dB, exhibits a higher phase standard deviation of 6.4 degrees and a corresponding reduction in displacement precision to 0.496 mm. This inverse relationship highlights how stronger SCR ratios lead to more reliable and accurate surface displacement estimates, as phase noise diminishes with increased SCR.

5.5. Discussions

The chapter presented a comprehensive analysis of the integration and performance evaluation of IGRS in Doel, focusing on the use of corner reflectors for InSAR applications. The key objective was to assess how corner reflectors enhance the accuracy of surface deformation monitoring through improved radar signal reflectivity, as indicated by RCS and SCR.

The results demonstrate the effectiveness of the corner reflectors in improving the quality of SAR data. The analysis of the RCS time series before and after the installation revealed a significant increase in signal strength, reflecting the impact of the corner reflectors on the radar measurements. This enhancement is crucial for precise geodetic measurements, as the corner reflectors provide a consistent, strong return signal, which is essential for accurate InSAR analysis.

The Beta0 analysis before and after the installation provided further insights into the reflectivity changes induced by the corner reflectors. The radar brightness maps illustrate the substantial increase in radar brightness after the installation, confirming the improved signal quality. This increase is particularly evident in the all track's data, which showed a notable rise in both RCS and Beta0 values, indicating a more robust and reliable signal post-installation.

The discussion also highlighted the role of SCR in performance evaluation. The higher SCR values observed in descending tracks compared to ascending ones suggest that these tracks experience less background noise, leading to clearer and more accurate detection of the corner reflector signal. This finding highlights the importance of considering track geometry and environmental factors when deploying corner reflectors for geodetic purposes.

The results clearly show that higher SCR values lead to reduced phase noise, which in turn improves displacement precision. This finding highlights the potential benefits of having an IGRS available in areas such as Antwerp and Saint-Vaast. If an IGRS had been available from the beginning of periods of different satellite missions in the Antwerp and Sint-Vaast cases, it could have provided a stable, high-SCR reference point, reducing the uncertainty associated with phase noise and enhancing the overall precision of displacement measurements.

Additionally, by anchoring the relative InSAR measurements to a consistent, well-defined geodetic reference frame, the integration of GNSS data would have provided independent verification of reference point stability. In both case studies, the lack of a stable, known reference point meant that displacement measurements could be biased due to reference point motion. Using IGRS would have minimized the potential bias in displacement measurements due to reference point motion.

Overall, the study emphasizes the role of corner reflectors in enhancing the accuracy of InSAR measurements within the IGRS framework. The significant improvements in RCS, Beta0, and SCR post-installation reflect the successful integration of these reflectors into the geodetic monitoring system, providing valuable data for precise surface deformation analysis.

This is a crucial step for the future integration and comparison of time series of LOS measurements, converted to vertical and horizontal displacements, with data from GNSS, ensuring comprehensive and accurate monitoring.

6

Conclusion and Perspectives

6.1. Conclusion

The dissertation provides an extensive investigation into land deformation and associated hydrogeological hazards in Belgium, focusing on the regions of Antwerp and Saint-Vaast. Through a combination of PS-InSAR analysis of SAR data, piezometric well monitoring, and numerical modeling, the research explains the intricate dynamics of ground deformation in these two regions.

The study of land subsidence in Antwerp employed a temporal analysis of surface displacements, using high-resolution TerraSAR-X data from 2019 to 2022, along with mid-resolution historical data from ERS1/2, ENVISAT ASAR, and Sentinel-1A radar datasets spanning 1992–2001, 2003–2010, and 2016–2023 respectively. This multi temporal space-based monitoring technique provided detailed insights into the spatial extent and magnitude of deformation over more than three decades.

The observations revealed a persistent trend of land subsidence, particularly pronounced in the harbor area. The subsidence rates differed significantly between the zones of Antwerp harbor and Antwerp city center, highlighting the influence of varying geological and hydrological conditions. The subsidence at the local model, situated outside the backfill area, was analyzed using a 3D groundwater flow model coupled with a 1D geomechanical model. This location outside the backfill zone was chosen to focus the analysis on the deformation due to the role of hydrological processes, excluding the effects of the compaction due to the presence of backfill material and load changes associated with that in the harbor. This approach allowed for a clearer understanding of subsidence driven by groundwater dynamics and sediment consolidation in the areas which is not subject to the presence of backfill.

This modeling approach enabled the simulation of swelling and compaction resulting from changes in water pressure across various aquifers. Notably, significant declines in water heads in the Ruisbroek-Berg Aquifer and the Lower Oligocene Aquifer System led to substantial compaction, while rising water heads in the Wemmel-Lede Aquifer resulted in swelling, which partially compensated the overall land subsidence.

A significant aspect of the study was the comparison of deformation rates calculated from the numerical model with those estimated by PS-InSAR. The rates of deformation derived from the PS-InSAR data provided a high-resolution temporal and spatial understanding of ground movement, while the numerical model offered insights into the mechanisms driving these deformations in the sublayers. The similarity in trends observed from both methods validated the model accuracy in capturing the subsurface processes. Notably, the deformation rates obtained from SkyGeo, EGMS (both using Sentinel data), and TerraSAR-X processed in this study were similar and aligned well with the model results, as they covered almost the same period. However, there were discrepancies when comparing the rates from Sentinel data processed in this study with those from SkyGeo, EGMS, and TerraSAR-X. Despite these differences, the fact that the results are comparable is already a significant achievement, considering the inherent limitations of both methods. This indicates a consistent pattern of subsidence across different data sources and underscores the robustness of the integrated approach. The PS-InSAR provided a more immediate response to surface changes, whereas the model could sometimes lag due to the simplifications and assumptions made about the subsurface properties and processes. However, with the strategic sub-layering in our modeling, which implicitly accounted for potential delays, this issue was effectively mitigated, ensuring a coherent understanding of deformation dynamics.

Despite the robust modeling framework, the study faced several challenges related to data scarcity. The limited availability of detailed hydrogeological and geomechanical parameters posed significant hurdles in achieving accurate deformation simulation. Furthermore, the temporal gaps in the PS-InSAR data and the lack of continuous piezometric measurements and reliable pumping data complicated the comparison of the computed deformation by the model and estimated by the PS-InSAR. These limitations highlight the necessity for continuous and high-quality data collection to enhance the reliability of subsidence assessments. The research emphasizes the importance of integrated monitoring approaches that combine satellite-based measurements with in-situ data to provide a comprehensive understanding of subsurface dynamics. Such integration is crucial for accurately assessing and computing ground deformation in complex geological settings.

In conclusion, the study of land subsidence in Antwerp shows the important role of advanced geodetic and hydrogeological monitoring in studying subsidence drivers. The findings demonstrate that significant water head declines in specific aquifers drive substantial compaction while rising water heads in other aquifers lead to swelling. The challenges posed by data scarcity and the need for continuous monitoring are emphasized, underscoring the importance of integrating different monitoring techniques to achieve accurate subsidence driver interpretation.

The investigation into natural hazards in Saint-Vaast focused on a region significantly affected by historical mining activities, particularly due to the presence of abandoned drainage galleries and changes in groundwater dynamics. The geological setting, characterized by Wealden terrains and historical mining galleries, played a crucial role in influencing subsurface dynamics and associated hazards. The study integrated three decades of SAR data from ERS (1992–2001), Envisat (2003–2010), and Sentinel (2016–2023), along with 13 years of piezometric wells data (2009–2023), to analyze ground deformation patterns and their hydrogeological drivers. The PS-InSAR analysis revealed a complex pattern of ground displacement, with phases of uplift and subsidence influenced by changes in subsurface water pressures. This deformation is also significantly affected by the mudflow outbursts, which have transported a substantial number of loose sediments toward the surface of the valley. The temporal progression of these displacement patterns was closely linked to hydrogeological disturbances, including clogging and pressure rising in the drainage gallery and then subsequent mudflow outbursts.

Two significant incidents in 2009 and 2018 were analyzed in detail. The PS-InSAR time series data indicated that the initial uplift phase observed from

2003 to 2009 was followed by a period of stability, which ended with the first documented clog rupture in 2009. This incident was attributed to the progressive rising of groundwater heads in the chalk aquifer and increasing pressures in the confining layers of clay in Wealden layers, leading to increased pore water pressure and subsequent pressure release. The radar data gap from 2010 to 2016 limited direct observations. However, the important subsidence following the 2009 mud outburst suggests that not only compaction occurred but also a significant transport of sediments out of the previously clogged gallery towards the valley. The reoccurrence of uplift in the Sentinel data from 2016 to 2018, followed by a shift to subsidence in 2018, coincides remarkably with the second outburst. This shows probably again a non-negligible transport of sediments, but this time directly to the river Haine using the pipe which was installed in 2009 as a precaution for future similar events.

The analysis of measured piezometric heads in Saint-Vaast provided key insights into the hydrogeological dynamics influencing ground deformation. Water head fluctuations in the aquifer correlated with ground displacement events. After the 2009 incident, water heads initially dropped, then stabilized and recovered. A sharp rise in water heads at the end of 2018, suggested a second clogging evolution followed by a rupture. This triggered rapid subsidence, which slowed over time but highlighted the vulnerability of area to subsurface pressure changes. Identifying critical breakpoints in the displacement and piezometric time series data highlighted the direct link between subsurface water pressures and ground stability, emphasizing the need for continuous monitoring and preventive measures to mitigate future risks.

In conclusion, the investigation into hydrogeological hazards in Saint-Vaast emphasizes the complex interaction between geological structures and natural and anthropogenic hydrogeological processes. The study highlights the necessity for integrated monitoring systems that combine PS-InSAR and piezometric analyses to provide a comprehensive understanding of ground deformation dynamics. The recurring pattern of uplift and subsidence observed in the region is so meaningful that monitoring both time series can robustly predict future similar patterns. Based on the observed trends, while there appears to be a pattern of incidents occurring approximately every 9-11 years, it is more likely that these events are influenced by variations in effective groundwater recharge rather than a strict cycle. For example, the unusually wet conditions since last October could have accelerated the process, potentially leading to an earlier significant event than previously anticipated. This hypothesis could be confirmed by observing the rising groundwater levels in the coming months. This prediction shows the need for proactive measures to manage and mitigate the risks associated with subsurface geohazards in the region.

The dissertation's findings from both Antwerp and Saint-Vaast underscore the critical importance of integrated geodetic and hydrogeological monitoring in understanding and managing land subsidence and hydrogeological hazards in post-mining regions. The comprehensive analysis combining PS-InAR data with numerical modeling and piezometric monitoring provided valuable insights into the subsurface dynamics driving ground deformation. In both regions, the challenges posed by data scarcity and the need for continuous high-quality data collection were emphasized. The successful application of advanced geodetic techniques and hydrogeological analysis demonstrated the importance of integrating different monitoring approaches to achieve accurate subsidence assessments and effective risk management.

6.2. Perspectives

The research on land deformation and hydrogeological hazards in Antwerp and Saint-Vaast has laid a solid groundwork for future studies and strategies for mitigation. While the investigation has provided valuable insights through the application of PS-InSAR analysis, piezometric well monitoring, and numerical modeling, it has also highlighted several areas that warrant further research and development to enhance our understanding and management of these geohazards.

The study points out several key areas for future exploration and mitigation efforts: In Antwerp, the study reveals the critical importance of understanding/recording stress factors and pumping activities that accurately reflect real-world conditions. Collecting detailed and reliable data on stress factors and especially pumping activities should be a priority. This involves accurate documentation and continuous monitoring of industrial activities and water extraction rates. Understanding these factors is crucial for creating precise models of subsurface stress and simulating their impacts on land subsidence. Additionally, expanding the network of piezometric wells remains essential. Increasing both the spatial and temporal resolution of the recorded piezometric heads in the wells will improve the understanding of groundwater head variations and their impact on subsurface effective stress. This involves strategic location choices to cover different hydrogeological settings, and frequent monitoring to capture rapid groundwater head changes. Increasing the number of piezometric wells would allow us to construct a more detailed and reliable model covering an extended region. With more piezometric data, specific areas, including those with high-resolution data such as TerraSAR-X can be considered during periods when we face a temporal gap of mid-resolution SAR data. This will increase the common periods between two displacement time series from the 1D geomechanical model and PS-InSAR, providing a more robust comparison. Additionally, having longer-term piezometric data would enable us to dedicate a portion of it to validate the results of the 3D flow model. This ensures that the inputs to the 1D geomechanical model, which are derived from the simulated 3D flow model, are reliable.

Ensuring the accuracy of reference points is critical for reliable PS-InSAR analysis. The installation of Integrated Geodetic Reference Stations (IGRS) in Antwerp, operational since May 2023, provides a stable and accurate reference point for future displacement measurements.

One of the critical insights from this study is the need for accurate and stable reference points to ensure reliable PS-InSAR displacement measurements. The installation of IGRS can help tackle the reference point problem observed in both Antwerp and Saint-Vaast case studies, where different satellite missions used different reference points, leading to potential biases in displacement estimations. Further deployment of IGRS across Belgium is essential, particularly in regions with active deformation such as Mechelen, Leuven, Brussels and Saint-Vaast. Strategically positioning IGRS near urban areas, industrial zones, and regions of significant groundwater extraction would provide a more accurate, stable reference for InSAR and GNSS observations. The coordination of such deployments should involve national geodetic agencies like the National Geographic Institute of Belgium

The deployment of extensometers could also significantly enhance future studies by providing detailed measurements of the displacement between two points, capturing vertical deformations in specific sublayers, including aquitards and aquifers. This data can be used to validate the 1D geomechanical model results, providing an additional data set for calibration of the subsidence simulations.

References

Abidin HZ, Andreas H, Gumilar I, Fukuda Y, Pohan YE, Deguchi T (2011) Land subsidence of Jakarta (Indonesia) and its relation with urban development, Natural Hazards J. 59(3): 1753–1771, doi: 10.1007/s11069-011-9866-9

Abidin HZ, Gumilar I, Andreas H, Murdohardono D, Fukuda Y (2013) On causes and impacts of land subsidence in Bandung Basin, Indonesia. Environmental earth sciences, 68:1545-1553. doi: 10.1007/s12665-012-1848-z

Allen DR (1988) Land subsidence caused by fluid removal (CONF-880301-). American Association of Petroleum Geologists, Tulsa, U.S. https://www.osti.gov/biblio/6544342

Allen JJ (1973) The effects of stress history on the resilient response of soils, Army Construction Engineering Research Laboratory.

Anderson MP, Woessner WW, Hunt RJ (2015) Applied groundwater modeling: simulation of flow and advective transport. Academic press.

Ansar AMH, Din AHM, Latip ASA, Reba MNM (2022) a Short Review on Persistent Scatterer Interferometry Techniques for Surface Deformation Monitoring. The International Archives of the Photogrammetry, Remote Sensing and Spatial Information Sciences, 46:23-31. doi: 10.5194/isprs-archives-XLVI-4-W3-2021-23-2022

Aquaveo (2023) Groundwater Modeling System (GMS)

Armaş, I., Gheorghe, M., Lendvai, A. M., Dumitru, P. D., Bădescu, O., & Călin, A. (2016). InSAR validation based on GNSS measurements in Bucharest. International Journal of Remote Sensing, 37(23), 5565-5580. doi: 10.1080/01431161.2016.1244367

Aswathi J, Kumar RB, Oommen T, Bouali EH, Sajinkumar KS (2022) InSAR as a tool for monitoring hydropower projects: A review. Energy Geoscience, 3(2):160–171. doi: 10.1016/j.engeos.2021.12.007

Azadnejad S, Hrysiewicz A, Trafford A, O'Loughlin F, Holohan EP, Kelly F, Donohue S (2024) InSAR supported by geophysical and geotechnical information constrains two-dimensional motion of a railway embankment constructed on peat. Engineering Geology, 333:107493. doi: 10.1016/j.enggeo.2024.107493

Baghbani AN, Choudhury T, Costa S, Reiner J (2022) Application of artificial intelligence in geotechnical engineering: A state-of-the-art review. Earth-Science Reviews J. 228, 103991, doi: 10.1016/j.earscirev.2022.103991

Bagheri-Gavkosh, M, Hosseini SM, Ataie-Ashtiani B, Sohani Y, Ebrahimian H, Morovat F, Ashrafi S (2021) Land subsidence: A global challenge. Science of The Total Environment 778:146193. doi:10.1016/j.scitotenv.2021.146193

Bayer B, Schmidt D, Simoni A (2017) The influence of external digital elevation models on PS-InSAR and SBAS results: Implications for the analysis of deformation signals caused by slow-moving landslides in the northern Apennines (Italy). IEEE Transactions on Geoscience and Remote Sensing, 55(5):2618–2631. doi: 10.1109/TGRS.2017.2648885

Bejani MM, Ghatee M (2021) A systematic review on overfitting control in shallow and deep neural networks, Artificial Intelligence Review J. 54(8):6391–6438, doi:10.1007/s10462-021-09975-1

Berardino P, Fornaro G, Lanari R, Sansosti E (2002) A new algorithm for surface deformation monitoring based on small baseline differential SAR interferograms. IEEE Transactions on geoscience and remote sensing, 40(11):2375–2383. doi: 10.1109/TGRS.2002.803792

Berardino P, Fornaro G, Lanari R, Sansosti E (2002) A new algorithm for surface deformation monitoring based on BGR (Geosciences and Natural Resources), NESCO (United Nations Educational, Scientific and Cultural Organization) (2013): International Hydrogeological Map of Europe 1:1,500,000, 25 sheets and 18 explanatory notes; Hanover. Website: https://www.bgr.bund.de/EN/Themen/Wasser/Projekte/laufend/Beratung/Ihme1500/ihme1500_projektbeschr_en.html?nn=1557832. Cited 26 June 2024.

Biot MA (1941) General theory of three-dimensional consolidation. Applied Physics J. 12(2):155–164, doi: 10.1063/1.1712886

Bitelli G, Bonsignore F, Unguendoli M (2000) Levelling and GPS networks to monitor ground subsidence in the Southern Po Valley. Journal of Geodynamics 30(3):355–369. doi:10.1016/S0264-3707(99)00071-X

Blackledge JM (2005) Chapter 10 - Synthetic Aperture Imaging. In Digital Image Processing: Mathematical and Computational Methods. Woodhead Publishing.

Bokhari R, Shu H, Tariq A, Al-Ansari N, Guluzade R, Chen T, ... & Aslam M (2023) Land subsidence analysis using synthetic aperture radar data. Heliyon, 9(3). doi: 10.1016/j.heliyon.2023.e14690

Bouraoui S (2013) Time series analysis of SAR images using persistent scatterer (PS), small baseline (SB) and merged approaches in regions with small surface deformation (Doctoral dissertation, Université de Strasbourg).

Bourbigot M (2016) Sentinel-1 Product Definition.

Brinkgreve RB, Vermeer PA (Eds.). (1999). Plaxis: finite element code for soil and rock analyses: version 7: [user's guide]. Balkema

Brouwer WS, Hanssen RF (2023) A treatise on InSAR geometry and 3D displacement estimation. IEEE Transactions on Geoscience and Remote Sensing. doi: 10.1109/TGRS.2023.3322595

Burbey TJ (2002) The influence of faults in basin-fill deposits on land subsidence, Las Vegas Valley, Nevada, USA. Hydrogeology J. 10(5):525–538, doi: 10.1007/s10040-002-0215-7

small baseline differential SAR interferograms, IEEE Transactions on Geoscience and Remote Sensing J. 40(11): 2375–2383, doi: 10.1109/TGRS.2002.803792

Bürgmann R, Rosen PA, Fielding EJ (2000) Synthetic aperture radar interferometry to measure Earth's surface topography and its deformation. Annual review of earth and planetary sciences, 28(1):169–209. doi: 10.1146/annurev.earth.28.1.169

Cai Y, Jin Y, Wang Z, Chen T, Wang Y, Kong W, Xiao W, Li X, Lian X, Hu H (2023) A review of monitoring, calculation, and simulation methods for ground subsidence induced by coal mining. International Journal of Coal Science & Technology 10(1): 32. doi: 10.1007/s40789-023-00595-4

Calderhead AI, Therrien R, Rivera A, Martel R, Garfias J (2011) Simulating pumping-induced regional land subsidence with the use of InSAR and field data in the Toluca Valley, Mexico. Advances in Water Resources J. 34(1): 83–97, doi: 10.1016/j.advwatres.2010.09.017

Camelbeeck T, Van Noten K, Lecocq T, Hendrickx M (2022) The damaging character of shallow 20th century earthquakes in the Hainaut coal area (Belgium). Solid Earth 13(3):469–495. doi: 10.5194/se-13-469-2022

Challis K, Kokalj Z, Kincey M, Moscrop D, Howard AJ (2008) Airborne lidar and historic environment records, Antiquity J. 82(318):1055–1064, doi: 10.1017/S0003598X00097775

Chang L, Dollevoet RP, Hanssen RF (2018) Monitoring line-infrastructure with multisensor SAR interferometry: Products and performance assessment metrics. IEEE journal of selected topics in applied earth observations and remote sensing, 11(5):1593–1605. doi: 10.1109/JSTARS.2018.2803074

Chaussard E, Amelung F, Abidin H, Hong SH (2013) Sinking cities in Indonesia: ALOS PALSAR detects rapid subsidence due to groundwater and gas extraction. Remote Sensing of Environment 128:150–161. doi: 10.1016/j.rse.2012.10.015

Chaussard E, Burgmann R, Shirzaei M, Fielding EJ, Baker B (2014) Predictability of Hydraulic Head Changes and Characterization of Aquifer-System and Fault Properties from InSAR-Derived Ground Deformation, Geophysical Research: Solid Earth J. 119(8): 6572–6590, doi: 10.1002/2014JB011266.

Chen CW, Zebker HA. 2000. Network approaches to two-dimensional phase unwrapping: Intractability and two new algorithms. JOSA A. 17(3):401–414. doi: 10.1364/josaa.17.000401

Chen CW, Zebker HA. 2001. Two-dimensional phase unwrapping with use of statistical models for cost functions in nonlinear optimization. JOSA A. 18(2):338–351. doi: 10.1364/JOSAA.18.000338

Chen CW, Zebker HA. 2002. Phase unwrapping for large SAR interferograms: Statistical segmentation and generalized network models. IEEE Transactions on Geoscience and Remote Sensing. 40(8):1709–1719. doi: 10.1109/TGRS.2002.802453

Chen J, Liu L, Zhang T, Cao B, Lin H (2018) Using Persistent Scatterer Interferometry to Map and Quantify Permafrost Thaw Subsidence: A Case Study of Eboling Mountain on the Qinghai-Tibet Plateau. Journal of Geophysical Research: Earth Surface 123(10):2663–2676. doi: 10.1029/2018JF004618

Chen X, Tessari G, Fabris M, Achilli V, Floris M (2021) Comparison Between PS and SBAS InSAR Techniques in Monitoring Shallow Landslides. In: Casagli, N., Tofani, V., Sassa, K., Bobrowsky, P.T., Takara, K. (eds) Understanding and Reducing Landslide Disaster Risk. WLF 2020. ICL Contribution to Landslide Disaster Risk Reduction. Springer, Cham. p 155–161

Chen Y, Luo Y, Feng M (2013) Analysis of a discontinuous Galerkin method for the Biot's consolidation problem, Applied Mathematics and Computation J. 219(17): 9043–9056, doi: 10.1016/j.amc.2013.03.104

Chen Y, Tao Q, Hou A, Ding L, Liu G, Wang K (2020) Accuracy verification and evaluation of Sentinel-1A repeat track differential interferometric synthetic aperture radar in monitoring mining subsidence, Applied Remote Sensing J. 14(1): 014501-014501, doi: 10.1117/1.JRS.14.014501

Chen Y, Xia J, Yu C, Chen B (2022) InSAR crustal deformation monitoring, modeling and error analysis. Frontiers in Environmental Science, 10:1009492. doi: 10.3389/fenvs.2022.1009492

Choopani A, Declercq PY, Orban P, Devleeschouwer X, Dassargues A (2021) Land subsidence as revealed by PS-InSAR observations in the Antwerp area (Belgium): first steps towards the understanding and modeling. In IAH2021 48th IAH Congress 'Inspiring Groundwater', doi: 10.13140/RG.2.2.28064.46088

Choopani A, Declercq PY, Verbeurgt J, De Doncker F, Orban P, Devleeschouwer X, Dassargues A (2023) Subsidence evolution of Antwerp region, Belgium over 77 years, using historical leveling and GNSS data and recent Persistent Scatterers Interferometry observations, EGU General Assembly 2023, Vienna, Austria, 24–28 Apr 2023, EGU23-9863, doi: 10.5194/egusphere-egu23-9863.

Choopani A, Dehghani M, Nikoo MR (2019) Determining hydrogeological parameters of an aquifer in Sirjan basin using Envisat ASAR interferometry and groundwater modeling, Remote Sensing J. 41(2):655-682, doi: 10.1080/01431161.2019.1646938

Choopani A, Ronchi B, Declercq PY, Devleeschouwer X (2022, November) Ground Deformations Related to an Old Drainage Adit in The Abandoned Coal Concession Around Saint-Vaast (Wallonia, Belgium) Analyzed Using PS InSAR and Piezometric Wells Time Serie. In International Mine Water Association Conference (IMWA 2022).

Cigna F, Del Ventisette C, Liguori V, Casagli N (2011) Advanced radar-interpretation of InSAR time series for mapping and characterization of geological processes. Natural Hazards and Earth System Sciences, 11(3):865-881. doi: 10.5194/nhess-11-865-2011, 2011

Costantino D, Angelini MG (2011) Geodetic monitoring applied to a mine area. Applied Geomatics 3(2):61–74. doi: 10.1007/s12518-011-0047-z

Craig RF, (2004). Craig's soil mechanics. CRC press.

Crosetto M, Monserrat O, Cuevas-González M, Devanthéry N, Crippa B (2016) Persistent scatterer interferometry: A review. ISPRS Journal of Photogrammetry and Remote Sensing, 115:78–89. doi: 10.1016/j.isprsjprs.2015.10.011

Czikhardt, R., Van Der Marel, H., & Papco, J. (2021). GECORIS: An open-source toolbox for analyzing time series of corner reflectors in InSAR geodesy. Remote Sensing, 13(5), 926. doi: 10.3390/rs13050926

Dassargues A (1995) On the necessity to consider varying parameters in land subsidence computations. In: Barends FBJ, Brouwer FJJ, Schroder FH (eds) Proceeding of the 5th International Symposium on Land Subsidence, The Hague, The Netherlands, 16-20 October 1995. IAHS Press, Wallingford. p. 258–269

Dassargues A (1998) Prise en compte des variations de la permeabilite et du coefficient d'emmagasinement specifique dans les simulations hydrogeologiques de la consolidation en milieux argileux satures, Bulletin de la Société Géologique de France J. 169(5):665-673

Dassargues A (2018) Hydrogeology: Groundwater Science and Engineering. CRC Press.

Dassargues A, Radu JP, Charlier R, Li XL, Li QF (1993). Computed subsidence of the central area of Shanghai. Bulletin of Engineering Geology and the Environment, 47:65–88, doi: 10.1007/BF02639592.

Dassargues A, Schroeder C, Li XL (1993) Applying the Lagamine model to compute land subsidence in Shanghai. Bulletin of Engineering Geology and the Environment. 47:13–26, doi: 10.1007/BF02639591

Davis EH, Raymond GP (1965) A Non-Linear Theory of Consolidation. Géotechnique J. 15(2):161–173, doi: 10.1680/geot.1965.15.2.161

Declercq PY, Choopani A, Dassargues A, Devleeschouwer X (2021) Areas Prone to Land Subsidence and their Evolutions in Belgium During the Last 30 Years. 2021 IEEE International Geoscience and Remote Sensing Symposium IGARSS, 8448–8451. doi: 10.1109/IGARSS47720.2021.9554738

Declercq PY, Dusar M, Pirard E, Verbeurgt J, Choopani A, Devleeschouwer X (2023) Post Mining Ground Deformations Transition Related to Coal Mines Closure in the Campine Coal Basin, Belgium, Evidenced by Three Decades of MT-InSAR Data. Remote Sensing 15(3): 725 doi:10.3390/rs15030725

Declercq PY, Gérard P, Pirard E, Walstra J, Devleeschouwer X (2021) Long-term subsidence monitoring of the alluvial plain of the Scheldt river in Antwerp (Belgium) using radar interferometry, Remote Sensing J, 13(6): 1160–1180, doi: 10.3390/rs13061160

Dehghani M, Nikoo MR (2019) Monitoring and Management of Land Subsidence Induced by Over-exploitation of Groundwater. In H. R. Pourghasemi & M. Rossi (Eds.), Natural Hazards GIS-Based Spatial Modeling Using Data Mining Techniques 271–296. doi: 10.1007/978-3-319-73383-8_12

Dehghani M, Zoej MJV, Entezam I (2013) Neural network modeling of Tehran land subsidence measured by Persistent Scatterer Interferometry, Photogrammetrie - Fernerkundung – Geoinformation J. 5–17 doi: 10.1127/1432-8364/2013/0154

Del Soldato M, Confuorto P, Bianchini S, Sbarra P, Casagli N (2021) Review of Works Combining GNSS and InSAR in Europe, Remote Sensing J. 13(9):1684–1711, doi: 10.3390/rs13091684

Deng YF, Tang AM, Cui YJ, Nguyen XP, Li XL, Wouters L (2011) Laboratory hydro-mechanical characterization of Boom Clay at Essen and Mol, Physics and Chemistry of the Earth J. 36(17–18):1878–1890, doi: 10.1016/j.pce.2011.10.002

Deruyter G, De Wulf A, Vercruysse J (2022) Influence of the I95-index and local parameters on the accuracy of GNSS positioning, Proceedings of 22nd International Multidisciplinary Scientific GeoConference SGEM 2022: 22(2.1): 409–416, doi: 10.5593/sgem2022/2.1/s11.48

Destatte P (1997) L'identité wallonne: Essai sur l'affirmation politique de la Wallonie aux XIX et XXèmes siècles. Institut Jules Destrée

Destination Terrils. (n.d.). Terril Albert 1er. Retrieved July 19, 2024, from https://www.destinationterrils.eu/fr/terril-albert-1er

Detournay E, Cheng AHD (1993). Fundamentals of Poroelasticity. In Fairhurst C (ed) Analysis and design methods, Pergamon. pp 113–171

Devleeschouwer X, Devlercq PY, Dusar M (2008) Ground motions revealed in the coal mining districts (Campine basin) using radar interferometry (PSInSAR technique). Syllabus Studiedag, Toegepaste geologische kartering in Vlaanderen en op het continentaal plat: nieuwe toepassingen en digitale technieken, 12 juni 2008, VITO NV, Mol, Belgium, 6 pages.

Devleeschouwer X, Devlercq PY, Dusar M Debien A (2008) Contrasting ground movements revealed by radar interferometry over abandoned coal mines (Campine, Belgium). Proceedings of Fringe 2007 Workshop, 26-30 November 2007, ESA SP-649, Frascati, Italy, 12 pages.

Digitaal Vlaanderen (2023) GNSS data of Flemish Positioning Services (FLEPOS) network, Available from Royal Observatory of Belgium. doi:10.24414/ROB-FLEPOS

Domenico PA, Schwartz FW (1997) Physical and Chemical Hydrogeology. John Wiley & Sons.

Dong S, Samsonov S, Yin H, Ye S, Cao Y (2014) Time-series analysis of subsidence associated with rapid urbanization in Shanghai, China measured with SBAS InSAR method, Environmental Earth Sciences J. 72(3): 677–691, doi: 10.1007/s12665-013-2990-y

Drevet JP, Frippiat C, Stassen F, Veschkens M (2010) Study of the consequences of post-mining in particular on groundwater and risk management (2011–01630) ISSeP Scientific Institute of public service.

Drevet JP, Frippiat C, Stassen F, Veschkens M (2011) Etude des conséquences de l'Après-Mine en particulier sur la gestion des eaux souterraines et des risques. ISSeP Scientific Institute of Public Service, Rapport n° 2011-01630, SUBVENTION 2010, Projet de rapport annuel, add number of pages.

Duncan JM, Chang CY (1970) Nonlinear analysis of stress and strain in soils, Soil Mechanics and Foundations Division J. 96(5): 1629–1653, doi: 10.1061/JSFEAQ.0001458

Dzurisin D, Lu Z (2007). Interferometric synthetic-aperture radar (InSAR). In: Volcano Deformation. Springer Praxis Books. Springer, Berlin, Heidelberg. doi: 10.1007/978-3-540-49302-0_5

Ebrahimy H, Feizizadeh B, Salmani S, Azadi H (2020) A comparative study of land subsidence susceptibility mapping of Tasuj plane, Iran, using boosted regression tree, random forest and classification and regression tree methods, Environmental Earth Sciences J. 79:1-12, doi: 10.1007/s12665-020-08953-0

Eghrari Z, Delavar MR, Zare M, Beitollahi A, Nazari B (2023) land subsidence susceptibility mapping using machine learning algorithms, ISPRS Annals of the Photogrammetry, Remote Sensing and Spatial Information Sciences J. 10:129-136, doi: 10.5194/isprs-annals-X-4-W1-2022-129-2023

Eineder M, Hubig M, Milcke B (1998, July) Unwrapping large interferograms using the minimum cost flow algorithm. In IGARSS'98. Sensing and Managing the Environment. 1998 IEEE International Geoscience and Remote Sensing. Symposium Proceedings. (Cat. No. 98CH36174) (Vol. 1, pp. 83-87). IEEE. doi: 10.1109/IGARSS.1998.702806

El Kamali M, Abuelgasim A, Papoutsis I, Loupasakis C, Kontoes C (2020) A reasoned bibliography on SAR interferometry applications and outlook on big interferometric data processing. Remote Sensing Applications: Society and Environment, 19:100358. doi: 10.1016/j.jog.2016.08.001

El Rai MC, Simonetto E (2009, September) PS-InSAR experiments for the analysis of urban ground deformation using StaMPS. In Image and Signal Processing for Remote Sensing XV (Vol. 7477: 437–443). SPIE. doi: doi.org/10.1117/12.830077

Eneva M, Falorni G, Adams D, Novali F (2011) Advanced InSAR Techniques for Measuring Surface Deformation in Geothermal Fields.

Esposito G, Clement J, Mora L, Crutzen N (2021) One size does not fit all: Framing smart city policy narratives within regional socio-economic contexts in Brussels and Wallonia. Cities 118:103329. doi: 10.1016/j.cities.2021.103329

Esri Netherlands (2015) https://esrinl-content.maps.arcgis.com/home/group.html?id=9cf0ea95e1b14f2e86a559ee620de15d&view=list&start=141&num=20#content

Estahbanati AT, Dehghani M (2018) A phase unwrapping approach based on extended Kalman filter for subsidence monitoring using persistent scatterer time series interferometry. IEEE Journal of Selected Topics in Applied Earth Observations and Remote Sensing, 11(8):2814–2820. doi: 10.1109/JSTARS.2018.2837020

Famiglietti JS (2014) The global groundwater crisis. Nature Climate Change J. 4(11): 945–948, doi: 10.1038/nclimate2425

Farr TG, Rosen PA, Caro E, Crippen R, Duren R, Hensley S, Kobrick M, Paller M, Rodriguez E, Roth L, Seal D (2007) The shuttle radar topography mission. Reviews of geophysics 45(2). doi: 10.1029/2005RG000183

Faryabi M (2023) A fuzzy logic approach for land subsidence susceptibility mapping: The use of hydrogeological data, Environmental Earth Sciences J. 82(9):209, doi: 10.1007/s12665-023-10909-z

Feng H, Zhou J, Zhou A, Xu H, Su D, Han X (2022) Spatiotemporal variation indicators for vegetation landscape stability and processes monitoring of semiarid grassland coal mine areas. Land Degradation & Development 33(1):3–17. doi: 10.1002/ldr.4073

Ferretti A (2014) Satellite InSAR Data: reservoir monitoring from space (EET 9). Earthdoc.

Ferretti A, Monti-Guarnieri A, Prati C, Rocca F, Massonet D (2007) InSAR principles-guidelines for SAR interferometry processing and interpretation. ESA

Ferretti A, Novali F, Fumagalli A, Prati C, Rocca F, Rucci A (2009) Beyond PSInSAR: The SQUEESAR Approach. 2009, G31A-02.

Ferretti A, Prati C, Rocca F (1999) Permanent scatterers in SAR interferometry. In IEEE 1999 International Geoscience and Remote Sensing Symposium. IGARSS'99 (Cat. No. 99CH36293), 3:1528–1530). IEEE. doi: 10.1109/IGARSS.1999.772008

Ferretti A, Prati C, Rocca F (2000) Nonlinear subsidence rate estimation using permanent scatterers in differential SAR interferometry. IEEE Transactions on geoscience and remote sensing, 38(5):2202–2212. doi: 10.1109/36.868878

Ferretti A, Prati C, Rocca F (2000) Nonlinear subsidence rate estimation using permanent scatterers in differential SAR Interferometry, IEEE Transactions on Geoscience and Remote Sensing J. 38(5): 2202–2212, doi: 10.1109/36.868878

Ferretti A, Prati C, Rocca F (2001). Permanent scatterers in SAR interferometry, IEEE Transactions on Geoscience and Remote Sensing J. 39(1): 8–20, doi: 10.1109/36.898661

Figueroa-Miranda S, Tuxpan-Vargas J, Ramos-Leal JA, Hernández-Madrigal VM, Villaseñor-Reyes CI (2018) Land subsidence by groundwater over-exploitation from aquifers in tectonic valleys of Central Mexico: A review. Engineering Geology, 246:91–106. doi: 10.1016/j.enggeo.2018.09.023

Findley WN, Lai JS, Onaran K (2013). Creep and relaxation of nonlinear viscoelastic materials. Dover Publication, Inc, New York.

Fiorentini N, Maboudi M, Leandri P, Losa M, Gerke M (2020) Surface motion prediction and mapping for road infrastructures management by PS-in SAR measurements and machine learning algorithms, Remote Sensing J. 12(23): 3976–3976, doi: 10.3390/rs12233976

Forster A (2000) Environmental Geology: Principles and Practice. Quarterly Journal of Engineering Geology and Hydrogeology J. 33(4): 350–351, doi: 10.1144/qjegh.33.4.350-b

Frippiat C, Veschkens M, Pacyna D, Funcken L (2013) Non-conclusive time series analyses – what can we learn on the behavior of the groundwater system? Understanding what caused the collapse of an abandoned drainage tunnel. Reliable Mine Water Technology 2:995–1002. Denver, Colorado, USA (Publication Printers).

Gabrysch RK, Bonnet CW (1975) Land-surface subsidence in the Houston-Galveston Region, Texas. Texas Water Development Board.

Gabrysch RK, Coplin LS (1990) Land-surface subsidence resulting from ground-water withdrawals in the Houston-Galveston region, Texas, through 1987. U.S. Geological Survey, doi: 10.3133/1391

Galloway D L, Burbey TJ (2011) Review: Regional land subsidence accompanying groundwater extraction, Hydrogeology J. 19(8):459–1486, doi:10.1007/s10040-011-0775-5

Galloway D, Riley FS (1999) San Joaquin Valley: California largest human alteration of the Earth’s surface. Land Subsidence in the United States, U.S. Geological Survey Circular, 1182: 23-34.

Galloway DL, Jones DR, Ingebritsen SE (1999) Land Subsidence in the United States. U.S. Geological Survey, doi: 10.3133/cir1182

Galloway DL, Jones DR, Ingebritsen SE (1999). Land Subsidence in the United States. U.S. Geological Survey.

Gambolati G, Freeze RA (1973) Mathematical simulation of the subsidence of Venice: 1. Theory, Water Resources Research J. 9(3):721–733, doi: 10.1029/WR009i003p00721

Gambolati G, Gatto P, Freeze RA (1974) Predictive simulation of the subsidence of

Venice. Science 183(4127):849–851, doi: 10.1126/science.183.4127.849

Gambolati G, Teatini P (2015) Geomechanics of subsurface water withdrawal and injection, Water Resources Research J. 51(6): 3922–3955, doi: 10.1002/2014WR016841

Garthwaite, M. C. (2017). On the design of radar corner reflectors for deformation monitoring in multi-frequency InSAR. Remote Sensing, 9(7), 648. doi: 10.3390/rs9070648

Garthwaite, M. C., Nancarrow, S., Hislop, A., Thankappan, M., Dawson, J. H., & Lawrie, S. (2015). Design of radar corner reflectors for the Australian Geophysical Observing System. Geoscience Australia, 3, 490.

Gedeon M, Wemaere I, Marivoet J (2007) Regional groundwater model of north-east Belgium, Hydrology J. 335(1):133–139, doi: 10.1016/j.jhydrol.2006.11.006

Geertsma J (1973) Land subsidence above compacting oil and gas reservoirs. Petroleum Technology J. 25(06): 734–744, doi: 10.2118/3730-PA

Geological 3D model (v3.1). Available from the Databank Ondergrond Vlaanderen (DOV) https://www.dov.vlaanderen.be. Cited 27 June 2024.

Geotechnics Department in Flanders (1999) Report on the results of the drillings with associated laboratory research carried out in connection with the construction of a buffer dike phase in the Waasland Haven in Beveren (Report numbers GEO-00-103/GEO-73-364B/GEO-83-111)

Ghorbani Z, Khosravi A, Maghsoudi Y, Mojtahedi FF, Javadnia E, Nazari A (2022) Use of InSAR data for measuring land subsidence induced by groundwater withdrawal and climate change in Ardabil Plain, Iran, Scientific Reports J. 12(1): 13998–14020, doi: 10.1038/s41598-022-17438-y

GNSS Metadata (2024). DOEL00BEL Site Information. Retrieved August 7, 2024, from https://gnss-metadata.eu/MOID/station.64b7f391b1f58be93303b347

Gonnuru P, Kumar S (2018) PS-InSAR based land subsidence estimation of Burgan oil field using TerraSAR-X data. Remote Sensing Applications: Society and Environment 9:17–25. doi: 10.1016/j.rsase.2017.11.003

Gualandi A, Liu Z (2021) Variational Bayesian independent component analysis for InSAR displacement time-series with application to Central California, USA, Geophysical Research: Solid Earth J. 126(4), doi: 10.1029/2020JB020845

Guzy A, Malinowska AA (2020) State-of-the-art and recent advancements in the modeling of land subsidence induced by groundwater withdrawal. Water J. 12(7):2051–2092, doi: 10.3390/w12072051

Hanssen RF (2001) Radar interferometry: data interpretation and error analysis (Vol. 2). Springer Science & Business Media.

Hanssen RF (2004) Stochastic modelling of time series radar interferometry. In IGARSS 2004. 2004 IEEE International Geoscience and Remote Sensing Symposium 4:2607–2610. IEEE. doi: 10.1109/IGARSS.2004.1369832

Hanssen RF, Klees R (1998) Applications of SAR interferometry in terrestrial and atmospheric mapping. In European Microwave Week (pp. 5-9).

Hartman HL, Mutmansky JM (2002) Introductory Mining Engineering. John Wiley & Sons

Heiken G, Funiciello R, Rita DD (2013) The seven hills of Rome: a geological tour of the eternal city. in the seven hills of Rome. Princeton University Press. doi: 10.1515/9781400849376

Helm DC (1976) One-dimensional simulation of aquifer system compaction near Pixley, California, Water Resources Research J. 11(3): 465–478, doi: 10.1029/WR011i003p00465

Helm DC (1986) COMPAC: a field-tested model to simulate and predict subsidence due to fluid withdrawal, Austral Geomechan Comput Newslett, 10:18-20.

Herrera-García G, Ezquerro P, Tomás R, Béjar-Pizarro M, López-Vinielles J, Rossi M, ... & Ye S (2021) Mapping the global threat of land subsidence. Science, 371(6524): 34–36. doi: 10.1126/science.abb8549

Hoffmann J (2003). The application of satellite radar interferometry to the study of land subsidence over developed aquifer systems. Stanford University

Holzer TL, Bluntzer RL (1984) Land subsidence near oil and gas fields, Houston, Texas, Groundwater J. 22(4): 450–459, doi: 10.1111/j.1745-6584.1984.tb01416.x

Holzer TL, Galloway DL (2005) Impacts of land subsidence caused by withdrawal of underground fluids in the United States. In J. Ehlen, W. C. Haneberg, & R. A. Larson (Eds.), Humans as Geologic Agents. Geological Society of America. doi: 10.1130/2005.4016(08)

Hongdong F, Kazhong D, Chengyu J, Chuanguang Z, Jiqun X (2011). Land subsidence monitoring by D-InSAR technique, Mining Science and Technology (China) J. 21(6):869–872, doi: 10.1016/j.mstc.2011.05.030

Hooper A (2008) A multi-temporal InSAR method incorporating both persistent scatterer and small baseline approaches, Geophysical Research Letters J. 35(16):302–307, doi: 10.1029/2008GL034654

Hooper A (2008) A multi-temporal InSAR method incorporating both persistent scatterer and small baseline approaches. Geophysical research letters, 35(16). doi: 10.1029/2008GL034654

Hooper A, Bekaert D, Spaans K, Arıkan M (2012) Recent advances in SAR interferometry time series analysis for measuring crustal deformation. Tectonophysics, 514:1–13. doi: 10.1016/j.tecto.2011.10.013

Hooper A, Segall P, Zebker H (2007) Persistent scatterer interferometric synthetic aperture radar for crustal deformation analysis, with application to Volcán Alcedo, Galápagos. Journal of Geophysical Research: Solid Earth, 112(B7). doi: 10.1029/2006JB004763

Hooper A, Segall P, Zebker H (2007) Persistent scatterer interferometric synthetic aperture radar for crustal deformation analysis, with application to Volcán Alcedo, Galápagos, Geophysical Research: Solid Earth J. 112(B7): 407–428, doi: 10.1029/2006JB004763

Hooper A, Zebker H, Segall P, Kampes B (2004) A new method for measuring deformation on volcanoes and other natural terrains using InSAR persistent scatterers. Geophysical Research Letters 31(23). doi: 10.1029/2004GL021737

Hooper A, Zebker HA (2007) Phase unwrapping in three dimensions with application to InSAR time series. JOSA A, 24(9), 2737–2747. doi: 10.1364/JOSAA.24.002737

Hrysiewicz A, Wang X, Holohan EP (2023) EZ-InSAR: An easy-to-use open-source toolbox for mapping ground surface deformation using satellite interferometric synthetic aperture radar. Earth Science Informatics, 16(2):1929–1945. doi: 10.1007/s12145-023-00973-1

Hu B, Chen J, Zhang X (2019) Monitoring the land subsidence area in a coastal urban area with InSAR and GNSS, Sensors J. 19(14):3181–3200, doi:10.3390/s19143181

Hu L. Wu H, Wen QB (2013) Electro-osmotic consolidation: Laboratory tests and numerical simulation. The 18th International Conference on Soil Mechanics and Geotechnical Engineering, Paris. 231–234.

Hu RL, Yue ZQ, Wang LU, Wang SJ (2004) Review on the current status and challenging issues of land subsidence in China. Engineering Geology J. 76(1-2):65-77, doi: 10.1016/j.enggeo.2004.06.006

Huang Y, Jin P (2018) Impact of human interventions on coastal and marine geological hazards: a review. Bulletin of Engineering Geology and the Environment, 77:1081–1090. doi: 10.1007/s10064-017-1089-1

Hubbert MK (1957) DARCY'S law and the field equations of the flow of underground fluids. International Association of Scientific Hydrology Bulletin. 2(1):23–59, doi: 10.1080/02626665709493062

Hudson Institute of Mineralogy. (n.d.). Albert 1 colliery, La Louvière, Hainaut, Wallonia, Belgium [Databank]. Mindat.Org. Retrieved September 20, 2023, from https://mindat.org/loc-418173.html

Igboekwe MU, Amos-Uhegbu C (2011) Fundamental approach in groundwater flow and solute transport modelling using the finite difference method. Earth and Environmental Sciences, 556:301–328. doi: 10.5772/26873

Ikuemonisan FE, Ozebo VC (2020) Characterisation and mapping of land subsidence based on geodetic observations in Lagos, Nigeria. Geodesy and Geodynamics, 11(2):151–162. doi: 10.1016/j.geog.2019.12.006

Jaeger JC, Cook NGW, Zimmerman R (2009) Fundamentals of Rock Mechanics. John Wiley & Sons.

Jafari F, Javadi S, Golmohammadi G, Karimi N, Mohammadi K (2016) Numerical simulation of groundwater flow and aquifer-system compaction using simulation and InSAR technique: Saveh basin, Iran. Environmental Earth Sciences J. 75:1–10, doi: 10.1007/s12665-016-5654-x

Jang JSR (1993) ANFIS: adaptive-network-based fuzzy inference system, IEEE Transactions on Systems, Man, and Cybernetics J. 23(3):665–685, doi:10.1109/21.256541

Jiang L, Bai L, Zhao Y, Cao G, Wang H, Sun Q (2018) Combining InSAR and hydraulic head measurements to estimate aquifer parameters and storage variations of the confined aquifer system in Cangzhou, North China Plain, Water Resources Research J. 54(10): 8234–8252 doi: 10.1029/2017WR022126

Jorgensen DG (1980) Relationships between basic soils-engineering equations and basic ground-water flow equations. US Government Printing Office.

Joyce KE, Samsonov SV, Levick SR, Engelbrecht J, Belliss S (2014) Mapping and monitoring geological hazards using optical, LiDAR, and synthetic aperture RADAR image data. Natural Hazards 73(2):137–163. doi: 10.1007/s11069-014-1122-7

Kampes B (1999) Delft Object-oriented Radar Interferometric Software User's manual and technical documentation. Delft University of Technology

Kamphuis, J. (2019). Co-location of geodetic reference points: On the design and performance of an Integrated Geodetic Reference Station.

Kenner R, Chinellato G, Iasio C, Mosna D, Cuozzo G, Benedetti E, Visconti MG, Manunta M, Phillips M, Mair V, Zischg A, Thiebes B, Strada C (2016) Integration of space-borne DInSAR data in a multi-method monitoring concept for alpine mass movements. Cold Regions Science and Technology 13165–75. doi: 10.1016/j.coldregions.2016.09.007

Khan J, Ren X, Afaq Hussain M, MQasil J (2022) Monitoring land subsidence using PS-InSAR technique in Rawalpindi and Islamabad, Pakistan. Remote Sensing J. 14(15):3722–3747, doi: 10.3390/rs14153722

Khoshghalb A, Khalili N (2010) A stable meshfree method for fully coupled flow-deformation analysis of saturated porous media, Computers and Geotechnics J. 37(6):789–795, doi: 10.1016/j.compgeo.2010.06.005

Khoshnevis SA, Ghorshi S (2020) A tutorial on tomographic synthetic aperture radar methods. SN Applied Sciences, 2(9):1504. doi: 10.1007/s42452-020-03298-6

Kim P, Kim YG, Paek CH, MJ (2019) Lattice Boltzmann method for consolidation analysis of saturated clay, Ocean Engineering, and Science J, 4(3): 193–202. doi:10.1016/j.joes.2019.04.004

Kim TTH, Tran HH, Phan TA, Lipecki T (2022) Mining-Induced Land Subsidence Detected by Persistent Scatterer InSAR: Case Study in Pniówek Coal Mine, Silesian Voivodeship, Poland. In International Conference on Geo-Spatial Technologies and Earth Resources (pp. 23-42). Cham: Springer International Publishing. doi: 10.1007/978-3-031-20463-0_2

Kivinen S, Vartiainen K, Kumpula T (2018) People and Post-Mining Environments: PPGIS Mapping of Landscape Values, Knowledge Needs, and Future Perspectives in Northern Finland. Land 7:151. doi: 10.3390/land7040151

Klees R, Massonnet D (1998) Deformation measurements using SAR interferometry: potential and limitations. Geologie en Mijnbouw, 77:161–176. doi: 10.1023/A:1003594502801

Krieger G, Hajnsek I, Papathanassiou K, Eineder M, Younis M, De Zan F, ... & Moreira A (2009) The tandem-L mission proposal: Monitoring earth's dynamics with high-resolution SAR interferometry. In 2009 IEEE Radar Conference (pp. 1–6). IEEE. doi: 10.1109/RADAR.2009.4977077

Langley RB, Teunissen PJ, Montenbruck O (2017) Introduction to GNSS. In: Teunissen PJ, Montenbruck O (eds) Springer Handbook of Global Navigation Satellite Systems. Springer Handbooks. Springer, Cham. doi: 10.1007/978-3-319-42928-1_1

Laurent A, Averbuch O, Beccaletto L, Graveleau F, Lacquement F, Capar L, Marc S (2021) 3-D structure of the Variscan thrust front in northern France: New insights from seismic reflection profiles. Tectonics, 40, e2020TC006642. doi: 10.1029/2020TC006642

Leake S A, Galloway DL (2007) MODFLOW Ground-Water Model—User Guide to the Subsidence and Aquifer-System

Compaction Package (SUB-WT) for Water-Table Aquifers. In Techniques and Methods (6-A23). U. S. Geological Survey doi: 10.3133/tm6A23

Leake S, Galloway D (2010) Use of the SUB-WT package for MODFLOW to simulate aquifer-system compaction in Antelope Valley, California, USA. IAHS-AISH Publication. 339:61–67.

Lechner AM, Baumgartl T, Matthew P, Glenn V (2016) The Impact of Underground Longwall Mining on Prime Agricultural Land: A Review and Research Agenda. Land Degradation & Development 27(6):1650–1663. doi: 10.1002/ldr.2303

Lee FT, Abel J (1983) Subsidence from underground mining: Environmental analysis and planning considerations (USGS-CIRC-876). Colorado School of Mines, Golden (USA). https://www.osti.gov/biblio/6149371

Lee S, Hong SM, Jung HS (2018) GIS-based groundwater potential mapping using artificial neural network and support vector machine models: The case of Boryeong city in Korea, Geocarto International J. 33(8):847–861, doi: 10.1080/10106049.2017.1303091

Lewis RW, Schrefler BA (1987) The finite element method in the deformation and consolidation of porous media

Li F, Liu G, Gong H, Chen B, Zhou C (2022) Assessing land subsidence-inducing factors in the Shandong province, China, by using PS-InSAR measurements, Remote Sensing J. 14(12): 2875–2896, doi: 10.3390/rs14122875

Li J, Zhu L, Gong H, Zhou J, Dai Z, Li X, Teatini P (2022) Unraveling elastic and inelastic storage of aquifer systems by integrating fast independent component analysis and a variable pre-consolidation head decomposition method. Hydrology J. 606:127420, doi: 10.1016/j.jhydrol.2021.127420

Liu D (2013). Synthetic Aperture Radar for Process-Related Monitoring in Urban and Mining Areas (Doctoral dissertation, Dissertation, Braunschweig, Technische Universität Braunschweig).

Liu J, Liu W, Allechy FB, Zheng Z, Liu R, Kouadio KL (2024) Machine learning-based techniques for land subsidence simulation in an urban area. Journal of Environmental Management. 352:120078, doi: 10.1016/j.jenvman.2024.120078

Liu X (2008) Airborne LiDAR for DEM generation: some critical issues. Progress in physical geography J. 32(1):31–49, doi: 10.1177/0309133308089496

Maaß AL, Schüttrumpf H (2018) Long-term effects of mining-induced subsidence on the trapping efficiency of floodplains. Anthropocene, 24:1–13. doi: 10.1016/j.ancene.2018.10.001

Mahapatra, P., der Marel, H. V., van Leijen, F., Samiei-Esfahany, S., Klees, R., & Hanssen, R. (2018). InSAR datum connection using GNSS-augmented radar transponders. Journal of Geodesy, 92, 21-32. doi: 10.1007/s00190-017-1041-y

Mahmoudpour M, Khamehchiyan M, Nikudel MR, Ghassemi MR (2016) Numerical simulation and prediction of regional land subsidence caused by groundwater exploitation in the southwest plain of Tehran, Iran. Engineering Geology J. 201:6–28, doi: 10.1016/j.enggeo.2015.12.004

Mancini F, Grassi F, Cenni N (2021) A workflow based on SNAP–StaMPS open-source tools and GNSS data for PSI-Based ground deformation using dual-orbit sentinel-1 data: Accuracy assessment with error propagation analysis. Remote Sensing, 13(4):753. doi: 10.3390/rs13040753

Marschalko M, Bednárik M, Yilmaz I, Bouchal T, Kubečka K (2012) Evaluation of subsidence due to underground coal mining: An example from the Czech Republic. Bulletin of Engineering Geology and the Environment 71(1):105–111. doi: 10.1007/s10064-011-0401-8

Massonnet D, Feigl KL (1998) Radar interferometry and its application to changes in the Earth's surface, Reviews of Geophysics J. 36(4): 441–500, doi: 10.1029/97RG03139

Mastro P, Serio C, Masiello G, Pepe A (2020) The multiple aperture SAR interferometry (MAI) technique for the detection of large ground displacement dynamics: An overview. Remote Sensing, 12(7):1189. doi: 10.3390/rs12071189

McDonald MG, Harbaugh AW (1988) A modular three-dimensional finite-difference ground-water flow model. US Geological Survey.

Mehrnoor S, Robati M, Kheirkhah Zarkesh MM, Farsad F, Baikpour S (2023) Land subsidence hazard assessment based on novel hybrid approach: BWM, weighted overlay index (WOI), and support vector machine (SVM), Natural Hazards J. 115(3):1997–2030, doi: 10.1007/s11069-022-05624-0

Meng FF, Piao CD, Shi B, Sasaoka T, Shimada H (2021) Calculation model of overburden subsidence in mined-out area based on Brillouin optical time-domain reflectometer technology. International Journal of Rock Mechanics and Mining Sciences 138:104620. doi: 10.1016/j.ijrmms.2021.104620

Métois M, Benjelloun M, Lasserre C, Grandin R, Barrier L, Dushi E, Koçi R (2020) Subsidence associated with oil extraction, measured from time series analysis of Sentinel-1 data: Case study of the Patos-Marinza oil field, Albania. Solid Earth 11(2):363–378. doi: 10.5194/se-11-363-2020

Meyer RF, Powley DE (1988) Subsidence and the petroleum industry: An overview. AAPG (Am. Assoc. Pet. Geol.) Bull.; (United States) 72:2 Article CONF-880301. https://www.osti.gov/biblio/6123088

Meylemans E (2017) It’s all in the Pixels: High-resolution remote-sensing data and the mapping and analysis of the archaeological and historical landscape, Internet Archaeology. 43, doi: 10.11141/ia.43.2

Mhlongo SE (2023) Physical hazards of abandoned mines: A review of cases from South Africa. The Extractive Industries and Society 15:101285. doi: 10.1016/j.exis.2023.101285

Miller M, Shirzaei M (2015) Spatiotemporal characterization of land subsidence and uplift in Phoenix using InSAR time series and wavelet transforms, Geophysical Research: Solid Earth J. 120(8): 5822–5842, doi: 10.1002/2015JB012017

Miller M, Shirzaei M, Argus D (2017) Aquifer mechanical properties and decelerated compaction in Tucson, Arizona, Geophysical Research: Solid Earth J. 122(10): 8402–8416, doi: 10.1002/2017JB014531

Ministerie Vlaamse Gemeenschap, Departement Leefmilieu en Infrastructuur, Administratie Milieu-, Natuur-, Land- en Waterbeheer, Afdeling Water (2004b) Ontwikkelen van regionale modellen ten behoeve van het Vlaams Grondwater Model (VGM) in GMS/MODFLOW. Perceel nr. 3: Brulandkrijtmodel.

Mirsalari SE, Fatehi Marji M, Gholamnejad J, Najafi M (2017) A boundary element/finite difference analysis of subsidence phenomenon due to underground structures. Mining and Environment J. 8(2): 237–253, doi: 10.22044/jme.2016.759

Mitchell JK, Soga K (2005) Fundamentals of soil behavior (Vol. 3). John Wiley & Sons, New York

Moreira A, Prats-Iraola P, Younis M, Krieger G, Hajnsek I, Papathanassiou KP (2013) A tutorial on synthetic aperture radar. IEEE Geoscience and Remote Sensing Magazine, 1(1):6–43. doi: 10.1109/MGRS.2013.2248301

Motagh M, Djamour Y, Walter TR, Wetzel HU, Zschau J, Arabi S (2007). Land subsidence in Mashhad Valley, northeast Iran: Results from InSAR, leveling and GPS. Geophysical Journal J. 168(2): 518–526, doi: 10.1111/j.1365-246X.2006.03246.x

Motagh M, Shamshiri R, Haghshenas Haghighi M, Wetzel HU, Akbari B, Nahavandchi H, Roessner S, Arabi S (2017) Quantifying groundwater exploitation induced subsidence in the Rafsanjan Plain, southeastern Iran, using InSAR time-series and in situ measurements, Engineering Geology J. 218: 134–151, doi: 10.1016/j.enggeo.2017.01.011

Nguyen XP, Cui YJ, Tang AM, Li XL, Wouters L (2014) Physical and microstructural impacts on the hydro-mechanical behavior of Ypresian clays, Applied Clay Science J. 102:172–185, doi: 10.1016/j.clay.2014.09.038

Nicau. (n.d.). La Louvière: Galerie. Retrieved July 19, 2024, from http://www.nicau.be/galeries/lalouviere/1.html

Orhan O (2021) Monitoring of land subsidence due to excessive groundwater extraction using small baseline subset technique in Konya, Turkey. Environmental Monitoring and Assessment 193(4):174. doi: 10.1007/s10661-021-08962-x

Osmanoglu B (2011) Applications and development of new algorithms for displacement analysis using InSAR time series. ProQuest. University of Miami.

Osmanoğlu B, Sunar F, Wdowinski S, Cabral-Cano E (2016) Time series analysis of InSAR data: Methods and trends. ISPRS Journal of Photogrammetry and Remote

Sensing 115:90–102. doi: 10.1016/j.isprsjprs.2015.10.003

Palmer MA, Bernhardt ES, Schlesinger WH, Eshleman KN, Foufoula-Georgiou E, Hendryx M S, Lemly AD, Likens GE, Loucks OL, Power ME, White PS, Wilcock PR (2010) Mountaintop Mining Consequences. Science 327(5962):148–149. doi: 10.1126/science.1180543

Palmqvist CW, Ochsner M, Jamali S, Hashemi H, Amerbilly K, Nilfouroushan F, Bagherbandi M, Karim R, Kour R, Åldstedt R, Norrbin P (2021) Satellite Monitoring of Railways using Interferometric Synthetic Aperture Radar (InSAR)

Park I, Choi J, Jin Lee M, Lee S (2012) Application of an adaptive neuro-fuzzy inference system to ground subsidence hazard mapping, Computers & Geosciences J. 48:228–238, doi: 10.1016/j.cageo.2012.01.005

Peng M, Lu Z, Zhao C, Motagh M, Bai L, Conway BD, Chen H (2022) Mapping land subsidence and aquifer system properties of the Willcox Basin, Arizona, from InSAR observations and independent component analysis, Remote Sensing of Environment J. 271: 112894–112909, doi: 10.1016/j.rse.2022.112894

Perissin D, Wang T (2010) Time-series InSAR applications over urban areas in China. IEEE Journal of Selected Topics in Applied Earth Observations and Remote Sensing, 4(1):92–100. doi: 10.1109/JSTARS.2010.2046883

Perissin D, Wang Z, Wang T (2011) The SARPROZ InSAR tool for urban subsidence/manmade structure stability monitoring in China, proceedings of the ISRSE, Sidney, Australia, 1015.

Pham HT, Rühaak W, Ngo DH, Nguyen OC, Sass I (2020) Fully coupled analysis of consolidation by prefabricated vertical drains with applications of constant strain rate tests: Case studies and an open-source program. Geotextiles and Geomembranes J. 48(3):380–391, doi: 10.1016/j.geotexmem.2019.12.009

Pham HT, Rühaak W, Schuster V, Sass I (2019) Fully hydro-mechanical coupled Plug-in (SUB+) in FEFLOW for analysis of land subsidence due to groundwater extraction. Software Manual. 9:15–19, doi: 10.1016/j.softx.2018.11.004

Phien-wej N, Giao PH, Nutalaya P (2006) Land subsidence in Bangkok, Thailand, Engineering Geology J, 82(4): 187–201, doi: 10.1016/j.enggeo.2005.10.004

Phoon KK, Tang C (2019) Characterisation of geotechnical model uncertainty. Georisk: Assessment and Management of Risk for Engineered Systems and Geohazards. 13(2):101–130, doi: 10.1080/17499518.2019.1585545

Pissart A, Lambot P (1989) Les mouvements actuels du sol en Belgique; comparaison de deux nivellements IGN (1946-1948 et 1976-1980). Annales de la Société géologique de Belgique J, 112(2):495-504

Poland JF, Davis GH (1969) Land subsidence due to the withdrawal of fluids, Reviews in engineering geology J. 2(1969):187–270, doi: 10.1130/REG2–p187

Poulos H G, Carter JP, Small JC (2002) Foundations and retaining structures-research and practice. In Proceedings of the International Conference on Soil Mechanics and Geotechnical Engineering. 4: 2527–2606), AA Balkema Publishers.

Prudic DE (1989) Documentation of a computer program to simulate stream-aquifer relations using a modular, finite-difference, ground-water flow model (Vol. 88). Department of the Interior, US Geological Survey

Public Service of Wallonia (SPW) (2023) The Walloon geographical information website [dataset]. https://geoportail.wallonie.be/catalogue-donnees-et-services

Qin S, Wang W, Song S (2018) Comparative study on vertical deformation based on GPS and leveling data, Geodesy and Geodynamics J. 9(2):115–120, doi: 10.1016/j.geog.2017.07.005

Qu F, Lu Z, Zhang Q, Bawden GW, Kim JW, Zhao C, Qu W (2015) Mapping ground deformation over Houston–Galveston, Texas using multi-temporal InSAR. Remote Sensing of Environment, 16: 290–306. doi: 10.1016/j.rse.2015.08.027

Radhika BP, Krishnamoorthy A, Rao AU (2020) A review on consolidation theories and its application. Geotechnical Engineering J. 14(1):9–15, doi: 10.1080/19386362.2017.1390899

Rafiee M, Ajalloeian R, Dehghani M, Mahmoudpour M (2022) Artificial neural network modeling of the subsidence induced by overexploitation of groundwater in Isfahan-Borkhar Plain, Iran. Bulletin of Engineering Geology and the Environment J. 81(5):170, doi: 10.1007/s10064-022-02646-7

Rajabi A M, Abolghasemi Y, Edalat A (2023) Application of support vector machine in modeling land subsidence in parts of Aliabad plain of Qom. Iranian Journal of Engineering Geology J, 16(1).

Ray S (2019) a quick review of machine learning algorithms, 2019 International Conference on Machine Learning, Big Data, Cloud and Parallel Computing (COMITCon), 35–39, doi: 10.1109/COMITCon.2019.8862451

Reddish DJ, Whittaker BN (2012) Subsidence: occurrence, prediction and control. Elsevier.

Reddish DJ, Whittaker BN (2012) Subsidence: Occurrence, Prediction, and Control. Elsevier.

Ren H, Feng X (2020) Calculating vertical deformation using a single InSAR pair based on singular value decomposition in mining areas. International Journal of Applied Earth Observation and Geoinformation, 92, 102115. doi: 10.1016/j.jag.2020.102115

Rezun B, Janez J, Dizdarevic T (2001) Hydrogeological aspects of the shutdown of the Idrija Mercury Mine.

Roscoe KH, Burland J (1968) On the generalized stress-strain behavior of wet clays. Road Research Laboratory, UK

Rosen PA, Gurrola E, Sacco GF, Zebker H (2012) The InSAR scientific computing environment. EUSAR 2012; 9th European Conference on Synthetic Aperture Radar 730–733.

Rosen PA, Hensley S, Joughin IR, Li FK, Madsen SN, Rodriguez E, Goldstein RM (2000) Synthetic aperture radar interferometry. Proceedings of the IEEE, 88(3):333–382. doi: 10.1109/5.838084

Sadeghi Z, Valadan Zoej MJ, Dehghani M (2013) An Improved Persistent Scatterer Interferometry for Subsidence Monitoring in the Tehran Basin. IEEE Journal of Selected Topics in Applied Earth Observations and Remote Sensing 6(3):1571–1577 doi: 10.1109/JSTARS.2013.2259221

Saelens W (2022) Industrial energy consumption in the urban Low Countries: Ghent and Leiden compared (c. 1650–1850). Urban History, 1–21. doi: 10.1017/S0963926822000645

Salom AT, Kivinen S (2020) Full article: Closed and abandoned mines in Namibia: A critical review of environmental impacts and constraints to rehabilitation. South African Geographical Journal 102(3):389–405. doi: 10.1080/03736245.2019.1698450

Sato C, Haga M, Nishino J (2006) Land Subsidence and Groundwater Management in Tokyo, International Review for Environmental Strategies J. 6(2): 403–424, Corpus ID: 130088967

Schanz T (1998) Zur Modellierung des mechanischen Verhaltens von Reibungsmaterialien.

Schanz T, Vermeer PA, Bonnier PG (1999) The hardening soil model: formulation and verification, Beyond 2000 in computational geotechnics J, 1: 281–296.

Schiffman RL, Stein JR (1970) One-dimensional consolidation of layered systems, Soil Mechanics and Foundations Division J. 96(4): 1499–1504, doi: 10.1061/JSFEAQ.0001453

Schofield A, Wroth P (1968) The critical state soil mechanics. McGraw Hill, London.

Schroeder C, Flamion B, Berger JL, Brixko J, Silva MRD, Charlier R (2008) Evaluation of instability hazards in rock masses influenced by mining works in the coal basin of Liege. Proceedings Post Mining 8:11.

Seed HB (1965) Settlement analysis, a review of theory and testing procedures, Soil Mechanics, and Foundations Division J. 91(2): 39–48, doi: 10.1061/JSFEAQ.0000721

Shamshiri R, Nahavandchi H, Motagh M (2018) Persistent scatterer analysis using dual-polarization sentinel-1 data: Contribution from VH channel. IEEE Journal of Selected Topics in Applied Earth Observations and Remote Sensing 11(9):3105-3112. doi: 10.1109/JSTARS.2018.2848111

Shen SL, Xu YS (2011) Numerical evaluation of land subsidence induced by groundwater pumping in Shanghai. Canadian Geotechnical J. 48(9):1378–1392 doi: org/10.1139/t11-049

Shepley MG, Pearson AD, Smith GD, Banton CJ (2008) The impacts of coal mining subsidence on groundwater resources management of the East Midlands Permo-Triassic Sandstone aquifer, England. Quarterly Journal of Engineering Geology and Hydrogeology 41(3):425–438. doi: 10.1144/1470-9236/07-210

Siriwardane HJ, Kannan RSS, Ziemkiewicz PF (2003) Use of Waste Materials for Control of Acid Mine Drainage and Subsidence. Journal of Environmental Engineering 129(10):910–915. doi: 10.1061/(ASCE)0733-9372(2003)129:10(910)

Siriwardane-de Zoysa R, Schöne T, Herbeck J, Illigner J, Haghighi M, Simarmata H, ... & Hornidge AK (2021) The ‘wickedness’ of governing land subsidence: Policy perspectives from urban Southeast Asia. PLoS One, 16(6):e0250208. doi: 10.1371/journal.pone.0250208

Small D, Holzner J, Raggam H, Kosmann D, Schubert A (2003) Geometric performance of ENVISAT ASAR products. IGARSS 2003. 2003 IEEE International Geoscience and Remote Sensing Symposium. Proceedings (IEEE Cat. No.03CH37477). 2(2):1121–1123. doi: 10.1109/IGARSS.2003.1294031

Songbo W, Yongyao L, Lei Z, Xiaoli D (2020) Multi-temporal InSAR for Urban Deformation Monitoring: Progress and Challenges. 雷达学报, 9(2):277–294. doi: 10.12000/JR20037

Sousa JJ, Hooper AJ, Hanssen RF, Bastos LC, Ruiz AM (2011) Persistent Scatterer InSAR: A comparison of methodologies based on a model of temporal deformation vs. spatial correlation selection criteria. Remote Sensing of Environment, 115(10):2652–2663. doi: 10.1016/j.rse.2011.05.021

Sousa JJ, Ruiz AM, Hanssen RF, Bastos L, Gil AJ, Galindo-Zaldívar J, de Galdeano CS (2010) PS-InSAR processing methodologies in the detection of field surface deformation—Study of the Granada basin (Central Betic Cordilleras, southern Spain), Journal of Geodynamics, 49:181. doi: 10.1016/j.jog.2009.12.002

Streutker DR, Glenn NF (2006) LiDAR measurement of sagebrush steppe vegetation heights. *Remote sensing of environment*, *102*(1-2):135–145.doi: 10.1016/j.rse.2006.02.011

Strozzi T, Wegmuller U (1999) Land subsidence in Mexico City mapped by ERS differential SAR interferometry, IEEE 1999 International Geoscience and Remote Sensing Symposium. IGARSS’99 (Cat. No.99CH36293), 4(4): 1940–1942, doi: 10.1109/IGARSS.1999.774993

Sukirman YB, Lewis RW (1994) Three-dimensional fully coupled flow: consolidation modeling using finite element method. SPE Asia Pacific Oil and Gas Conference, doi: 10.2118/28755-MS

Suresh KP, Kim DJ, Jung J, Cho YK (2019, March) Application of PS-InSAR Technique for Measuring the Coastal Subsidence in the East Coast of South Korea. In 2019 URSI Asia-Pacific Radio Science Conference (AP-RASC) (pp. 1-3). IEEE. doi: 10.23919/URSIAP-RASC.2019.8738313

Syahrir R, Wall F, Diallo P (2021) Coping with sudden mine closure: The importance of resilient communities and good governance. The Extractive Industries and Society 8(4):101009. doi: 10.1016/j.exis.2021.101009

Tavakkoli Estahbanati A, Dehghani M (2018) A Phase Unwrapping Approach Based on Extended Kalman Filter for Subsidence Monitoring Using Persistent Scatterer Time Series Interferometry. IEEE Journal of Selected Topics in Applied Earth Observations and Remote Sensing J. 11(8): 2814–2820, doi: 10.1109/JSTARS.2018.2837020

Tavakkoliestahbanati A, Milillo P, Kuai H, Giardina G (2024) Pre-collapse spaceborne deformation monitoring of the Kakhovka dam, Ukraine, from 2017 to 2023. Communications Earth & Environment, 5(1):145. doi: 10.1038/s43247-024-01284-z

Terzaghi K (1925) Principles of Soil Mechanics, Engineering News-Record J. 95(19): 742–746

Terzaghi K (1943) Theoretical Soil Mechanics. John Wiley & Sons, Inc. doi: 10.1002/9780470172766

Tian Z, Zhao L, Fan H, Lin T, Li T (2024) Mining subsidence monitoring using distributed scatterers InSAR based on Goldstein filter and Fisher information matrix-weighted optimization. Natural Hazards 120:4205–4231. doi: 10.1007/s11069-023-06359-2

Tien Bui D, Shahabi H, Shirzadi A, Chapi K, Pradhan B, Chen W, Khosravi K, Panahi M, Bin Ahmad B, Saro L (2018) Land subsidence susceptibility mapping in South Korea using machine learning algorithms. Sensors J. 18(8):2464, doi:10.3390/s18082464

Tomás R, Romero R, Mulas J, Marturià JJ, Mallorquí JJ, Lopez-Sanchez JM, Herrera G, Gutiérrez F, González PJ, Fernández J, Duque S, Concha-Dimas A, Cocksley G, Castañeda C, Carrasco D, Blanco P (2014) Radar interferometry techniques for the study of ground subsidence phenomena: A review of practical issues through cases in Spain. Environmental Earth Sciences, 71(1):163–181. doi: 10.1007/s12665-013-2422-z

Tomiyasu K (1978) Tutorial review of synthetic-aperture radar (SAR) with applications to imaging of the ocean surface. Proceedings of the IEEE, 66(5):563–583 doi: 10.1109/PROC.1978.10961

Tosi L, Teatini P, Carbognin L, Brancolini G (2009) Using high-resolution data to reveal depth-dependent mechanisms that drive land subsidence: The Venice coast, Italy, Tectonophysics J. 474(1): 271–284, doi: 10.1016/j.tecto.2009.02.026

Tóth J (1970) A conceptual model of the groundwater regime and the hydrogeologic environment. Journal of Hydrology, 10(2):164–176. doi: 10.1016/0022-1694(70)90186-1

Van Leijen FJ (2014). Persistent scatterer interferometry based on geodetic estimation theory.

van Thienen-Visser K, Pruiksma JP, Breunese JN (2015) Compaction and subsidence of the Groningen gas field in the Netherlands. Proceedings of the International Association of Hydrological Sciences. 372(372):367–373, doi: 10.5194/piahs-372-367-2015, 2015.

Vandersteen K, Gedeon M, Leterme B (2012) Hydrogeology of North-East Belgium. External Report. SCK• CEN-ER-236.

Verbeiren B, Batelaan O, De Smedt F (2006) Ontwikkeling van Regionale Modellen ten behoeve van het Vlaams Grondwater Model (VGM) in GMS/MODFLOW. Perceel 1: Centraal Kempisch Systeem. Deelrapport 2: Opbouw van het grondwatermodel, gevoeligheidsanalyse en kalibratie. Vakgroep Hydrologie en Waterbouwkunde (HYDR) - Vrije Universiteit Brussel.

Vlaamse Milieumaatschappij (2016) Stroomgebiedbeheerplan voor de Schelde 2016-2021: Grondwatersysteemspecifiek deel Centraal Vlaams Systeem, depotnummer, Aalst D/2016/6871/019

Voyiadjis GZ, Zhou Y, Abdalla A (2024) Creep-induced subsidence along coastal Louisiana with GPS measurements and finite element modeling. Geoenergy Science and Engineering, 238:212840. doi: 10.1016/j.geoen.2024.212840

Wang H, Gong H, Chen B, Zhou C, Yang Y, Sun X (2024) Research on land subsidence-rebound affected by dualistic water cycle driven by climate change and human activities in Dezhou City, China. Journal of Hydrology. 636:131327, doi: 10.1016/j.jhydrol.2024.131327

Wang S, Liu K, Wang S, Liang Y, Tian F (2022) Three-dimensional stochastic distribution characteristics of void fraction in longwall mining-disturbed overburden. Bulletin of Engineering Geology and the Environment 81(10):414. doi: 10.1007/s10064-022-02929-z

Wang Y, Hong W, Zhang Y, Lin Y, Li Y, Bai Z, Zhang Q, Lv S, Liu H, Song Y (2020) Ground-Based Differential Interferometry SAR: A Review. IEEE Geoscience and Remote Sensing Magazine 8(1):43–70. doi: 10.1109/MGRS.2019.2963169

Wang YQ, Wang ZF, Cheng WC (2019). A review on land subsidence caused by groundwater withdrawal in Xi'an, China. Bulletin of Engineering Geology and the Environment J. 78(4):2851–2863, doi: 10.1007/s10064-018-1278-6

Wdowinski S, Bray R, Kirtman BP, Wu Z (2016) Increasing flooding hazard in coastal communities due to rising sea level: Case study of Miami Beach, Florida, Ocean & Coastal Management J. 126:1–8, doi: 10.1016/j.ocecoaman.2016.03.002

Wen T, Tiewang W, Arabameri A, Asadi Nalivan O, Pal SC, Saha A, Costache R (2022) Land-subsidence susceptibility mapping: Assessment of an adaptive neuro-fuzzy inference system–genetic algorithm hybrid model, Geocarto International J. 37(26):12194–12218, doi: 10.1080/10106049.2022.2066198

Werbrouck I, Antrop M, Van Eetvelde V, Stal C, De Maeyer P, Bats M, Bourgeois J, Court-Picon M, Crombé P, De Reu J, De Smedt P, Finke P, Van Meirvenne M, Verniers J, Zwertvaegher A (2011) Digital elevation model generation for historical landscape analysis based on LiDAR data: A case study in Flanders (Belgium). Expert Systems with Applications J. 38(7): 8178–8185, doi: 10.1016/j.eswa.2010.12.162

Werner C, Wegmuller U, Strozzi T, Wiesmann A (2003) Interferometric point target analysis for deformation mapping. IGARSS 2003. 2003 IEEE International Geoscience and Remote Sensing Symposium. Proceedings (IEEE Cat. No.03CH37477), 7(7):4362–4364. doi: 10.1109/IGARSS.2003.1295516

Wood DM (1990) Soil behavior and critical state soil mechanics. Cambridge University Press.

Xu H, Chen F, Zhou W (2021) A comparative case study of MTInSAR approaches for deformation monitoring of the cultural landscape of the Shanhaiguan section of the Great Wall, Heritage Science J. 9(1): 1–15 doi: 10.1186/s40494-021-00543-y

Xu YS, Shen SL, Cai ZY, Zhou GY (2008) The state of land subsidence and prediction approaches due to groundwater withdrawal in China, Natural Hazards J. 45(1): 123–135, doi: 10.1007/s11069-007-9168-4

Xue F, Lv X, Dou F, Yun Y (2020) A review of time-series interferometric SAR techniques: A tutorial for surface deformation analysis. IEEE Geoscience and Remote Sensing Magazine, 8(1):22–42. doi: 10.1109/MGRS.2019.2956165

Yang J (2022) Bistatic Synthetic Aperture Radar. Woodhead Publishing.

Yang W, Xia X (2013) Prediction of mining subsidence under thin bedrocks and thick unconsolidated layers based on field measurement and artificial neural networks. Computers & Geosciences J. 52:199–203, doi: 10.1016/j.cageo.2012.10.017

Yang Y, Yang W, Peng S, Liu J, Zhang T, Shan H (2022) Land deformation monitoring in the Taiyuan area based on PS-InSAR. Environmental Monitoring and Assessment, 194(9):615. doi: 10.1007/s10661-022-10311-5

Yang YJ, Hwang C, Hung WC, Fuhrmann T, Chen YA, Wei SH (2019) Surface deformation from Sentinel-1A InSAR: relation to seasonal groundwater extraction and rainfall in Central Taiwan. Remote Sensing, 11(23):2817. doi: 10.3390/rs11232817

Yans J (2003) Chronologie des sédiments kaoliniques à faciès wealdiens (Barrémien moyen à Albien supérieur; Bassin de Mons) et de la saprolite polyphasée (Crétacé inférieur et Miocène inférieur) de la Haute-Lesse (Belgique). Implications géodynamiques et paléoclimatiques. Thèse de doctorat, Faculté Polytechnique de Mons et Université de Paris-Sud Orsay, 316 p.

Yarmohammad Touski M, Dehghani M, Veiskarami M (2023) Monitoring and modeling of a landslide in Kahroud, Iran, by InSAR measurements and slope stability analysis. Natural Hazards:117(3):2249-2268. doi:10.1007/s11069-023-05941-y

Yasuhara K, Yamanouchi T, Ue S (1986) Secondary compression of clay in consolidation and undrained shear tests. In International Symposium on recent developments in laboratory and field tests and analysis of geotechnical problems, p 361–374

Yong RN, Townsend FC (1986) Consolidation of soils: testing and evaluation: a symposium (No. 892). ASTM International

Yu H, Lan Y, Yuan Z, Xu J, Lee H (2019) Phase unwrapping in InSAR: A review. IEEE Geoscience and Remote Sensing Magazine, 7(1):40–58. doi: 10.1109/MGRS.2018.2873644

Yun Z (2002) One-dimensional model for land subsidence and its solution, Engineering Geology J. 10(4):434–437

Zanchettin D, Bruni S, Raicich F, Lionello P, Adloff F, Androsov A, ...and Zerbini S (2021) Sea-level rise in Venice: historic and future trends. Natural Hazards and Earth System Sciences. 21(8):2643–2678

Zebker HA, Werner CL, Rosen PA, Hensley S (1994) Accuracy of topographic maps derived from ERS-1 interferometric radar. IEEE transactions on Geoscience and Remote Sensing, 32(4):823–836. doi: 10.1109/36.298010

Zhai W, Zhang Y (2007) Apply spatially variant apodization to SAR/INSAR image processing. In 2007 1st Asian and Pacific Conference on Synthetic Aperture Radar 54–57. IEEE. doi: 10.1109/APSAR.2007.4418553

Zhang L, Ding X, Lu Z (2015) Ground deformation mapping by fusion of multi-temporal interferometric synthetic aperture radar images: A review. International journal of image and data fusion, 6(4):289–313. doi: 10.1080/19479832.2015.1068874

Zhang L, Su Y, Li Y, Lin P (2024) Estimating urban land subsidence with satellite data using a spatially multiscale geographically weighted regression approach. Measurement, 228:114387. doi: 10.1016/j.measurement.2024.114387

Zhang W, Gu X, Hong L, Han L, Wang L (2023) Comprehensive review of machine learning in geotechnical reliability analysis: Algorithms, applications, and further challenges. Applied Soft Computing J. 136: 110066, doi: 10.1016/j.asoc.2023.110066

Zhao K, Chen S (2011) Study on artificial neural network method for ground subsidence prediction of metal mine. Procedia Earth and Planetary Science J. 2:177–182, doi: 10.1016/j.proeps.2011.09.029

Zheng C, Wang PP (1999) MT3DMS: a modular three-dimensional multispecies transport model for simulation of advection, dispersion, and chemical reactions of contaminants in groundwater systems; documentation and user’s guide.

Zheng J, Yao W, Lin X, Ma B, Bai L (2022) An Accurate Digital Subsidence Model for Deformation Detection of Coal Mining Areas Using a UAV-Based LiDAR, Remote Sensing J. 14(2):421–440, doi: 10.3390/rs14020421

Zhou C, Gong H, Chen B, Li X, Li J, Wang X, Gao M, Si Y, Guo L, Shi M, Duan G (2019) Quantifying the contribution of multiple factors to land subsidence in the Beijing Plain, China with machine learning technology, Geomorphology J. 335: 48–61, doi: 10.1016/j.geomorph.2019.03.017

Zhuang C, Zhou Z, Illman WA (2017) A Joint analytic method for estimating aquitard hydraulic parameters. Ground WaterJ. 55(4):565–576 doi:10.1111/gwat.12494

Zienkiewicz OC, Taylor RL (1989) The Finite Element Method: Solid mechanics. Butterworth-Heinemann.

Appendix A. Scientific Contribution and Publications

Scientific Articles

A. Choopani, P. Orban, P. Y. Declercq, X. Devleeschouwer, and A. Dassargues, Challenges in comparing land subsidence measurements by PS-InSAR with simulations from coupled hydro-geomechanical modeling: a case study in Antwerp harbour. C*urrently under review* in the Hydrogeology Journal.

A. Choopani, P. Y. Declercq, B. Ronchi, X. Devleeschouwer, Assessing Hydrogeological Hazards in the Post-Mining Region in Saint-Vaast, Belgium: Insights from Three Decades of SAR Data and Piezometric Analysis. *Currently under review* at the Journal of Natural Hazards.

Declercq, P. Y., Dusar, M., Pirard, E., Verbeurgt, J., **Choopani, A.**, & Devleeschouwer, X. (2023). Post-mining ground deformations transition related to coal mines closure in the Campine coal basin, Belgium, evidenced by three decades of MT-InSAR data. Remote Sensing, 15(3), 725. Doi: 10.3390/rs15030725

Congresses and Seminars

Choopani, A., Declercq, P. Y., Orban, P., Devleeschouwer, X., & Dassargues, A. (2021, September). Land subsidence as revealed by PS-InSAR observations in the Antwerp area (Belgium): first steps towards the understanding and modelling. In IAH2021 48th IAH Congress' Inspiring Groundwater'.

Choopani, A., Declercq, P. Y., Verbeurgt, J., De Doncker, F., Orban, P., Devleeschouwer, X., & Dassargues, A. (2023, April). Subsidence Evolution of Antwerp Region, Belgium over 77 Years, Using Historical Levelling and GNSS Data and Recent Persistent Scatterers Interferometry Observations. In *EGU 2023*.

Moreau, A., **Choopani, A.**, Declercq, P. Y., Orban, P., Devleeschouwer, X., & Dassargues, A. (2023, April). Difficulties arising when PS-InSAR displacement measurements are compared to results from geomechanical and groundwater flow computations. In *EGU General Assembly 2023*.

Devleeschouwer, X., **Choopani, A.**, Moreau, A., Walraevens, K., Van Camp, M., Van Camp, M., ... & Declercq, P. Y. (2021, September). The LASUGEO project: monitoring LAnd SUbsidence caused by Groundwater exploitation through gEOdetic measurements. In *7th International Geologica Belgica Meeting*.

Choopani, A., Orban, P., Declercq, P. Y., Devleeschouwer, X., & Dassargues, A. (2023, July). APPLICATION OF A MULTIDISCIPLINARY APPROACH TO ASSESS CONSOLIDATION IN DIFFERENT GEOLOGICAL LAYERS AT A LOCAL SCALE IN ANTWERP. In *International Geoscience and Remote Sensing Symposium 2023*.

Declercq, P. Y., **Choopani, A.**, Verbeurgt, J., Devleeschouwer, X. (2023, July). POST MINING GROUND DEFORMATIONS FROM LAND SUBSIDENCE TO REBOUND: AN OVERVIEW OF THE CAMPINE (LIMBURG, BELGIUM) COAL MINING DISTRICT. In *International Geoscience and Remote Sensing Symposium 2023*.

Choopani, A., Ronchi, B., Declercq, P. Y., & Devleeschouwer, X. (2022, November). Ground Deformations Related to an Old Drainage Adit in The Abandoned Coal Concession Around Saint-Vaast (Wallonia, Belgium) Analyzed Using PS InSAR and Piezometric Wells Time Serie. In *International*

Mine Water Association Conference (IMWA 2022).

Devleeschouwer, X., **Choopani, A.**, & Declercq, P. Y. (2023). Ground Deformations Observed for Three Decades (1992-2022) above Old and Deep Coal Mines Reused for Deep Gas Storage Sites (Wallonia, Belgium) Using PS-InSAR Time-Series. In International Mine Water Association Conference (IMWA 2022). International Mine Water Association, Christchurch, New Zealand.

Choopani, A., Declercq, P. Y., Verbeurgt, J., De Doncker, F., Orban, P., Dassargues, A., & Devleeschouwer, X. (2023, April). A Step Towards Accurate Integrated Monitoring of The Sinking Zones in the Coastal Area of Antwerp Due to Possible Hydrogeological and Geomechanical Processes. In *10th International Symposium on Land Subsidence (TISOLS 2023)*.

Moreau, A., **Choopani, A.**, Declercq, P. Y., Orban, P., Devleeschouwer, X., & Dassargues, A. (2023, April). A Summary Review Based on Case Studies of the Challenges Related to the Comparison of Displacements Measured by PS-InSAR and Simulated by Geomechanical Coupled to Groundwater Models. In *The Tenth International Symposium on Land Subsidence*. Copernicus Publications, Göttingen, Germany.